CURRENT DEBATES in SCIENCE and MATHEMATICS

EDITOR
Assoc. Prof. Aykut DEMİRÇALI



DUVAR

CURRENT DEBATES in SCIENCE and MATHEMATICS

EDITOR
Assoc. Prof. Aykut DEMİRÇALI



Current Debates in Science and Mathematics
Editor: Assoc. Prof. Aykut DEMİRÇALI, Ph.D.

Editor in chief: Berkan Balpetek
Cover and Page Design: Duvar Design
Printing : First Edition-OCTOBER 2022
Publisher Certificate No: 49837
ISBN:978-625-8109-82-5

© **Duvar Publishing**
853 Sokak No:13 P.10 Kemeraltı-Konak/Izmir/ Turkey
Phone: 0 232 484 88 68
www.duvaryayinlari.com
duvarkitabevi@gmail.com

TABLE OF CONTENTS

Chapter 1 **5**
A New Loss Distribution: Some Statistical Properties and
Premiums Based on Risk Measures
Abdullah Yılmaz, Altan Tunçel

Chapter 2 **21**
Some Generalized Algorithm For Using the
Diophantus-Al-Khwarizmi Substitution
A.B. Urdaletova, S.K. Kydyraliev, A.A. Doolotova

Chapter 3 **31**
Pharmaceutical Wastes Removal in Wastewater by Composites
Ayfer YILDIRIM

Chapter 4 **45**
Grand Story of a Tiny Particle:Neutrino
Çağın KAMIŞCIOĞLU

Chapter 5 **61**
Homology Modeling and Importance
Gizem KÖPRÜLÜLÜ KÜÇÜK

Chapter 6 **71**
A Robust Numerical Method For the Singularly Perturbed
Integro-Differential Equations
Derya ARSLAN

Chapter 7 **83**
Pseudo Quadratıc Modules
Elis SOYLU YILMAZ

Chapter 8 **99**
Age and Body Size of the Anatolian Banded Newt
Ommatotriton Nesterovi (Litvinchuk, Zuiderwijk, Borkin & Rosanov, 2005)
Ufuk BÜLBÜL, Hatice ÖZKAN, Engin ZAMAN

Chapter 9 **111**
Leaves of Kermes Oak Induces a Priming Effect on
Soil Organic Carbon Mineralization
Şahin CENKSEVEN, Burak KOÇAK

Chapter 10 **127**
Variational Approach For Optimal Control of
A Nonlocal Elasticity Theory Based-Single Walled Carbon
Nanotube Model
Seda GÖKTEPE KÖRPEOĞLU

Chapter 11 **139**
The Behaviors Of Heavy Ion Therapy In Layer Bio Structures
Fatih EKİNCİ

Chapter 12 **153**
Fruit Micromorphology Of
Some *Myosotis* L. (Boraginaceae) Species From Turkey
Pınar AKDOĞAN ŞİRİN, Öznur ERGEN AKÇİN

Chapter 13 **171**
A Deadly Virus In Computer:
In Silico World Of Sars-Cov-2, Homology Modeling and
Molecular Docking
Nazlı Irmak GİRİTLİOĞLU, Gizem KÖPRÜLÜLÜ KÜÇÜK

Chapter 14 **187**
A Research on the Histo-Anatomical Characteristics of
Some Species of *Anagallis* (Primulacaeae) Distributed in Turkey
Sibel ULCAY

Chapter 1

A New Loss Distribution: Some Statistical Properties and Premiums Based on Risk Measures

Abdullah Yılmaz[1]
Altan Tunçel[2]

1 Asst.Prof.Dr., Kırıkkale University, Department of Actuarial Sciences.
ORCID: 0000-0002-1196-9541, a.yilmaz@kku.edu.tr

2 Assoc.Prof.Dr., Kırıkkale University, Department of Actuarial Sciences.
ORCID: 0000-0002-5339-1071, atuncel@kku.edu.tr

1. INTRODUCTION

The derivation of loss distributions from insurance data is not an easy task. The loss distributions have been and continues to be an important area of actuarial study. Many papers have been presented to this area that discusses various actuarial applications examining loss distributions. Some of these distributions are Weibull, Exponential, Lognormal, Pareto and Gamma. One of the main characteristics of these distributions is being right-skewed. Therefore, estimating the loss severity in the actuarial study due to the fact that all of them have a right skewed feature. It is the purpose of this paper to define some elementary functions which utilize an underlying loss distribution and then use these functions to generalize the derivation of several actuarial rating values.

A new class of uni-bimodal skewed distributions with a more flexible hazard function, the alpha symmetric distribution, was described by [7]. In the past few years, many distributions which belong to the skew-symmetric distributions family of distributions have been investigated such as [1], [2], [11], [3]. The Esscher transform is a measure transform, introduced by Esscher [5] in an actuarial context. Since the studied of Gerber and Shiu [6] The Esscher transform is a very important tool in actuarial science and insurance. Benth and Sgarra [4] have discussed the application of the Esscher transformation to risk premiums. The main goal of this study is to define a more flexible distribution called Esscher transformed Truncated Alpha Skew Laplace distribution (ETASL) for the modeling of insurance data based on Esscher transformation method. For a base probability density function (pdf) $f(x)$ of random variable X, let h be a real number such that

$$M_X(h) = \int_{-\infty}^{\infty} e^{hx}\,\mathrm{f}(x)\mathrm{dx}$$

exist. A new function defined as

$$g(x;h) = \frac{e^{hx} f(x)}{M_X(h)} \tag{1}$$

is a probability density, and it is called the Esscher transform of the original distribution where h is the natural parameter of Esscher transformation.

The rest of this paper is organized as follows: In Section 2, the cdf and pdf of ETASL distribution are obtained. In addition, some important properties of the ETASL distribution such as moments and moment generating function, skewness and kurtosis, modality behavior, order statistics, stress-strength reliability and hazard rate function are studied in that section. Some premium based risk

measures based on ETASL distribution are studied same section. The statistical inference problem for the ETASL distribution according to the maximum likelihood (ML), the least-squares (LS) and the moments-based estimation method are discussed in Section 3. This section also covers a series of simulation experiments for comparing the performance of the obtained estimators are performed. We analyze a real-life dataset from the literature for illustrative purposes in Section 4. Finally, the last section of the paper concludes the study.

2. DEFINITION AND BASIC PROPERTIES

In this section, we introduce the Esscher transformed Truncated Alpha Skew Laplace distribution. The probability density function (pdf) of the Truncated Alpha Skew Laplace distribution (TASL) is

$$f(x;\alpha) = \frac{1+(1-\alpha x)^2}{2(\alpha^2-\alpha+1)} e^{-x}, \quad x > 0, \tag{2}$$

where $\alpha \in \mathbb{R}$ and the moment generating function (mgf) is

$$M(h) = \frac{\alpha^2+\alpha(h-1)+(h-1)^2}{\big((\alpha-1)\alpha+1\big)(1-h)^3}, \qquad h < 1. \tag{3}$$

By using the transformation given by Eq(1) the pdf of the Esscher transformed Truncated Alpha Skew Laplace distribution (ETASL) is obtained as

$$g(x;\alpha,\beta) = \frac{(\alpha^2x^2-2\alpha x+2)\beta^3}{2(\alpha^2+\beta^2-\alpha\beta)} e^{-\beta x}, \quad x \geq 0 \tag{4}$$

Where $\beta = 1 - \mathrm{h} > 0$ and $\alpha \in \mathbb{R}$ are parameters. The corresponding cdf is

$$G(x;\alpha,\beta) = 1 - \frac{2\beta^2+\alpha^2(\beta x(\beta x+2)+2)-2\alpha\beta(\beta x+1)}{2(\alpha^2+\beta^2-\alpha\beta)} e^{-\beta x} \tag{5}$$

where $x \geq 0$. From now on, a random variable *X* distributed the *ETASL* with parameters α and β will be indicated as *X*~*ETASL*(α, β). Figure 1 illustrates the some of the possible shapes of the pdf of *ETASL* distribution for different values of the parameters α and β.

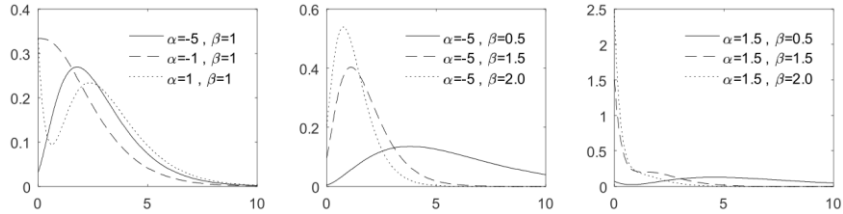

Figure 1. PDF of ETASL distribution for different values of parameters α and β.

2.1. Moments and Moment Generating Function

The moment generating function of *ETASL*(α, β) distribution is

$$M_X(t) = \frac{(\alpha^2 + \alpha(t-\beta) + (t-\beta)^2)\beta^3}{(\alpha^2 - \alpha\beta + \beta^2)(\beta - t)^3}, \quad \beta > t.$$

The kth moment of $X \sim ETASL(\alpha, \beta)$ random variable is

$$\mu_k = E(X^k) = \left(\frac{2\beta^2 + \alpha^2(k+1)(k+2) - 2\alpha\beta(k+1)}{2\beta^k(\alpha^2 - \alpha\beta + \beta^2)}\right)\Gamma(k+1), \qquad (6)$$

where $k=1,2,\ldots$ .Thus, the mean and variance of X can be calculated as

$$\mu = E(X) = \frac{\alpha - 2\beta}{\alpha^2 - \alpha\beta + \beta^2} + \frac{3}{\beta}, \qquad (7)$$
$$Var(X) = \frac{\alpha^2 + 2\alpha\beta - 2\beta^2}{(\alpha^2 - \alpha\beta + \beta^2)^2} + \frac{3}{\beta^2}.$$

2.2. Skewness and Kurtosis

Both the skewness (γ_1) and kurtosis (γ_2) coefficients of the *ETASL*(α, β) distribution can be obtained in short forms. The skewness coefficient is

$$\gamma_1 = \frac{2(3\alpha^6 - 9\alpha^5\beta + 18\alpha^4\beta^2 - 23\alpha^3\beta^3 + 21\alpha^2\beta^4 - 6\alpha\beta^5 + \beta^6)}{\beta^3(\alpha^2 - \alpha\beta + \beta^2)^3\left(\left(\frac{\alpha^2 + 2\alpha\beta - 2\beta^2}{(\alpha^2 - \alpha\beta + \beta^2)^2}\right) + \left(\frac{3}{\beta^2}\right)\right)^{3/2}},$$

and the kurtosis is

$$\gamma_2 = \frac{9(5\alpha^8 - 20\alpha^7\beta + 52\alpha^6\beta^2 - 80\alpha^5\beta^3 + 90\alpha^4\beta^4 - 68\alpha^3\beta^5 + 36\alpha^2\beta^6 - 8\alpha\beta^7 + \beta^8)}{(3\alpha^4 - 6\alpha^3\beta + 10\alpha^2\beta^2 - 4\alpha\beta^3 + \beta^4)^2}$$

The Figure 2 shows the variation of skewness and kurtosis with respect to the β parameter for some selected values of the α parameter.

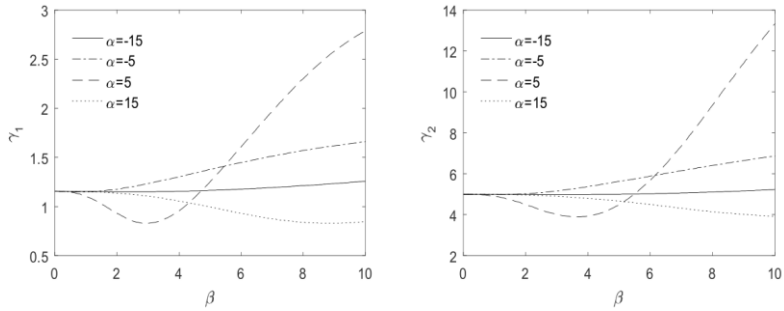

Figure 2. Skewness (γ_1) and kurtosis (γ_2) coefficients of ETASL*(α, β) distribution for different values of parameters α and β.*

2.3. Modality Behavior

The critical values of the pdf of the ETASL distribution are given by

$$x_{1,2} = \frac{\alpha^2 + \alpha\beta \mp \sqrt{\alpha^4 - \alpha^2\beta^2}}{\alpha^2\beta}.$$

Thus, for real-valued critical points to exist, $|\alpha| \geq \beta$ must be present. On the other hand

$$g''(x_{1,2};\alpha,\beta) = \pm\frac{\beta^3\sqrt{\alpha^2(\alpha-\beta)(\alpha+\beta)}}{\alpha^2-\alpha\beta+\beta^2} e^{\left(\frac{\sqrt{\alpha^2(\alpha-\beta)(\alpha+\beta)}-\alpha(\alpha+\beta)}{\alpha^2}\right)}.$$

The mode of the distribution occurs at $x = 0$ and x_1 since $g''(x_1;\alpha,\beta) > 0$ and $g''(x_2;\alpha,\beta) < 0$ for $\alpha > \beta$. In this case, the distribution will be decreasing between $(0, x^2)$, increasing between (x_2, x_1) and continuously decreasing after the mode at x_1. If $\alpha < 0$ and $-\alpha > \beta$ then $g''(x_1;\alpha,\beta) < 0$ and $g''(x_2;\alpha,\beta) > 0$ the only mode of the distribution will be at x_2. So, the distribution will be increase between $(0, x_2)$, and decrease continuously after the mode at x_2. If $\alpha = \beta$, the mode other than zero will be at the $2\beta^{-1}$ point. In summary, if we denote the mode of the *ETASL*(α, β) distribution with x_T,

$$x_T = \begin{cases} \left\{0, \dfrac{\left(\alpha^2 + \alpha\beta - \sqrt{(\alpha^4 - \alpha^2\beta^2)}\right)}{\alpha^2\beta}\right\} & ,\alpha > \beta \\ \dfrac{\left(\alpha^2 + \alpha\beta + \sqrt{(\alpha^4 - \alpha^2\beta^2)}\right)}{\alpha^2\beta} & ,\alpha < 0, -\alpha > \beta \\ \{0, 2\beta^{-1}\} & ,\alpha = \beta \\ 0 & ,otherwise \end{cases}.$$

2.4. Stress-Strength Reliability

Suppose Y represents the `stress' and $X$ represents the `strength' to sustain the stress, then the stress-strength reliability is denoted by $R = P(Y < X)$. Let $X \sim ETASL(\alpha_1, \beta_1)$ and $Y \sim ETASL(\alpha_2, \beta_2)$. If $\alpha_1 = \alpha_2 = \alpha$ stress-strength reliability $P(Y < X)$ is

$$R = \left(\frac{\beta^{23}}{(\beta^1+\beta^2)^5(\alpha^2-\alpha\beta^1+\beta^{12})(\alpha^2-\alpha\beta^2+\beta^{22})}\right)\times$$
$$[\beta^{14}(7\alpha^2-10\alpha\beta^2+6\beta^{22})-2\beta^{13}(\alpha-\beta^2)\left(5\alpha^2+2\beta^2(\beta^2-2\alpha)\right)+$$
$$\beta^{12}(\alpha^2-\alpha\beta^2+\beta^{22})(10\alpha^2-5\alpha\beta^2+\beta^{22})$$
$$+\alpha\beta^2\beta^1(5\alpha-\beta^2)(\alpha^2-\alpha\beta^2+\beta^{22})+$$
$$\alpha^2{\beta_2}^2(\alpha^2-\alpha\beta_2+{\beta_2}^2)+{\beta_1}^5(4\beta_2-3\alpha)+{\beta_1}^6].$$

If $\beta_1 = \beta_2 = \beta$

$$R = \frac{2\alpha^2\beta^2(\alpha^2-2\beta)+\alpha^1\beta(8\alpha^2\beta-5\alpha^{22}-12\beta^2)+\alpha^{12}(-11\alpha^2\beta+8\alpha^{22}+14\beta^2)+8\beta^4}{16(-\alpha^1\beta+\alpha^{12}+\beta^2)(-\alpha^2\beta+\alpha^{22}+\beta^2)}.$$

2.5. Hazard Rate Function

The hazard rate function h_r of $X \sim ETASL(\alpha, \beta)$ random variable is

$$h_r(x) = \frac{g(x;\alpha,\beta)}{1-G(x;\alpha,\beta)}$$
$$= \frac{\beta^3(\alpha x(\alpha x-2)+2)}{2\beta^2+\alpha^2(\beta x(\beta x+2)+2)-2\alpha\beta(\beta x+1)},$$

where $x \geq 0, \alpha > 0, \beta > 0$ and $\alpha \in \mathbb{R}$. Critical point of the $h_r(x)$ is $x_{1,2} = \frac{\beta-\alpha\mp\sqrt{\alpha^2+\beta^2}}{\alpha\beta}$ and

$$h_r''(x_1) < 0 \; and \; h_r''(x_2) > 0, if \; \alpha > 0$$
$$h_r''(x_1) > 0 \; and \; h_r''(x_2) < 0, if \; \alpha < 0.$$

Furthermore $h_r(x)$ is bathtub shape when $\alpha > 0$ and $\alpha - \beta + \sqrt{(\alpha^2+\beta^2)} > 0$. The Figure 3 shows $h_r(x)$ function for different values of parameters.

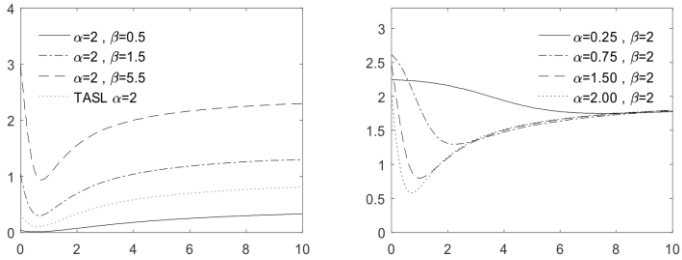

Figure 3. The hazard rate function $h_r(x)$ *of* ETASL*(α, β) distribution for different values of parameters α and β.*

2.6. Order Statistics

Let $X_1, X_2, \dots, X_n$ be a random sample from $ETASL(\alpha,\beta)$ distribution and $X_{(i)}$ denotes the corresponding *i*th order statistics. It is easy to see that the pdf of $X_{(i)}$ is

$$g_{X_{(i)}}(x;\alpha,\beta) = \frac{\left(\beta^3 2^{i-n-1}(\alpha x(\alpha x-2)+2)n!\, e^{-\beta x}\right)}{(\alpha^2-\alpha\beta+\beta^2)\Gamma(i)\Gamma(n-i+1)} \times \left(\frac{e^{-\beta x}\left(-2\beta^2+\alpha^2\left(-(\beta x(\beta x+2)+2)\right)+2\alpha\beta(\beta x+1)\right)}{\left(2(\alpha^2-\alpha\beta+\beta^2)\right)}+1\right)^{i-1} \times \left(\frac{e^{-\beta x}\left(2\beta^2+\alpha^2(\beta x(\beta x+2)+2)-2\alpha\beta(\beta x+1)\right)}{\alpha^2-\alpha\beta+\beta^2}\right)^{n-i}.$$

Hence, pdf of $X_{(1)} = min\{X_1, X_2, \dots, X_n\}$ obtained as

$$g_{X_{(1)}}(x;\alpha,\beta) = \frac{\beta^3 2^{-n} n(\alpha x(\alpha x-2)+2)e^{-\beta x}}{\alpha^2-\alpha\beta+\beta^2} \times \left(\frac{e^{-\beta x}\left(2\beta^2+\alpha^2(\beta x(\beta x+2)+2)-2\alpha\beta(\beta x+1)\right)}{\alpha^2-\alpha\beta+\beta^2}\right)^{n-1},$$

and pdf of $X_{(n)} = max\{X_1, X_2, \dots, X_n\}$ obtained as

$$g_{X_{(n)}}(x;\alpha,\beta) = \frac{\beta^3 n(\alpha x(\alpha x-2)+2)e^{-\beta x}}{2(\alpha^2-\alpha\beta+\beta^2)} \times \left(\frac{e^{-\beta x}\left(-2\beta^2+\alpha^2\left(-(\beta x(\beta x+2)+2)\right)+2\alpha\beta(\beta x+1)\right)}{2(\alpha^2-\alpha\beta+\beta^2)}+1\right)^{n-1}.$$

3. INFERENCE

The methods used to obtain the point estimation of the α and β parameters of the *ETASL*(α,β) distribution will be the subject of this section. Let $X_1, X_2, \dots, X_n$ random variables be a sample from *ETASL*(α,β). Then the maximum likelihood estimation (MLE), least squares estimation (LSE) and moments estimation (ME) of these parameters are examined in the following subsections.

3.1. Maximum Likelihood Estimation

The log-likelihood function of ETASL distribution calculated as

$$\sum_{i=1}^{n} lng(\alpha,\beta;X_i) = nln\left[\frac{\beta^3}{2(\alpha^2+\beta^2-\alpha\beta)}\right] + \sum_{i=1}^{n} n\left[\left(\alpha^2 X_i^2 - 2\alpha X_i + 2\right)\right] - \beta\sum_{i=1}^{n} X_i.$$

Derivation of log-likelihood function with respect to α and β is

$$\frac{\partial}{\partial\alpha}\sum_{i=1}^{n} lng(\alpha,\beta;x_i) = n\left[\frac{\beta-2\alpha}{\alpha^2-\alpha\beta+\beta^2}\right] + \sum_{i=1}^{n}\frac{\alpha x_i^2 + x_i(\alpha x_i - 2)}{\alpha x_i(\alpha x_i - 2)+2} = 0, \tag{8}$$

$$\frac{\partial}{\partial\beta}\sum_{i=1}^{n} lng(\alpha,\beta;x_i) = n\left[\frac{\alpha-2\beta}{\alpha^2-\alpha\beta+\beta^2} + \frac{3}{\beta}\right] + \sum_{i=1}^{n} x_i = 0, \tag{9}$$

Let the maximum likelihood estimates of the α and β parameters be denoted by $\hat{\alpha}_{ML}$ and $\hat{\beta}_{ML}$. $\hat{\alpha}_{ML}$ and $\hat{\beta}_{ML}$ are obtained by simultaneously solving the equations Eq(8) and Eq(9) numerically.

3.2. Method of Moments Estimation

The first moment of the *ETASL*(α,β) distribution were given in Eq(7) and second moment can be obtained by Eq(6). Following equation is obtained by equalizing the first two moments to the sample moments.

$$\frac{\alpha-2\beta}{\alpha^2-\alpha\beta+\beta^2} + \frac{3}{\beta} = \frac{1}{n}\sum_{i=1}^{n} X_i,$$

$$\frac{2(6\alpha^2-3\alpha\beta+\beta^2)}{\beta^2(\alpha^2-\alpha\beta+\beta^2)} = \frac{1}{n}\sum_{i=1}^{n} X_i^2.$$

By solving these two equations with respect to α and β, the moment estimators $\hat{\alpha}_M$ and $\hat{\beta}_M$ can be obtained.

3.3. Least Squares Estimation

To obtain the least squares estimators, first using the index j for shortening the ordered sample values $\left(x_{(1)} \leq \cdots \leq x_{(n)}\right)$, so we can write $x_j \coloneqq x_{(j)} \quad , j = 1,2, \ldots, n$.

The least squares estimators $\hat{\alpha}_{LS}$ and $\hat{\beta}_{LS}$ for the parameters of the *ETASL*(α,β) distribution is obtained by minimizing

$$\sum_{j=1}^{n}\left(1-\frac{e^{-\beta x_j}\left(2\beta^2+\alpha^2\left(\beta x_j\left(\beta x_j+2\right)+2\right)-2\alpha\beta\left(\beta x_j+1\right)\right)}{2(\alpha^2+\beta^2-\alpha\beta)}-\frac{j}{n+1}\right)^2$$

according to the α and β parameters. Thus, the equations

$$\sum_{j=1}^{n}\beta^3 x_j e^{-2\beta x_j}\left(4\alpha-2\beta+\alpha\left(-(\alpha-2\beta)\right)x_j\right)\times \left(\begin{array}{c} 2(\alpha^2-\alpha\beta+\beta^2)\left((j-n-1)e^{\beta x_j}+n+1\right)+ \\ \alpha\beta(n+1)x_j\left(2\alpha-2\beta+\alpha\beta x_j\right) \end{array}\right), \tag{10}$$

$$\sum_{j=1}^{n}\beta^2 x_j e^{-2\beta x_j}\left(6\alpha^2-4\alpha\beta+2\beta^2+\alpha x_j\left(\begin{array}{c} -3\alpha^2+4\alpha\beta \\ -2\beta^2+ \\ \alpha(\alpha^2-\alpha\beta+\beta^2)x_j \end{array}\right)\right)\times \left(\left(\begin{array}{c} 2\alpha^2 \\ -2\alpha\beta \\ +2\beta^2 \end{array}\right)\left((j-n-1)e^{\beta x_j}+n+1\right)+\alpha\beta(n+1)x_j\left(\begin{array}{c} 2\alpha \\ -2\beta \\ +\alpha\beta x_j \end{array}\right)\right) \tag{11}$$

are obtained. The values of the $\hat{\alpha}_{LS}$ and $\hat{\beta}_{LS}$ estimators are obtained by equating the Eq(10) and Eq(11) to zero and solving them simultaneously.

4. SIMULATION

In this section, we did the Monte Carlo simulation studies to show and compare the prediction performances of M, ML, LS and weighted-least squares (WLS) estimators that have been obtained in previous section. In Monte Carlo simulations, the mean square errors (MSE) based on the simulation results, repeated at 100 times for different values of α and β, are given in the Figure 4. As can be seen from the figure, while the sample size increases, the mean error squares approach zero.

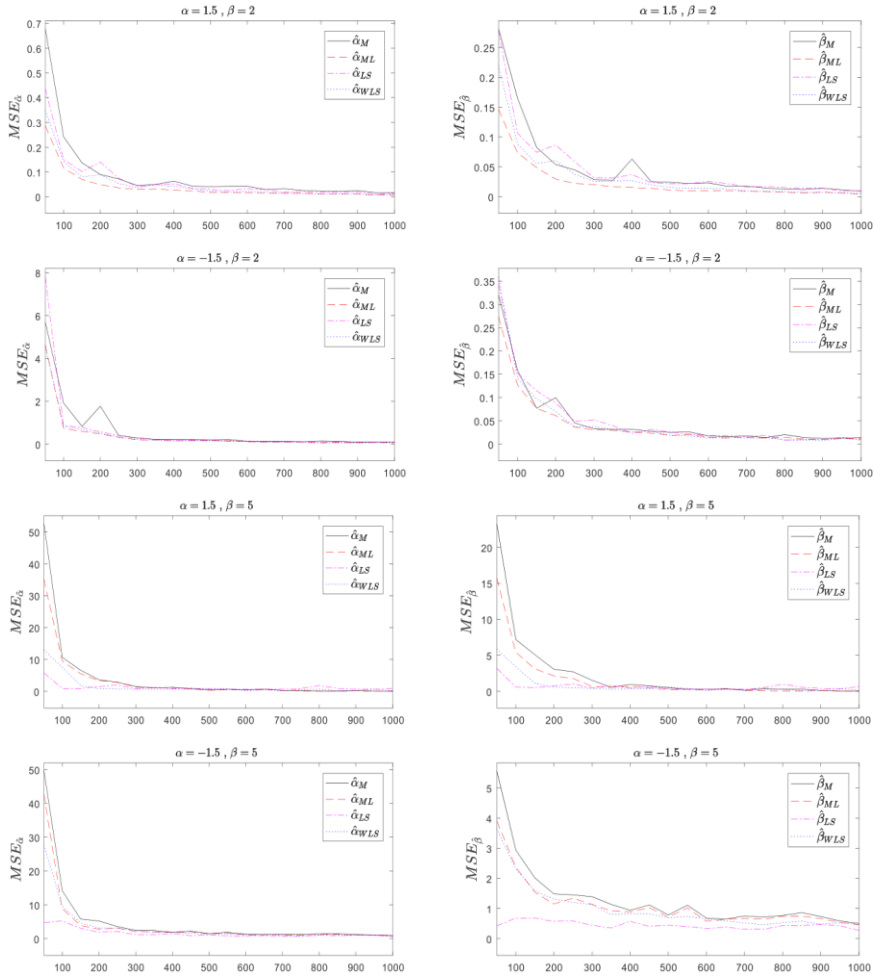

Figure 4. MSE of parameter estimations for different values of sample sizes and parameters.

5. PREMIUM BASED RISK MEASURES

In actuarial science, premium-based risk measures first appeared in the concept of the premium principle, also called the traditional premium principle. It is defined as the function that determines the appropriate insurance premium to be demanded for the risk of loss between the insured and the insurer. In the premium principle, χ is described as risk of loss and $\mathcal{H}$ denotes the premium principle function as a risk measure.

Mathematically, risk measurement is the functional matching of a loss distribution to real numbers. As a loss random variable, X is nonnegative and the risk measurement function by $\mathcal{H}$, the risk measurement can be defined as $\mathcal{H}: \chi \rightarrow$

$\mathbb{R}$. See for more details [13], [9], [10]. The most well-known premium principles are expected value premium principle, standard deviation premium principle, variance premium principle [12]. Risk measurements are used to determine the economic capital, apart from the premium calculation principles. The common feature of these measurements is the premium calculation provides a higher value than the expected value of the loss. Insurance companies use various risk measurement methods for the capital they need to allocate to meet their future liabilities. In this section we examine the five well known premium principles for $X \sim ETASL(\alpha, \beta)$ as a risk of loss.

Expected Value Risk Premium :

Expected Value Premium Principle can be defined as follows [8],

$$\begin{aligned}\mathcal{H}_E(X) &= (1+\theta)E(X)\\ &= (1+\theta)\left(\frac{\alpha-2\beta}{\alpha^2-\alpha\beta+\beta^2}+\frac{3}{\beta}\right),\end{aligned}$$

where θ is a loading factor and $\theta \geq 0$. It is the most widely used premium principle within the insurance business.

Variance Risk Premium :

Variance Premium Principle states that

$$\begin{aligned}\mathcal{H}_V(X) &= E(X)+\theta Var(X)\\ &= \frac{\alpha-2\beta}{\alpha^2-\alpha\beta+\beta^2}+\frac{3}{\beta}+\theta\left(\frac{\alpha^2+2\alpha\beta-2\beta^2}{(\alpha^2-\alpha\beta+\beta^2)^2}+\frac{3}{\beta^2}\right)\end{aligned}$$

where θ is a loading factor and $\theta \geq 0$.

Standard Deviation Risk Premium :

Standard Deviation Premium Principle is described by following equation:

$$\begin{aligned}\mathcal{H}_D(X) &= E(X)+\theta\sqrt{\left(Var(X)\right)}\\ &= \frac{\alpha-2\beta}{\alpha^2-\alpha\beta+\beta^2}+\frac{3}{\beta}+\theta\sqrt{\frac{\alpha^2+2\alpha\beta-2\beta^2}{(\alpha^2-\alpha\beta+\beta^2)^2}+\frac{3}{\beta^2}}.\end{aligned}$$

Exponential Risk Premium :

Exponential Premium Principle is defined as

$$\mathcal{H}_L(X) = \frac{1}{\theta} lnM_X(\theta)$$
$$= \frac{1}{\theta} ln \frac{\beta^3(\alpha^2 + \alpha(\theta - \beta) + (\beta - \theta)^2)}{(\alpha^2 - \alpha\beta + \beta^2)(\beta - \theta)^3},$$

where $\theta \geq 0$ is a loading factor and $\beta > \theta$.

Esscher Risk Premium:

Esscher Premium Principle is expressed as

$$\mathcal{H}_{ESS}(X) = \frac{E\left(Xe^{\theta X}\right)}{E(e^{\theta X})} = \frac{M_X'(t)}{M_X(t)}$$
$$= \frac{\alpha - 2\beta + 2t}{\alpha^2 + \beta^2 + t^2 - \beta(\alpha + 2t) + \alpha t} + \frac{3}{\beta - t},$$

where $\theta \geq 0$ is a loading factor. Moreover, it is sensitive to the change in the extreme claims.

6. APPLICATION TO REAL DATA

In this research, we provide an application of *ETASL*(α, β) distribution to show the performance of the proposed model. We also provide real-life data set and illustrate the flexibility of the proposed model.

Automobile claim amount dataset consisting of 30 samples [8]. The data set are given below:

54	140	230	560	600	1100	1500	1800	1920
2000	2450	2500	2580	2910	3800	3800	3810	3870
4000	4800	7200	7390	11750	12000	15000	25000	30000
32300	35000	55000.						

To compare the goodness of fit of the proposed distribution with exponential distribution (Exp) and Weibull (Wei), we consider the Kolmogorov-Smirnov (KS) value with p-value, the Akaike information criterion (AIC), the Bayesian information criterion (BIC) and the log-likelihood value in Table 1. The smaller value of these criterions indicates the better fit of the distribution.

Table 1. Summary of fits for automobile claim data.

Dist.	Method	$\hat{\alpha}$	$\hat{\beta}$	KS	p	AIC	BIC	$-L$
ETASL	ME	0.0842	0.1284	0.186	0.222	187.781	190.583	-91.89
	ML	0.0936	0.1403	0.164	0.357	187.56	190.368	-91.78
	LS	0.0463	0.1353	0.137	0.582	194.867	197.669	-95.43
	WLS	0.0654	0.1318	0.137	0.582	189.647	192.449	-92.82
Exp.	ML	9.1688	-	0.279	0.014	194.948	196.349	-96.47
Wei.	ML	7.2680	0.7143	0.154	0.432	190.006	192.808	-93.00

Figure 5 shows graphs of the fitted distributions for automobile claim data. The left panel of this figure shows the histogram of data and fitted pdfs. Empirical CDF and fitted CDFs are shown in the right panel.

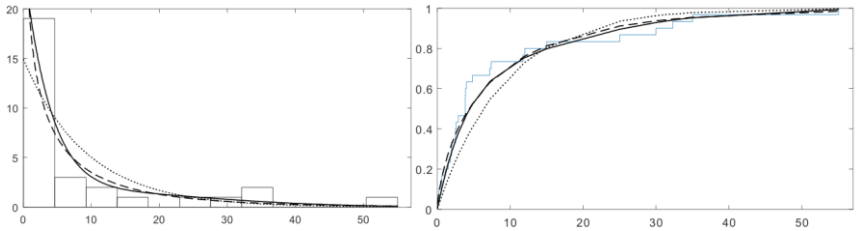

Figure 5. Graphs of fitted distributions for automobile claim data.

The Table 2 shows that the premium based risk measures for automobile claim data values we studied in the previous section.

Table 2. Premium based risk measures for automobile claim data.

θ	Distribution	Method	$\mathcal{H}_E$	$\mathcal{H}_V$	$\mathcal{H}_D$	$\mathcal{H}_L$	$\mathcal{H}_{ESS}$
0.10	Etasl	ME	10.82	25.40	11.08	36.83	110.54
		ML	10.09	22.56	10.33	29.03	76.45
		LS	7.00	11.84	7.10	19.40	71.04
		WLS	8.30	17.01	8.52	28.61	94.81
	Exponential	ML	10.09	17.58	10.09	24.87	110.31
	Weibull	ML	9.93	25.67	10.32	-	-
0.05	Etasl	ME	10.33	17.62	10.46	16.50	27.30
		ML	9.63	15.86	9.75	14.58	22.94
		LS	6.68	9.10	6.73	8.62	12.44
		WLS	7.92	12.28	8.03	11.79	19.18
	Exponential	ML	9.63	13.37	9.63	12.27	16.93
	Weibull	ML	9.48	17.35	9.67	-	-

7. CONCLUSION

The most common statistical distributions used to model risks are not good alternatives for insurance, as in most cases the risk distribution is skewed. In this paper, we proposed a new loss distribution called Esscher transformed truncated alpha-skew-Laplace distribution. Thanks to this distribution, it predicts non-life data well in the actuarial field. It has important statistical representations and is easy to calculate. As a possible future work, different risk measures (VaR, CVaR, EL, etc.) can be calculated using numerical methods.

REFERENCES

[1] Reinaldo B Arellano-Valle, Milton A Cortes, and Hector W Gomez. An extension of the epsilon-skew-normal distribution. Communications in Statistics Theory and Methods, 39(5):912–922, 2010.

[2] Reinaldo B Arellano-Valle, Hector W Gomez, and Fernando A Quintana. Statistical inference for a general class of asymmetric distributions. Journal of Statistical Planning and Inference, 128(2):427–443, 2005.

[3] Gokarna R Aryal and Chris P Tsokos. Application of the truncated skew laplace probability distribution in maintenance system. Journal of Modern Applied Statistical Methods, 8(2):7, 2009.

[4] Fred Espen Benth and Carlo Sgarra. The risk premium and the Esscher transform in power markets. Stochastic Analysis and Applications, 30(1):20–43, 2012.

[5] F Esscher. On the probability function in the collective theory of risk. Skandinavisk aktuarietidskrift, 15, 175-195, 1932.

[6] Gerber Shiu ESW. Option pricing by esscher transforms (with discussion). Trans. Soc. Actuaries, 46:99–191, 1994.

[7] S Shams Harandi and MH Alamatsaz. Alpha–skew–laplace distribution. Statistics-Probability Letters, 83(3):774–782, 2013.

[8] Rob Kaas, Marc Goovaerts, Jan Dhaene, and Michel Denuit. Modern actuarial risk theory: using R, volume 128. Springer Science-Business Media, 2008.

[9] Zinoviy Landsman and Michael Sherris. Risk measures and insurance premium principles. Insurance: Mathematics and Economics, 29(1):103–115, 2001.

[10] Peter Liebwein. Risk models for capital adequacy: Applications in the context of solvency ii and beyond. The Geneva Papers on Risk and Insurance-Issues and Practice, 31(3):528–550, 2006.

[11] V Nekoukhou and MH Alamatsaz. A family of skew-symmetric-laplace distributions. Statistical Papers, 53(3):685–696, 2012.

[12] Tomer Shushi. Skew-elliptical distributions with applications in risk theory. European Actuarial Journal, 7(1):277–296, 2017.

[13] Cansu Telkes. The Comparison of risk measures on claim distributions: Turkish motor insurance case. 2018.

Chapter 2

Some Generalized Algorithm For Using The Diophantus-Al-Khwarizmi Substitution

A.B. Urdaletova[1]
S.K. Kydyraliev[2]
A.A. Doolotova[3]

1 PhD, Kyrgyz-Turkish "Manas" University, anarkul.urdaletova@manas.edu.kg

2 ScD, American University in Central Asia, kydyraliev_s@auca.kg

3 M.A., American University in Central Asia, doolotova_a@auca.kg

1. Introduction

In the course of its development, humanity has achieved impressive successes. Modern vehicles, videophones, ..., often surpass what people only dreamed of in their fairy tales. At the same time, it cannot be considered that the level of intellectual development has changed significantly. Consider a problem that was solved several thousand years ago.

Problem. Find the lengths of the sides a rectangle with a perimeter of 40 cm and an area of 96 cm^2.

Solution. It is easy to understand that in mathematical language, this problem is about solving the system $\begin{cases} ab = 96, \\ a + b = 20, \end{cases}$ where a and b are the lengths of the sides of the rectangle.

Our contemporary is likely to solve this problem roughly as follows: first, express a from the second equation of the system: $a = 20 - b$; then substitute this expression into the first equation, and get a quadratic equation: $ab = 96 \Rightarrow (20 - b)\, b = 96 \Rightarrow 20b - b^2 = 96 \Rightarrow \quad b^2 - 20b + 96 = 0$. The roots of this equation, the numbers 8 and 12, will give the solution to the problem.

But the famous ancient Greek mathematician Diophantus would say: “If the sides were equal to each other, then they would have a length of 10, and their product would be 100. Since $ab = 96$, one of the sides is slightly longer than 10, and the other is as much shorter than 10. So, $a = 10 + z;\ b = 10 - z,$ and $(10 + z)(10 - z) = 96$. Hence, $100 - z^2 = 96 \Rightarrow z^2 = 4 \Rightarrow z = 2$. Thus, $a = 10 + 2 = 12;\ b = 10 - 2 = 8$ ".

It is worth noting that such reasoning was successfully used by many mathematicians of antiquity, such as the Egyptians, Babylonians, Chinese, and Hindus (Katz, 2009; Eves, 1990). Muhammad ben-Musa al-Khwarizmi (783–850), an outstanding mathematician, whose works formed the basis of modern mathematics, occupies a prominent place among them (J. J. O’Connor and E. F. Robertson, 2003). The famous historian of science J. Sarton called him "the greatest mathematician of his time and, all things considered, one of the greatest mathematicians of all time" (Sarton, 1927).

Note that the above mentioned method, let's call it the Diophantus-al Khwarizmi method, can be successfully used to solve various problems. We will show a few such problems in the following part.

2. The Diophantus-al Khwarizmi method: examples

Problem 1. The area of the rectangle is 3120 cm^2, the diagonal is 89 cm. Find the lengths of the sides.

Solution. In mathematical language, this problem is about solving a system $\begin{cases} ab = 3120, \\ a^2 + b^2 = 89^2, \end{cases}$ where a and b are the lengths of the sides of the rectangle. As $(a + b)^2 = a^2 + 2ab + b^2 = 89^2 + 2 \cdot 3120 = 14161 = 119^2$, the original system is equivalent to the system $\begin{cases} ab = 3120, \\ a + b = 119. \end{cases}$ Therefore, it possible take $a = 119/2 + z$; $b = 119/2 - z$.

Then, $(59{,}5 + z)(59{,}5 - z) = 3120$. Hence, $3540{,}25 - z^2 = 3120 \Rightarrow z^2 = 420{,}25 \Rightarrow z = 20{,}5$. In this way, $a = 59{,}5 + 20{,}5 = 80$; $b = 59{,}5 - 20{,}5 = 39$.

Problem 2. The area of the rectangle is 120 mm^2. What is its height if it is equal to three bases plus two millimeters?

Solution. In mathematical language, this problem is about solving a system $\begin{cases} ah = 120, \\ h = 3a + 2, \end{cases} \Leftrightarrow \begin{cases} ah = 120, \\ h - 3a = 2, \end{cases}$ where a and h are the base and height of the rectangle.

Let $h = 1 + z$; $-3a = 1 - z$. Then, $(1 + z)(1 - z) = -3 \cdot ah = -3 \cdot 120$. Hence, $1 - z^2 = -360 \Rightarrow z^2 = 361 \Rightarrow z = 19$. In this way, $h = 1 + z = 20$; $-3a = 1 - z = -18 \Rightarrow a = 6$.

Problem 3. Lena bought carrots for $22. Azamat, discussing the purchase with her, noted that he spent $18 on the purchase of carrots. At the same time, he bought 15 kg less, paying 5 cents more for each kilogram. At what price did Azamat buy carrots?

Solution. As we know, the purchase cost (seller's revenue) is expressed by the formula $R = pq$, where p is the price, q is the purchase volume. According to the conditions of the problem, there is a system of equations $\begin{cases} pq = 22, \\ (p + 0{,}05)(q - 15) = 18. \end{cases}$

The first equation of the system describes Lena's purchase, the second — Azamat's. Expanding the brackets in the second equation: $pq + 0{,}05q - 15p -$

$0,75 = 18$, and replacing pq with its value from the first equation, we get $22 + 0,05q - 15p – 0,75 = 18$.

Then, $0,05q – 15p = -3,25 \Leftrightarrow q – 300p = -65$.

Let $q = -65/2 + z$; $-300p = -65/2 – z$. Hence, $(-32,5 + z)(-32,5 – z) = -300 \cdot 22$.

Consequently, $1056,25 - z^2 = -6600 \Rightarrow z^2 = 7656,25 \Rightarrow z = 87,5$.

In this way, $q = -65/2 + z = -32,5 + 87,5 = 55$; $-300p = -65/2 – z = -32,5 - 87,5 = -120 \Rightarrow p = 0,4$. Thus, Lena bought carrots, a kilogram of which cost 40 cents, and Azamat bought carrots for 45 cents/kg.

3. The Diophantus-al Khwarizmi method: the algorithm

It's time to formalize the algorithm for solving problems using the substitution of Diophantus-Muhammad Al Khwarizmi — the algorithm for solving problems by the method of Diophantus-al Khwarizmi:

To solve the system:

$$\begin{cases} px + qy = r; \\ x \cdot y = s; \end{cases} \qquad (1)$$

with respect to unknown x and y, where p, q, r, s are known numbers, we need to:

- introduce a new unknown variable z according to the formula $px = r / 2 - z$; $qy = r / 2 + z$;
- using the equation xy = s, obtain that $px \cdot qy = (r / 2 - z)(r / 2 + z) = p \cdot q \cdot s$;
- using the formula for the difference of squares, obtain and then solve the equation $(r / 2)^2 - z^2 = p \cdot q \cdot s$ with respect to the unknown z;
- use the found z values to determine the x and y values.

Let us illustrate the method of Diophantus-al Khwarizmi with a couple more examples.

4. The Diophantus-al Khwarizmi method: more examples

Problem. Prove that a square has the largest area among all rectangles of the same perimeter.

Proof. Consider a rectangle with sides a and b and perimeter p. Accordingly, the equality $2(a + b) = p$ takes place. Then, $a + b = p/2$. Following Diophantus, suppose $a = p/4 + z$. Hence, $b = p/4 - z$. Thus, the area of the rectangle is $ab = (p/4 + z)(p/4 - z) = p^2/16 - z^2$. It is clear that the area of a rectangle, which is

written as an expression $S = p^2/16 - z^2$ will have the greatest value at $z = 0$. Then, $a = p/4 + z = p/4$, $b = p/4 - z = p/4$. That is, among all rectangles of the same perimeter, the square has the largest area.

The problem of determining the eigenvalues of a matrix is very important in various fields of mathematics, in particular, when solving systems of linear difference and differential equations. Let us demonstrate how the Diophantus-al Khwarizmi method can be used in this case.

Problem. Determine the eigenvalues of the matrix $\begin{pmatrix} 5\frac{11}{18} & 3\frac{1}{6} \\ 2\frac{7}{19} & 2\frac{1}{9} \end{pmatrix}$.

Solution. Recall that the eigenvalues of the matrix $\begin{pmatrix} a & b \\ c & d \end{pmatrix}$ are the roots of the equation $(a - \lambda)(d - \lambda) - cb = 0$. That is, we need to subtract the unknown λ from the elements of the main diagonal, calculate the determinant of the resulting matrix, equate it to zero and solve the resulting equation.

So, we need to solve the equation $\left(5\frac{11}{18} - \lambda\right)\left(2\frac{1}{9} - \lambda\right) - 2\frac{7}{19} \cdot 3\frac{1}{6} = 0$.

Here we can go the usual way: open the brackets, then solve the resulting quadratic equation. In this case, we will have to deal with not very pleasant calculations. On the other hand, we can use the method of Diophantus-al Khwarizmi.

We denote $x = 5\frac{11}{18} - \lambda;\ y = 2\frac{1}{9} - \lambda$ and note that $2\frac{7}{19} \cdot 3\frac{1}{6} = 7{,}5$. Then, $xy = 7{,}5;\ x - y = (5\frac{11}{18} - \lambda) - (2\frac{1}{9} - \lambda) = 3{,}5$. Therefore, writing x = 3,5/2 - z; -y = 3,5/2 + z, from the equation xy = 7,5, we get that x·(-y) = (1,75 - z)(1,75 + z) = -7,5. That is, 1.752 - z2 = -7.5 => z2 = 10.5625.

Hence, for z = 3,25, we obtain x= 3,5/2 - z = -1,5 and, accordingly, from the equality $x = 5\frac{11}{18} - \lambda$ the first eigenvalue $\lambda = 7\frac{1}{9}$. A negative root value, z = -3.25, will yield the second eigenvalue: x = 3,5 / 2 - z = 5 and, from the equality $x = 5\frac{11}{18} - \lambda$, we get $\lambda = \frac{11}{18}$.

5. The "transfer" method

Next, we're going to get the formula for roots of the quadratic equation. But, before that, let's make a small "lyrical" digression. How do you feel about the statement that the equation $0{,}03x^2 - 8x + 400 = 0$ can be easily solved "in mind"? We think that many will not believe this. But, as it turns out, there is a method that can "make a fairy tale come true". Let's demonstrate it.

Consider the quadratic equation $ax^2 + bx + c = 0$, where $a \neq 0$. By multiplying both sides by a, we get the equation $a^2x^2 + abx + ac = 0$. Now, we introduce the notation $ax = y$, and we arrive at the equation $y^2 + by + ac = 0$. In this method, the coefficient a is multiplied by the free term, as if "transfer" to it. Hence the name of the method is the "transfer" method. So, by "transferring" the coefficient at the square of the equation $0{,}03x^2 - 8x + 400 = 0$ to the free term, we get the equation: $y^2 - 8y + 0.03 \cdot 400 = 0 \Leftrightarrow y^2 - 8y + 12 = 0$. The roots of this very simple quadratic equation are the numbers 2 and 6. Accordingly, the roots of the original equation are the numbers $2/0{,}03$ and $6/0{,}03 = 200$.

Therefore, in order to solve the equation $ax^2 + bx + c = 0$, we will use the "transfer" and get the equation $y^2 + by + ac = 0$. We rewrite it as $y(y + b) = -ac$. Since $y - (y + b) = -b$, we obtain the system $\begin{cases} y(y+b) = -c; \\ y-(y+b) = -b \end{cases}$.

Next, you can use the method of Diophantus-al Khwarizmi:

$y = -b/2 + z$; $-(y + b) = -b/2 - z \Rightarrow$

$ac = y[-(y + b)] = (-b/2 + z)(-b/2 - z) = (-b/2)^2 - z^2$, i.e

$ac = (-b/2)^2 - z^2$. Therefore, $z^2 = (-b/2)^2 - ac$.

Hence, $y = -\frac{b}{2} \pm \sqrt{\left(\frac{b}{2}\right)^2 - ac} = -\frac{b}{2} \pm \sqrt{\frac{b^2 - 4ac}{4}}$.

Remembering that $y = ax$, we return to the original variable and obtain the well-known formula: $x = \frac{-b \pm \sqrt{b^2 - 4ac}}{2a}$

It can be noted that in the process of obtaining a formula for the roots of a quadratic equation given in general form, a formula for the roots of the reduced quadratic equation was obtained. Making the appropriate renaming, we see that the roots of the equation $x^2 + px + q = 0$ can be obtained by the formula

$$x = -\frac{p}{2} \pm \sqrt{\left(\frac{p}{2}\right)^2 - q}\,.$$

6. Conclusion

We think the time has come to talk about the problem outlined in the introduction. In 2003 and 2004, the first and at that time the only regular column appeared in an all-German newspaper. The column "Five Minutes of Mathematics" appeared every Monday in Die Welt, and a few weeks later the column was reprinted in the Berliner Morgenpost. Over the course of two years, one hundred essays have been published on a wide variety of mathematical disciplines. Regular readers of the column got an idea of cryptography and coding theory, got acquainted with the charm of prime numbers and the infinite, learned how mathematics works in CD-players and tomography, figured out the famous Monty Hall problem and other mysteries of probability theory (Behrends, 2008).

Among the topics that aroused the greatest interest was the story about cryptography — about methods of sending secret messages so that they truly remain secret. Cryptography has become a branch of mathematics in which intensive research is conducted today. In recent decades, there has been a sudden surge in commercial interest in prime numbers because the new results have been extremely eloquent and have revealed a lot about the security of encrypted data transmission. It was found that there was no longer any need to store the information used in the encoding and decoding of classified information.

Security now depends on a very specific problem about primes: anyone who can decompose a large number into the product of two primes can read the encrypted message. It is easy to see that, for example, 35 is equal to the product of two prime numbers 7 and 5, but for the number 49 402 601 (it is equal to the product of prime numbers 33 223 and 1487), everything is much more complicated. In serious cryptography, numbers with hundreds of digits are considered. It is generally believed that there is no procedure to set the multipliers of such large numbers so quickly that breaking the cipher is of practical use. This idea has revolutionized cryptography under the name of public key cryptography (Behrends, 2008).

At this point it is time to recall the Diophantus-al-Horezmi method, and to demonstrate how we can solve the problem of multiplication of a number equal to the product of two prime numbers. Let's start with the big number 66446. An uninformed person may get scared, but we know that this is a simple problem and

its solution is: 66446 = 2 · 33223. The fact is that there is only one even prime number - the number 2, and since 66446 is even, one of its factors must be equal to two. Therefore, numbers that are the product of two odd prime numbers are of interest.

So, we have the number n, which is the product of two primes: n = pq. If p is the smaller of them, then q = p + 2k, where k is an integer. Let the number r lie exactly in the middle between the numbers p and q. Then, p = r - k and q = r + k. Therefore, n = (r - k)(r + k) = $r^2 - k^2$, and therefore $n + k^2 = r^2$. So, if you add the exact square of some number to the number n, then you will again get an exact square.

This observation suggests the following algorithm for finding prime multipliers: Let's add to n exact squares $k^2 = 1^2, 2^2, 3^2$, ... and each time check if the number $n + k^2$ is an exact square. The computer will do it quickly. Having received the desired result, we write that $n + k^2$ is equal to r^2. It remains to note that the desired multipliers p and q are given by the formulas p = r - k and q = r + l.

As an example, we will demonstrate the process of decomposition into two prime multipliers of the number 3935167:

$3935167 + 1^2 = 3935168 = (1983{,}7257\ldots)^2$;

$3935167 + 2^2 = 3935171 = (1983{,}72654\ldots)^2$;

$3935167 + 3^2 = 3935176 = (1983{,}7278\ldots)^2$;

…

We will continue this process until the sum becomes an exact square: $3935167 + 33^2 = 3936256 = (1984)^2$. It turned out that the number 3935167 is the product of two primes: 1984 – 33 = 1951 and 1984 + 33 = 2017.

References

1. Behrends, E. (2008). *Five-minute mathematics.* American Mathematical Society.
2. Eves, H. (1990). *An Introduction to the History of Mathematics.* Philadelphia: Saunders College Pub.
3. Katz, V. J. (2009). *A History of Mathematics: An Introduction, 3d edition.* Pearson.
4. O'Connor, J. J. & Robertson, E. F. (1999). "*Abu Ja'far Muhammad ibn Musa Al-Khwarizmi*". Retrieved from: http://www.history.mcs.st-andrews.ac.uk/history/References/ Al- Khwarizmi.html
5. Sarton , G. (1927). Introduction to the History of Science. *Science, 66*(1707), 260-262.

Chapter 3

Pharmaceutical Wastes Removal in Wastewater by Composites

Ayfer YILDIRIM[1]

1 Dr.Öğr.ÜyesiMardin Artuklu University, Vocational School of Health Services, Mardin/Turkey
ayferyildirim@artuklu.edu.tr ORCID ID: https://orcid.org/0000-0002-2079-4587

INTRODUCTION

In recent years, with industrialization, the increase in the search for better efficiency, especially in the chemical, pharmaceutical, textile, and other manufacturing industries, has increased the use of many organic molecules such as pesticides, detergents, drugs, dyes, and other industrial products, and therefore, these compounds formed later on. The toxic properties of many of them pose a danger to human health and ecosystem balance, as they are found in wastewater discharged into rivers [1-3]. Pollution of natural resources such as water continues to be one of the most challenging problems of today's society. Due to the very high consumption brought by globalization, pharmaceutical Wastes (PWs) are considered organic pollutants. One of the classes of emerging contaminants of greatest concern, the pharmaceutical contaminant originates from hospitals, pharmaceutical industries, households, and veterinary and domestic facilities, which are biologically active compounds used to prevent, cure or treat diseases. Pharmaceuticals are chemical compounds designed to improve the quality of life of humans and animals and are the diagnosis, treatment and prevention of diseases. In recent years, with the increase in applications such as self-medication and inappropriate disposal of partially consumed drugs, pharmaceutical wastes have also increased significantly [4,5]. Unfortunately, this situation not only leads to the pollution of ground and surface waters but also poses a high toxicological risk for living things exposed to these compounds. In recent years, as a result of the widespread use of drugs, residues of PWs are frequently found in wastewater and other environmental matrices such as soil and surface waters [6, 7 (**Figure 1)**]. However, it always causes traces of pharmaceuticals to enter the environments and threatens the lives of aquatic and other creatures by allowing wastewater with unrefined/partially processed pharmaceuticals [8]. Moreover, it is known that it carries a potential risk for human health even at very low concentrations. In research, it has been determined that this type of waste is not subject to regulation in many developing countries. Increasing drug consumption and inadequacy of traditional water treatment methods to remove pharmaceutical traces from water have created a global concern. Based on this, both the regulation of such pollutants and the increase of their removal efficiency from wastewater should be sought. This wastewater must be treated before discharge to accomplish environmental regulations.

The adsorption technique, which is among the other traditional treatment techniques (ultrafiltration membrane, biodegradation, electrocoagulation, ozonation), is in demand because of its cheap, efficient and easy application [9,11]. Removal studies of PWs by adsorption have been investigated in recent years. Several materials have been studied as composite adsorbents for the removal of PWs such as zeolite clay-based

[12], metal-organic framework-based [13], chitosan-based [14], cellulose-based [15], metal organic framework-based [16], metals/metal oxides-based [17] etc. Composite is a material prepared by mixing two or more components with different physical and chemical properties. The original components that make up the composite retain their identities and different properties, and the component they form has higher qualities. Composites can be synthesized using natural or polymer synthetic types. The fact that synthetic composites are resistant to ordinary degradation poses a threat to the ecological environment, and therefore it is important to develop alternative composites that are sustainable, biodegradable, cost-effective, economical and environmentally friendly, and non-toxic [18]. For a composite to be called a biocomposite, it must be from a biological source, such as a plant, microbial, or animal, or consist of at least one component that is biodegradable by microorganisms.

In this book chapter, PWs that cause water pollution were examined and their removal via synthetic and biological composites by adsorption technique was investigated.

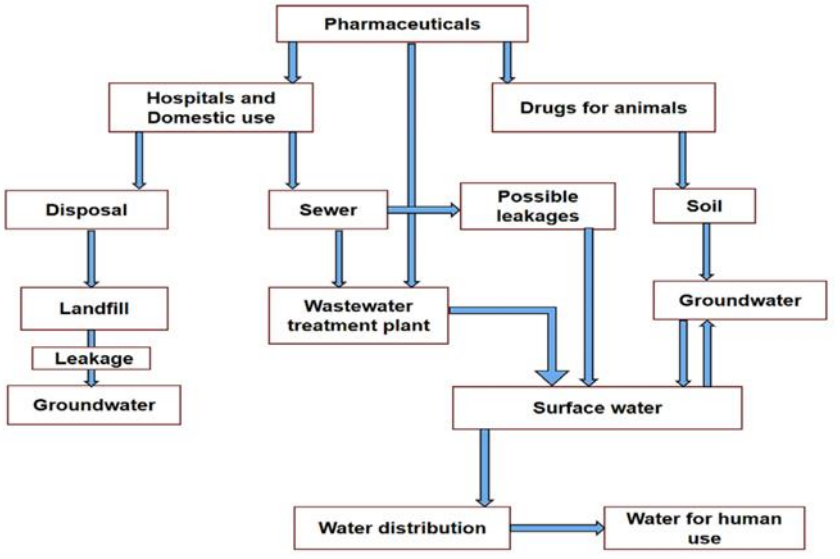

Figure 1. Formation pathways of pharmaceutical wastes [7]

1.MOST COMMON PHARMACEUTICAL WASTES IN WASTEWATER

Some pharmaceutical compounds have a hydrophilic nature, while others have a hydrophobic nature, and even different environmental conditions determine the nature of some drugs. Besides, the nature of a pharmaceutical compound also varies depending on its chemical composition. Many pharmaceuticals can also upset the balance of nature when released into the environment. For example, when

released into water, they cause many negative effects that can cause serious damage to water pollution and thus to aquatic creatures and people. That is why it is of great importance to remove these emerging pharmaceutical pollutants from water. Also, it has become necessary to identify suitable materials for adsorption, which is a suitable treatment method for pharmaceutical removal from wastewater discharges before these wastewaters are reused or released into water bodies. In the literature, various composites have been used as effective adsorbents for the adsorption of pharmaceutical wastes from wastewater.

In this section, the most frequently studied pharmaceutical wastes (β-blockers, Anti-inflammatory Drugs, Antibiotics) in the literature, which pollute the waters due to their wide use, have been mentioned that summarized in **Table 1**.

1.1. β-blockers

Atenolol, (4-[3-(2-hydroxy-3-isopropylamino) propoxy] phenylacetamide), β-blockers, which are frequently used in the treatment of hypertension, angina pectoris, myocardial infarction, are in the drug group. Because this drug is largely unaffected by any chemical structural changes in human excretion, it is widely detected in many environmental matrices such as hospital sewers or wastewater treatment plants [19]. In addition, when Atenolol is used with other drugs, it has been found to have a very harmful effect on the environment and increase the growth of human embryonic stem cells by 30 %.

1.2. Anti-inflammatory Drugs

Inflammatory processes are often associated with infection states. Anti-inflammatory drugs are also drugs used to heal these infections. Ketoprofen, a typical carboxylic anti-inflammatory compound, is a contaminant that can be easily transported from wastewater to other water systems. Hemodynamic changes and thyroid tumors may occur in case of exposure to Diclofenac sodium, an anti-inflammatory drug widely used in the treatment of inflammatory disorders or dysmenorrhea. Also, Ibuprofen causes serious side effects to the human body including vomiting, bleeding, kidney problems, and cardiovascular risk.

1.3. Antibiotics

Antibiotics are the most commonly used type of medicine. Antibiotics, which are partially metabolized after digestion, are excreted from the living body, both metabolized and non-metabolized parts. For this reason, antibiotics that can be released into wastewater by human and animal bodies as a result of insufficient metabolism (30-90%) can also pass into the environment through soils polluted by animal excretion and fertilizer distribution. This antibiotic poses a risk of

inducing bacterial resistance when released into the environment and thus may upset the balance of the flora. For example, Tetracycline, which is frequently used in the treatment of animal diseases, is a medical antibiotic.

2. COMPOSITE ADSORBENTS for PHARMACEUTICAL WASTES

In recent years, the increase in the use of pharmaceuticals, it causes a rapid increase in pharmaceutical wastes and especially their release into water causes water pollution and therefore serious health problems. For this purpose, the search for cheap, easy-to-use, wide-perspective, high adsorption capacity materials for the adsorption technology applied to remove these impurities has also expanded. Therefore, it becomes imperative to purify water effectively by removing these pharmaceutical contaminants. Designer compounds are blended via impregnation with metal oxides, clay minerals, organic compounds, or carbonaceous materials such as graphene oxide, polysaccharides, and carbon nanotubes to synthesize composites and increase the suitability of the composite structure for adsorption.

Due to its excellent gel-forming capacity, hydrophobicity, biodegradability, and low purchasing cost, as well as the chemical structure sensitive to the preparation of composite materials, gelatin is a good alternative with highly superior properties for the production of adsorbent composites. In a study by synthesizing gelatin and carbon nanotubes-based composite, diclofenac sodium adsorption was investigated and its adsorption capacity was determined as 20.57 mg/g [20].

Chitosan macromolecule is frequently preferred in scientific studies because it provides composites with lower cost, superior mechanical properties and more functional groups [21], Baran et al., (2020) [22]. In previous work [23], core-brush-shaped aromatic rings-modified chitosan has been prepared and adsorption of pharmaceutical wastes (ketoprofen, carbamazepine, sulfamethoxazole) has been investigated. Zhou et al. [24] have synthesized metal-organic frameworks/sodium alginate and metal-organic frameworks/chitosan composites for ibuprofen and ketoprofen removal from wastewater. It has been reported that these prepared composites exhibit very good renewability over several repeated adsorption/desorption cycles of pharmaceutical wastes. In another study prepared with chitosan-based composite, a magnetic composite was prepared with grafting co-polymerization on the surface of chitosan/Fe_3O_4 particles to investigate the adsorption performance of diclofenac sodium (anti-inflammatory drug) and tetracycline hydrochloride (antibiotic) pharmaceuticals [25]. Chen et al. [26] have investigated the removal of ketoprofen by porous chitosan, advanced

crystalline materials such as UiO-66 and linking agent (epichlorohydrin) to obtain suitable composite foams (CSF@UiO-66).

Cellulose (non-toxic biocompatible, and sustainable material), the most abundant polysaccharide in nature, is generally obtained from plants. Cellulose is an important component of the plant cell wall, so it forms an important part of the plant structure. Cellulose acetate is also a common polymer that is frequently used to create composite materials with its porous structure, and its adsorption capacity is also quite good. The removal of diclofenac sodium and tetracycline pharmaceutical wastes was searched by cellulose acetate-Mg-Al layered double hydroxide nanocomposite membranes from wastewater [27] In the proportioning of the composite, the increase of Mg-Al (4%) increased the adsorption capacity of both pharmaceuticals.

The effectiveness of biochar, which is a very good alternative adsorbent obtained by thermal decomposition of biomass in the absence of oxygen (pyrolysis) and at very high temperatures (<700 ◦C), ineffective adsorption of pharmaceutical compounds in its highly porous carbonaceous structure is accepted by studies in the literature. ZnAl/biochar composite was synthesized as an alternative adsorbent for removing acetaminophen, ketoprofen, and ibuprofen in a study by Moreno-P´erez et al. [28]. Maximum adsorption capacity was found as 1,108.43, 1,081.35, and 1,032.81 mg/g for acetaminophen, ketoprofen, and ibuprofen onto ZnAl/biochar composite, respectively.

Table 1. Summarize pharmaceuticals adsorption by composites

Composite	Pharmaceutical Waste	Adsorption Capacity (mg/g)	Isotherm model	Kinetic model	Method	Reference
zimidazolate framework / zinc oxide nanocomposite	Tetracycline	-	Langmuir	Pseudo-second	UV–Vis spectrophotometer	[29]
ZnAl/biochar	acetaminophen, ketoprofen, and ibuprofen	1,108.43, 1,081.35, 1,032.81	Freundlich/ Henry	-	UV-spectrophotometry	[28]
gelatins and carbon nanotubes	diclofenac sodium	20.57	Freundlich	Pseudo-second	UV-spectrophotometry	[20]

lignocellulosic waste biomass-based carbonaceous	ketoprofen, carbamazepine, sulfamethoxazole	19.675, 21.895, 19.181	Langmuir	Pseudo-second	HPLC	[19]
sugarcane ash/polyethylene terephthalate /iron	diclofenac, naproxen	3.243, 9.564	-	-	HPLC	[36]
corncob biochar-based montmorillonite	atenolol	47.29	Freundlich	Pseudo-second	UV-Vis spectrophotometry	[31]
core-brushes shaped chitosan/Fe3O4	norfloxacin, tylosin, diclofenac sodium	165, 134, 151	Langmuir	Pseudo-first	UV-Vis spectrophotometry	[23]
metal-organic frameworks/sodium alginate and metal-organic frameworks/chitosan	ibuprofen, ketoprofen	-	Redlich-Peterson (Freundlich &Langmuir)	Pseudo-second	UV-Vis spectrophotometry	[24]
chitosan-based magnetic composite particles	diclofenac sodium, tetracycline	100, 35	Langmuir	Pseudo-second	UV-Vis spectrophotometry	[25]
chitosan-advanced crystalline materials(UiO-66)	Ketoprofen	209.7	Langmuir	Pseudo-second	UV-Vis spectrophotometry	[26]
metal–organic frameworks-magnetic Cellulose acetate/layered double hydroxide adsorptive membranes	etracycline, diclofenac sodium	745, 277	Langmuir	Pseudo-second	HPLC	[30]

cellulose acetate-layered double hydroxide adsorptive membranes	diclofenac sodium, tetracyclinecipro floxacin	%21	-	-	UV-Vis spectrophotom etry	[27]
zeolite-carbon	ciprofloxacin	%92	Freundlich	Pseudo-second	UV-Vis spectrophotom etry	[33]
magnetic polymer/clay composite	atenolol, ciprofloxacin and gemfibrozil	15.6, 39.1, 24.8	Freundlich	-	HPLC	[32]

Magnetic can be used to produce photo-regenerable, recyclable, and efficient composite. Metal-organic frameworks that functionalized with magnetic (Fe_3O_4) successfully prepared to obtain a suitable composite to determine the adsorption of tetracycline and diclofenac sodium with excellent adsorption capacities of 745 and 277 mg/g, respectively [30].

Known for its hydrophilic nature, clay is a natural adsorbent and its ability to add pharmaceuticals to the layered structure has encouraged its use in drug delivery. Also, since the applicability of pure clay has been limited to cationic pollutants until now; clay is modified by various techniques using organic polymers, magnetic particles, cations, and metals. In a study [31], a corncob biochar-based montmorillonite composite was synthesized and used for the adsorption of Atenolol, a pharmaceutically occurring organic pollutant. The adsorption capacity of Atenol on corncob biochar was determined as 47.29 mg/g. In another study, atenolol (beta-blocker), ciprofloxacin (antibiotic) and gemfibrozil (lipid regulator) were adsorbed by using magnetic polymer/clay composite [32]. Synthesized pellet's surface area the was mesoporous surface (94.81 m^2/g) and maximum adsorption capacities were found to be 15.6 for atenolol, 39.1 for ciprofloxacin and 24.8 mg/g for gemfibrozil. It was reported that zeolite/carbon composite adsorbent was prepared and the adsorption capacity of ciprofloxacin from wastewater was studied [33]. In this study, experimental data has fitted with pseudo-second-order kinetic model and Freundlich isotherm model.

Large amounts of waste produced by the food industry pollute the environment, and most of these residues can be recycled and used in removal studies. Thus, agricultural wastes are attracting attention as a highly sought-after

raw material as a candidate for water pollution control due to their low cost and availability [34]. Modifications of agricultural wastes are generally essential to improve their performance in adsorption. In recent years, the use of agricultural wastes has been the focus of great interest for researchers due to their abundance and cheapness in the adsorption of pharmaceutical wastes. For example, in one study, Yin et al. [35] investigated tylosin removal studies using a goethite-straw mass composite. A pharmaceutical waste removal study was also carried out by Américo-Pinheiro et al. [36] that has used heavy sugarcane ash fused with polyethylene terephthalate and functionalized with iron to produce a low-cost composite for the removal of diclofenac and naproxen. In another similar study, lignocellulosic waste biomass-based carbonaceous adsorbent has been synthesized by Coimbra et al. [34] for investigation of ketoprofen, carbamazepine and sulfamethoxazole adsorption and 99%, the excellent removal efficiency was found (19.675, 21.895, 19.181 mg/g).

3. CONCLUSION

Due to the discharge of all these domestic, hospital, industrial and agricultural wastes, pharmaceutical residues are frequently encountered in the soil, surface and underground waters. Wastewaters containing these pharmaceutical residues also cause deadly health risks due to their toxic nature, as they contain toxic and carcinogenic elements. It has been determined by the studies that the composite materials in different structures prepared in adsorption studies to remove all these pollutions are quite effective. Looking at the last few decades, numerous literature reviews have been published regarding the use of different composite adsorbents e.g. chitosan, cellulose, clay, agricultural waste, metal oxide, and biochar based for the removal of wastewater pharmaceutical wastes while preparing the composite in the studies; materials with cheap, regenerable, abundant, easily modified, and high adsorption capacity is preferred. It is observed by the literature studies that the prepared composite adsorbents generally comply with the Langmuir isotherm model and the pseudo-second kinetic model, in addition to their good adsorption capacity in the removal of pharmaceutical wastes. Studies have shown that composite materials are very effective in the removal of pharmaceutical wastes, and with new future studies, composites with a newer perspective can be prepared and used in the removal of pharmaceutical wastes and other organic pollutants.

REFERENCES

[1] Kim Y. Choi K. Jung J., Park S., . Kim P.G, Park J. Aquatic toxicity of acetaminophen, carbamazepine, cimetidine, diltiazem and six major sulfonamides, and their potential ecological risks in Korea. *Environ. Int.*, 33, 2007, 370-375.

[2] Yıldırım A., Acay H. Biosorption studies of mushrooms for two typical dyes. *Journal of the Turkish Chemical Society Section A: Chemistry.* 2020, 295-306.

[3] Cleuvers M. Aquatic ecotoxicity of pharmaceuticals including the assessment of combination effects. *Toxicol. Lett.,* 142, 2003, 85-194.

[4] Vieira Y., Lima E.C., Foletto E.L., Dotto G.L. Microplastics physicochemical properties, specific adsorption modeling and their interaction with pharmaceuticals and other emerging contaminants. *Science of The Total Environment*, 753, 2021, 141981.

[5] Kyzas G.Z., Kostoglo M., Lazaridis N.K., Lambropoulou D.A., Bikiaris D.N. Environmental Friendly Technology for the Removal of Pharmaceutical Contaminants from Wastewaters Using Modified Chitosan Adsorbents. *Chemical Engineering Journal*, 222, 2013, 248-258.

[6] Petrie B., Barden R., Kasprzyk-Hordern B. A review on emerging contaminants in wastewaters and the environment: Current knowledge, understudied areas and recommendations for future monitoring. *Water Res.*, 72, 2015, 3-27.

[7] Rai P.K., Sonne K., Brown R.J.C., Younis S.A., Kim K.H. Adsorption of environmental contaminants on micro- and nano-scale plastic polymers and the influence of weathering processes on their adsorptive attributes. *Journal of Hazardous Materials*, 427, 2022, 127903.

[8] Ahmed M.J., Hameed B.H. Removal of emerging pharmaceutical contaminants by adsorption in a fixed-bed column: A review. *Ecotoxicology and Environmental Safety,* 149, 2018, 257-266.

[9] Yildirim A., Baran M. F., Acay H. Kinetic and isotherm investigation into the removal of heavy metals using a fungal-extract-based bio-nanosorbent. *Environmental Technology & Innovation*, 20, 2020.

[10] Yildirim A., Acay H., Baran F. Synthesis and characterisation of mushroom-based nanocomposite and its efficiency on dye biosorption via antimicrobial activity, International Journal of Environmental Analytical Chemistry, 102:7, 2022, 1545-1562.

[11] Yıldırım A., Acay H., Baran A. Synthesis and characterization of molecularly imprinted composite as a novel adsorbent and competition

with non-imprinting composite for removal of dye. *Journal of the Turkish Chemical Society Section A*: Chemistry, 2021; 609-622.

[12] Fernández-Reyes B., Morales-Jiménez S., Muñoz-Senmache J.C., Vega-Santander D.R., Hernández-Maldonado A.J. Single- and multi-component adsorption of selected contaminants of emerging concern from water and some of their metabolites onto hierarchical porous copper(II)-zeolite - activated carbon composite. *Microporous and Mesoporous Materials,* 312, 2021, 110355.

[13] Samuel M.S., Savunthari K.V., Chandrasekar N., Balaji R., Selvarajan E. Removal of environmental contaminants of emerging concern using metal–organic framework composite. *Environmental Technology & Innovation*, 25, 2022, 102216.

[14] Lessa E.F., Nunes M.L., Fajardo A.R. Chitosan/waste coffee-grounds composite: An efficient and eco-friendly adsorbent for removal of pharmaceutical contaminants from water. *Carbohydrate Polymers*, 189, 2018, 257-266.

[15] Ruan C., Ma Y., Shi G., He C., Du C., Jin X., Liu X., He S., Huang Y. Self-assembly cellulose nanocrystals/SiO_2 composite aerogel under freeze-drying: Adsorption towards dye contaminant. Applied Surface Science, 592, 2022, 153280.

[16] Darabdhara, J. Ahmaruzzaman Md. Recent developments in MOF and MOF based composite as potential adsorbents for removal of aqueous environmental contaminants. *Chemosphere*, 304, 2022, 135261.

[17] Taoufik N., Elmchaouri A., Anouar F., Korili S.A., Gil A. Improvement of the adsorption properties of an activated carbon coated by titanium dioxide for the removal of emerging contaminants. *Journal of Water Process Engineering*, 31, 2019, 100876.

[18] Khalid Q., Khan A., Bhatti H.N., Sadaf S., Kausar A., Alissa S.A., Alghaith, M.K. Iqbal M. Cellulosic biomass biocomposites with polyaniline, polypyrrole and sodium alginate: Insecticide adsorption-desorption, equilibrium and kinetics studies. *Arabian Journal of Chemistry*, 14:7, 2021, 103227.

[19] Sekulic M.T., Boskovic N., Milanovic M., Letic N.G., Gligoric E., Pap S. An insight into the adsorption of three emerging pharmaceutical contaminants on multifunctional carbonous adsorbent: Mechanisms, modelling and metal coadsorption. *Journal of Molecular Liquids*, 284, 2019, 372-382.

[20] Rigueto C.V. T., Rosseto M., Nazari M.T., Ostwald B.E.P., Alessandretti I., Manera C., Piccin J.S., Dettmer A. Adsorption of diclofenac sodium by

composite beads prepared from tannery wastes-derived gelatin and carbon nanotubesİ. *Journal of Environmental Chemical Engineering,* 9:1, 2021, 105030.

[21] Quesada H.B., Peixoto de Araújo T., Vareschini D.T., de Barros M.A.S.D., Gomes R.G., Bergamasco R. Chitosan, alginate and other macromolecules as activated carbon immobilizing agents: A review on composite adsorbents for the removal of water contaminants. *International Journal of Biological Macromolecules*, 164, 2020, 2535-2549.

[22] Baran M.F., Yildirim A., Acay H., Keskin C., Aygun H. Adsorption performance of *Bacillus licheniformis* sp. bacteria isolated from the soil of the Tigris River on mercury in aqueous solutions, *International Journal of Environmental Analytical Chemistry*, 102:9, 2022, 2013-2028.

[23] Zhou X., Dong C., Yang Z., Tian Z., Lu L., Yang W., Wang Y., Zhang L., Li A., Chen J. Enhanced adsorption of pharmaceuticals onto core-brush shaped aromatic rings-functionalized chitosan magnetic composite particles: Effects of structural characteristics of both pharmaceuticals and brushes. *Journal of Cleaner Production*, 172, 2018, 1025-1034.

[24] Zhuo N., Lan Y., Yang W., Yang Z., Li X., Zhou X., Liu Y., Shen J., Zhang X. Adsorption of three selected pharmaceuticals and personal care products (PPCPs) onto MIL-101(Cr)/natural polymer composite beads. *Separation and Purification Technology*, 177, 2017, 272-280.

[25] Zhang S., Dong Y., Yang Z., Yang W., Wu J., Dong C. Adsorption of pharmaceuticals on chitosan-based magnetic composite particles with core-brush topology. *Chemical Engineering Journal*, 304, 2016, 325-334.

[26] Chen J., Ouyang J., Chen W., Zheng Z., Yang Z., Liu Z., Zhou L. Fabrication and adsorption mechanism of chitosan/Zr-MOF (UiO-66) composite foams for efficient removal of ketoprofen from aqueous solution. *Chemical Engineering Journal*, 431, Part 2, 2022, 134045.

[27] Raicopol M.D., Andronescu C., Voicu S.I., Vasile E., Pandele A.M. Cellulose acetate/layered double hydroxide adsorptive membranes for efficient removal of pharmaceutical environmental contaminants. *Carbohydrate Polymers*, 214, 2019, 204-212.

[28] Moreno-Pérez J., Pauletto P.S., Cunha A.M., Bonilla-Petriciolet Á., Salau N.P.G., Dotto G.L. Three-dimensional mass transport modeling of pharmaceuticals adsorption inside ZnAl/biochar composite. *Colloids and Surfaces A: Physicochemical and Engineering Aspects*, 614, 2021, 126170.

[29] Ahmadi S. A. R., Kalaee M.R., Moradi O., Nosratinia F., Abdouss M. Synthesis of novel zeolitic imidazolate framework (ZIF-67) – zinc oxide

(ZnO) nanocomposite (ZnO@ZIF-67) and potential adsorption of pharmaceutical (tetracycline (TCC)) from water. *Journal of Molecular Structure*, 1251, 2022, 132013.

[30] Zhao F., Fang S., Gao Y., Bi J. Removal of aqueous pharmaceuticals by magnetically functionalized Zr-MOFs: Adsorption Kinetics, Isotherms, and regeneration. *Journal of Colloid and Interface Science*, 615, 2022, 876-886.

[31] Fu C., Zhang H., Xia M., Lei W., Wang F. The single/co-adsorption characteristics and microscopic adsorption mechanism of biochar-montmorillonite composite adsorbent for pharmaceutical emerging organic contaminant atenolol and lead ions. *Ecotoxicology and Environmental Safety*, 187, 2020, 109763.

[32] Arya V., Philip L. Adsorption of pharmaceuticals in water using Fe3O4 coated polymer clay composite. *Microporous and Mesoporous Materials*, 232, 2016, 273-280.

[33] Al-Jubouri S.M., Al-Jendeel H.A., Rashid S.A., Al-Batty S. Antibiotics adsorption from contaminated water by composites of ZSM-5 zeolite nanocrystals coated carbon. *Journal of Water Process Engineering*, 47, 2022, 102745.

[34] Escapa C.R.N., C., Otero, M. Adsorption Separation of Analgesic Pharmaceuticals from Ultrapure and Waste Water: Batch Studies Using a Polymeric Resin and an Activated Carbon. *Polymers*, 10:9, 2018, 958.

[35] Yin Y.Y. , Guo X.T., Yang C., Gao L.M., Hu Y.B. An efficient method for tylosin removal from an aqueous solution by goethite modified straw mass. *RSC Adv.*, 98, 2016, 95425-95434.

[36] Américo-Pinheiro J.H.P., Salomão G.R., Paschoa C.V.M., Cruz I.A.,. Isique W.D, Ferreira L.F.R., Torres N.H., Bilal M., Iqbal H.M.N., Sillanpää M., Nadda A.K. Effective adsorption of diclofenac and naproxen from water using fixed-bed column loaded with composite of heavy sugarcane ash and polyethylene terephthalate. *Environmental Research*, 211, 2022, 112971.

Chapter 4

Grand Story of a Tiny Particle:Neutrino

Çağın KAMIŞCIOĞLU[1]

1 Physics Engineering Department, Faculty of Engineering, Ankara University, Ankara, Türkiye
gunesc@ankara.edu.tr

1. Introduction

When we look at the smallest building blocks of matter that make up the universe, we see that the same material is the basis of everything, the most basic things we know, namely subatomic particles. This sentence hides more than a hundred years of history behind it. During this time, thousands of people were engaged in subatomic particle physics, focused on incredible ideas, reached exciting results, and ultimately succeeded in creating a great deal of knowledge in both experimental and theoretical fields. These results are a reflection of our search for answers to the questions about the universe and ourselves. Fortunately, science is our greatest tool in understanding the world around us. As science progresses our story continues with new chapters.

Today, subatomic physics is still among the active research areas as it was in the past. Experiments are the most important part of this research. With the developing technology, our discovery of the subatomic world has accelerated and we have to examine it from a different perspective.

When I was in college, I learned that "The smallest building block of matter is the atom". This is very surprising. Because of all the diversity we see around us, the sea, the clouds, the mountains, and the apple in my hand are made up of atoms. While this statement is quite exciting even with our current knowledge and perspective today, the idea of atoms goes back 2500 years before. Democritus and Leucippus of Abdera who is the Greek philosophers proposed that when the matter is divided into parts, it cannot last forever. There must be an indivisible structure that can no longer be divided, and that is the non-divisible part of matter, namely the atom, which is a Greek word meaning "indivisible". Democritus' idea of the atom survived for centuries and was used by scientists such as Newton, Maxwell, and Mendeleev. At the beginning of the 19th century, John Dalton developed the first modern atomic theory based on an advanced understanding of chemistry. He proved that the smallest building block of matter is the atom but not just one type of atom as ancient Greek philosophers proposed. Then the studies on radioactivity and electricity showed that the atom is not the smallest building block of matter, but rather there are smaller building blocks.

In 1897, the result of the experiment, done by J.J. Thomson, was very exciting and revolutionary. He proposed the evidence of a new particle called "electron" and so he started the era of particle physics.

Thus, particle physics began to explain the fundamental particles and the relationship between them. Particles claimed in theoretical studies began to be observed and discovered over time. Today, according to the Standard Model, we are aware of the existence of 12 elementary particles, 4 force carriers, and a Higgs

boson. Among these particles neutrino, one of the most mysterious particles in this world is the main character of this study. Therefore, in this study, focusing on the neutrino particle, its historical process, neutrino experiments, and their contribution to the neutrino physics are presented.

2. The Birth of Neutrino

In today's world, X-rays are widely used in the diagnosis of diseases. If Wilhelm Roentgen, Professor of Physics, had not made this discovery in 1895, maybe they would still have to cut people to see if the bone was broken.

On the evening of November 8, Roentgen was working with a cathode ray tube (Crookes tube) in his laboratory. He realized the glow from a chemically coated screen close to the tube. It means that the cathode rays are coming out of the tube. He repeats the experiment many times. He observed that the cathode rays could escape even though he changed the tubes or covered the experimental setup with different and thick objects. From his results, Roentgen deduced that he had observed something completely new. He named his discovery "X-rays," a name that continues to this day. The discovery of X-rays, which forms the basis of today's imaging methods, was honored with the Nobel Prize in Physics in 1901.

Although no one had a clear idea of what X-rays were exactly, this news was quite interesting. Antoine Henri Becquerel immediately understood that it was his turn to move in this game. He had phosphorescent crystals containing potassium, sulfur, and uranium that he had prepared with his father years ago. Perhaps any of these crystals could emit X-rays. To test this, he wrapped the phosphorescent substance in paper to protect it from light and placed it on a photographic plate then left them in the sunlight. His first results were traces formed on photographic films, and he thought they were caused by X-rays emitted from uranium. In the following a few cloudy days, without sunlight, Becquerel couldn't energize his specimen, and he put them in his drawer together with uranium salts and photographic films. Then, when he took the films out of the drawer to develop them, he encountered traces on these films, similar to the ones exposed to the sunlight. Becquerel repeated his experiment many times and discovered that uranium salts radiated spontaneously without the need for prior stimulation by sunlight. A. H. Becquerel discovered radioactivity in 1896 while searching for X-rays in his experiment. He didn't immediately name his discover because he wanted to understand and prove what it was.

In 1898, Marie Curie and her husband Pierre tried to separate the elements in the radioactive substance pitchblende, and the work resulted in the discovery of two new elements, polonium and radium. In 1903, the Nobel Prize in Physics was awarded to A. H. Becqurel, M. Curie, and P. Curie for the discovery of natural

radioactivity. In 1899, Ernest Rutherford discovered that there are two different types of radioactivity, alpha (α) and beta (β) radiations emitted from uranium. The third type of gamma (γ) radiation was discovered by Paul Villard in 1900.

J. Chadwick discovered in 1914 that the electron energy spectrum is continuous in β decay. This seemed to violate the law of conservation of energy, and the results were expected to be tested with another system and strengthened the experimental evidence. Therefore, it took 30 years for this idea to be accepted by the physics community (Franklin 2018; Close 2004; All Nobel Prizes).

3. Observing The Tiny Particle

Since its discovery in the mid-nineteenth century, the principle of conservation of energy has been one of the fundamental principles of physics. If the claimed theory violates the conservation of energy, it is not possible to be taken seriously by the physics community. In 1930 Niels Bohr, who made foundational contributions to understanding atomic structure and quantum theory, drew attention to the problem of energy principle in the continuous beta decay energy spectrum in his lecture to the British Chemical Society. In the same year, Wolfgang Ernst Pauli, one of the pioneers of quantum physics, proposed the "desperate way out" which could solve the problem of the continuous energy spectrum in beta decay. Pauli suggested that in beta decay, there must be a third particle besides the proton and electron, that some of the energy is carried by this neutral particle so that energy can be conserved in the decay. While expressing that this particle has a very small mass and interacts with matter very rarely, it would be very difficult to observe it, he said, "I made a terrible mistake by putting forward a particle that is impossible to detect."

In 1934, Enrico Fermi, who made important contributions to physics, introduced his beta decay theory. Fermi assumed that Pauli's neutron existed and included it in his theory, calling it "neutrino". According to Fermi, beta decay was a process in which the neutron decayed into an electron, a proton, and a neutrino, postulating that electrons and neutrinos were created at the time of decay. Thus, by including the neutrino, Fermi preserved the laws of conservation of energy, momentum, and angular momentum and solved the continuous energy spectrum problem. Observing the neutrino particle would confirm this whole process.

Pauli received a telegram from Cylede Cowan in 1956. Cylede Cowan's telegram to Pauli said that the hopeless particle he had proposed had been discovered.

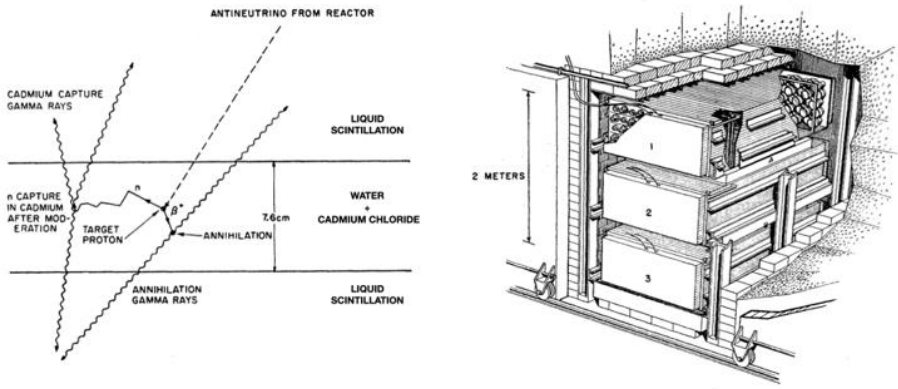

Figure 3.1. Schematic diagram and sketch of detector (Reines et al., 1960).

Reines, Cowan, and collaborators designed an experiment to detect free antineutrinos in the Savannah River nuclear reactor. The schematic drawing and outline of the experiment are shown in Figure 3.1. The detector consisted of a large scintillator tank in which approximately 300 liters of cadmium compound had been dissolved, and the tank was surrounded by 90 photomultiplier tubes that would detect the produced gamma rays. The presence of the antineutrino is implied by observing the end products of inverse beta decay. Thanks to this experiment they designed, 26 years after Pauli's proposal, Frederick Reines and Clyde Cowan observed the interactions of neutrinos formed in the Savannah River reactor in the USA. This discovery brought Frederic Reines the Nobel Prize in 1995 (Reines et al., 1960; Franklın 2018, All Nobel Prizes).

4. Are There Different Types of Neutrinos?

In the late 1950s, after the discovery of the neutrino, the most important question expected to be answered was whether there was a kind of neutrino or not. Leon Lederman, Melvin Schwartz, and Jack Steinberger answered this question in a study they carried out in 1962. Only the electron-neutrino had been discovered at the time, and scientists wondered if they could find more types of these particles. Alternate Gradient Synchrotron (AGS), the most powerful accelerator at the time, was ready to produce the needed beam.

The experiment, it is aimed to examine the neutrinos emitted from the decay of pion and kaon particles as a result of bombarding the beryllium target with protons with an energy of 15 GeV as shown in Figure 4.1. The resulting pi meson shower travels approximately 21m towards a 5,000-ton steel wall made from old battleship plates. The produced pi meson shower decayed into muons and

neutrinos on the way, but only the last particles were able to pass through the wall into a neon-filled detector called a spark chamber. The muon spark traces detected in the final stage proved the existence of muon-neutrinos. Since no electrons were observed, it was experimentally proven that the neutrinos formed were different particles from the neutrinos formed with electrons. M. Schwartz, L. Lederman, and J. Steinberger were awarded the 1988 Nobel Prize in Physics for this important discovery (Danby et al. 1962, All Nobel Prizes).

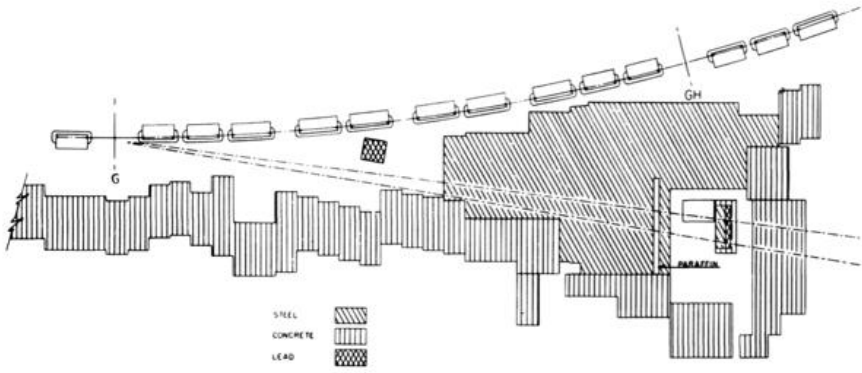

Figure 4.1. Experiment scheme of muon-neutrinos(Danby et al. 1962).

So, until the 1970s, two different types of neutrinos were obtained and questions about neutrinos were slowly being answered. Martin L. Perl and colleagues discovered a new lepton in 1975 while studying heavy leptons. The new lepton was named tau lepton. However, the great loss of energy and momentum in the decay indicated the presence of a third neutrino. This discovery brought up the same question of whether the tau neutrino exists or not. The answer to this question was given 25 years later in 2000.

Physicists were certain of the existence of the third neutron in the late 1990s. However, detecting the tau neutrino was not easy because the tau particle is the shortest-lived and most unstable particle among other leptons (roughly 2.6×10^{-13}s). To detect this kind of fast decaying particle, high-sensitivity and high-tech detectors are needed. A detector with these features was developed in the DONUT (Direct Observation of the NU Tau) experiment with a Japanese-American collaboration in the late 1990s. The DONUT experiment was designed to study ν_τCC interactions. For this purpose, a beam of 800GeV protons from the Tevatron collides with the beam dump, creating a fast neutrino beam with an average energy of 53 GeV. Charm particles (Ds) are then produced and decayed into an anti-tau neutrino and a tau lepton. The tau neutrino produces in the decays

of tau, travels 36m to reach the emulsion target. The experiment used an emulsion/counter-hybrid detector and the target consisted of nuclear emulsion as a three-dimensional tracking device as shown in Figure 4.2. Because of its submicron accuracy and high spatial resolution, the nuclear emulsion is a very powerful technique for short-lived tau particle detection. It was announced that 8 neutrino interactions were observed in the experiment in 2000, 25 years after the discovery of tau lepton.(Kamışcıoğlu 2022;Kodama et al. 2001).

With the discovery of this last member of the lepton family, we now know that the three charged leptons, the electron, muon, and tau, are emitted along with the electron neutrino, the muon neutrino, and the tau neutrino.

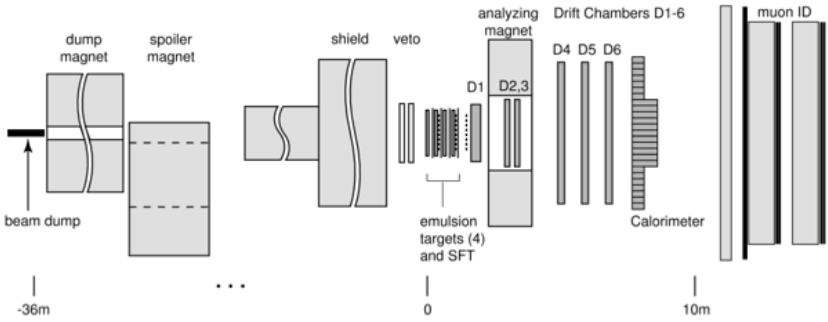

Figure 4.2. Experiment scheme of DONUT Experiment.(Kodama et al. 2001)

5. The Neutrino Shows Mysterious Properties

Since the pioneering days of the late 1950s, neutrino sources in the universe have been tried to be explained or proven. It is possible to divide neutrino sources into two main topics as natural and artificial sources. Neutrinos are formed on a scale ranging from MeV to GeV in these sources.

John N. Bahcall, an American astrophysicist, has been working on the Sun since 1960. But his main interest was neutrinos emitted from the Sun. Bahcall made important calculations to measure the number of neutrinos emitted at different stages of the Sun's fusion chain. John N. Bahcall, an American astrophysicist, has been working on the Sun since 1960. But his main interest was neutrinos emitted from the Sun. Bahcall made important calculations to measure the number of neutrinos emitted at different stages of the Sun's fusion chain. His work with experimental chemist Raymond Davis on a project to detect solar neutrinos launched the long-run Homestake experiment in 1964. In 1965, Homestake began searching for solar neutrinos using approximately 390.000 liters of dry-cleaning fluid (liquid tetrachloroethylene) in the Homestake gold

mine at Lead, South Dakota. The detector shown in Figure 5.1 is therefore placed underground to avoid cosmic interactions. Neutrinos from the Sun were tried to be observed by chlorine-neutrino interaction in the dry-cleaning fluid. The experiment was successful and solar neutrinos were confirmed in 1968. But the number found in the experiment was smaller than John Bahcall's calculation, leading to the solar neutrino puzzle (Davis et al., 1968; Bahcall and Davis 1989).

The Homestake experiment continued to collect data for over twenty years, eventually, the observed event rate was only about 30% of the Solar Model prediction. Why did only 30% o of the neutrinos formed in the Sun reach the Earth? Although Ray Davis's results were confirmed by different experiments, this situation was referred to as the solar neutrino problem in the literature.

The apparent inconsistency between the results and the predictions caused both surprise and disappointment for Bahcall and Davis. Various ideas which caused long discussions were put forward by the physics communities. Many issues from deficiencies in the model or calculations in the experimental process were discussed. This point, which seems like an unsolvable puzzle, is the point where the neutrino particle reveals its mystery called oscillation.

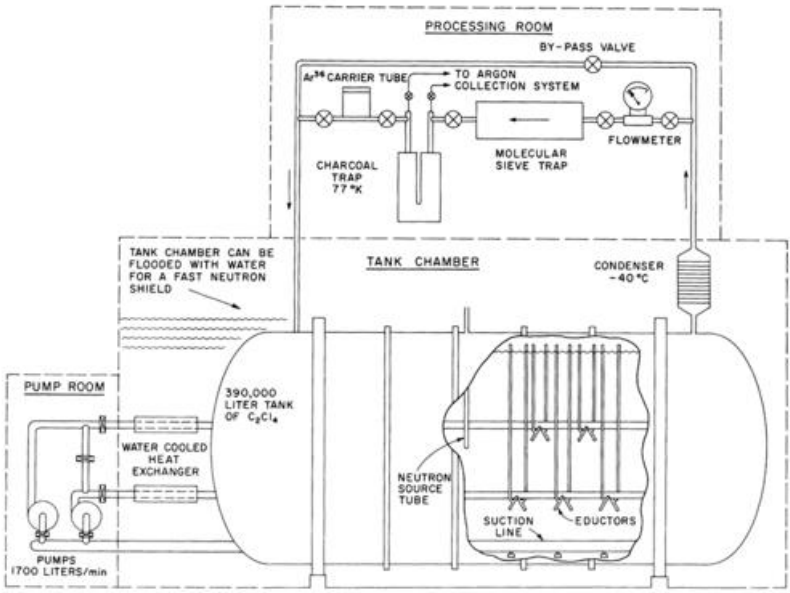

Figure 5.1.Schematic view of Homestake Experiment.(Davis et al., 1968)

6. A New Era in Neutrino Physics

While searching for answers to questions about neutrinos, Bruno Pontecorvo, one of the pioneers of neutrino physics, created a new era in neutrino physics with his idea. At that time, B. Pontecorvo was very impressed by the possibility of oscillation of the kaon to the antikaon particle proposed by Gell-Mann and Pais in 1955(Gell-Mann and Pais 1955). Similarly, he thought about the oscillation in the lepton sector and tried to prove that there could be an oscillation between the neutrino and the antineutrino. However, this oscillation has never been observed. After the discovery of the muon neutrino, the idea of flavor oscillations was proved by Maki, Nakagawa, and Sakata in 1962. In the same year, Japanese physicist Ziro Maki suggested that this transformation may also occur between neutrino flavors. If this prediction is correct, some of the electron neutrinos coming from the Sun are transformed into another type of neutrino from the point where they were born until they reach the Earth, and due to this change, the electron neutrinos could not be detected.

Neutrinos are very difficult particles to detect due to their reluctance to interact. Detecting neutrinos in a detector becomes a game of chance because of their features such as the absence of electric charges and their oscillation. To increase the probability of seeing a neutrino in a detector, various methods must be applied to further interact with neutrinos. For this reason, attempts to detect the neutrino led to the construction of the world's largest particle detectors. Various experiments have been carried out in the past to solve the solar neutrino problem and detect neutrinos from the Sun like Homestake (Cleveland et. al 1998), Kamiokande (Fukuda, Y., et al., 1996), GALLEX (Hampel, W.,et al.1999), SAGE (Abdurashitov, J. N., et al. 2002), GNO(Altmann, et al. 2000) and SNO (Ahmed, S. et al. 2004).

The first clue that neutrinos oscillate was partially clarified 20 years later in 1998 by the Super-Kamiokande experiment. Super-Kamiokande is a Cherenkov detector containing 50 kt of ultrapure water. The experiment, set up in Mozumi mine northwest of Tokyo, was able to detect neutrino interactions in 1998 with more than 10,000 PMTs tubes placed on inner walls. The analysis of neutrino interactions recorded by the Super-Kamiokande experiment between 1996 and 1998 showed that the number of atmospheric neutrinos arriving at the top of the Mozumi Mine was different from the number of neutrinos coming from the lower part. In fact, the number of incoming muon neutrinos was expected to be equal. The results obtained do not directly indicate the neutrino flavors, but oscillation has been proven with this experiment. Similar evidence of neutrino oscillation came in 2002 from the Sudbury Neutrino Observatory (SNO) in Canada (Ahmad, et al. 2001; Ahmad, et al. 2002). The experiment, a heavy water-Cherenkov

detector, was sensitive to electron neutrinos via CC and was located about 2 km below the ground. The detector, which started to receive data in 1999, showed that two-thirds of the neutrinos coming from the sun oscillate until they reach the detector and turn into another neutrino flavor as a result of the analysis of the charged and neutral interactions. Thus, SNO completely solved the long-lasting solar neutrino problem and showed that the experimental results of R. Davis and the theoretical calculations of J. H. Bahcall were correct. Ray Davis was awarded the Nobel Prize in 2002 for his work on the Solar neutrino. Similarly, Takahaki Kajita and Art McDonald were jointly awarded the Nobel Prize in 2015 for the discovery of neutrino oscillations in collaboration with Super-Kamiokande.

Humanity's interest in the neutrino particle has always continued in the historical process. In addition to the oscillation experiments mentioned above, many experiments with different purposes but mainly examining neutrinos have been carried out using man-made beams from accelerators and nuclear reactors. Some of them can be listed as; Borexino (Bellini, et al. 2011) MINOS (Adamson, et al. 2013), T2K (Abe, et al. 2014), NOνA (Sanchez, 2015), Double Chooz (Abe, et al.2012), Daya Bay (Zhang, 2014) and RENO (Choi, et al. 2016) and KamLAND (Gando, et al. 2011), DONUT (Kodama, et al. 2002), CHORUS (Eskut, et al., 1997), OPERA (Agafonova, et al. 2013).

Thanks to the remarkable discoveries made by a series of neutrino oscillation experiments carried out in history, we have accumulated a great knowledge of neutrino physics. However, today, experiments and studies on this mysterious particle continue. Among new generation experiments carried out recently CHORUS (CERN Hybrid Oscillation Research ApparatUS), DONUT (Direct Observation of Nu-Tau), and OPERA (The Oscillation Project with Emulsion-tRacking Apparatus) have successfully used nuclear emulsion technology. The tau neutrino was discovered in 2000 using emulsion technology in the DONUT experiment. Following this discovery, the OPERA experiment recorded a total of 19505 neutrino interactions in 2008-2012. Using the nuclear emulsion technique, OPERA was able to observe 5 $\nu_{\mu} \rightarrow \nu_{\tau}$ oscillations with an accuracy of 5.1σ and a background event of 0.25 $\pm$0.05. This observation, made for the first time in the appearance mode, is proof that the neutrino is oscillating (Agafonova, et al. 2018; Agafonova, et al. 2019; All Nobel Prizes).

7. Conclusion

Looking at the neutrino's more than 100-year history, we can see that there are pretty good reasons to believe it exists. From the observation of the continuous energy spectrum in beta decay to recent work on neutrino oscillations, numerous

studies have provided a tremendous body of knowledge in the field of neutrino physics. In each of these experiments, neutrinos behaved as electrically neutral, spin 1/2, have helicity, had a very small mass, oscillating, and come in three varieties of particles.

The Standard Model in particle physics was created to explain the basic building blocks of matter and the interactions between them. The theoretical and experimental results obtained so far showed that the Standard Model has made significant progress toward becoming a consistent model within itself. However, we also know that there are many problems that the model fails to explain. One of them is the mass of the neutrino. The oscillation of the neutrino, which is defined as a massless particle in the Neutrino Standard Model, indicates that the neutrino has a small but nonzero mass. So if the neutrino's mass is nonzero, it means the birth of new physics beyond the Standard Model.

It is of course always possible to discover new things. But to predict what might happen, we need to have a good understanding of the information we have. Dozens of scientists in history have made great efforts to understand the neutrino particle because the neutrino has also been successfully used to investigate other aspects of nature. Today, thanks to high technology, particle detectors with very high resolution are designed and successful results are obtained. There are still many experiments are designed or in preparation. The purpose of these experiments is the same as the purpose 100 years ago; to reveal the truth about the nature of the neutrino particle. Thus, the new information we will obtain will be added to our existing knowledge and will enable us to better understand the universe we live in, and in fact, to know ourselves better.

References

1. Abdurashitov, J. N., et al. (2002). Solar neutrino flux measurements by the Soviet-American gallium experiment (SAGE) for half the 22-year solar cycle. Journal of Experimental and Theoretical Physics, 95(2), 181–193. https://doi.org/10.1134/1.1506424.
2. Abe, Y. et al. (2012). Reactor electron antineutrino disappearance in the Double Chooz experiment, Phys. Rev. D 86 (2012) 052008, http://dx.doi.org/ 10.1103/PhysRevD .86.052008
3. Abe, K. et al. (2014). Precise measurement of the neutrino mixing parameter θ23 from muon neutrino disappearance in an off-axis beam, Phys. Rev. Lett. 112 (18) (2014) 181801, http://dx.doi.org/10.1103/PhysRevLett.112.181801.
4. Adamson, P. et al.(2013). Measurement of neutrino and antineutrino oscillations using beam and atmospheric data in MINOS, Phys. Rev. Lett. 110 (25) (2013) 251801, http://dx.doi.org/10.1103/PhysRevLett.110.251801.
5. Agafonova, N., et al. (2013). New results on $\nu\mu \rightarrow \nu\tau$ appearance with the OPERA experiment in the CNGS beam, Journal of High Energy Physics, 36(11):1-31.
6. Agafonova, N., et al. (2018). Final results of the OPERA Experiment on $\nu\tau$ Appearance in the CNGS Neutrino Beam, Physical Review Letters, 120(21):1-7.
7. Agafonova, N., et al. (2019). Final results on neutrino oscillation parameters from the OPERA experiment in the CNGS beam, Physical Review D, 100(051301):1-8.
8. Ahmad, Q. R., et al. (2001).Measurement of the Rate of νe+d→p+p+e− Interactions Produced by 8B Solar Neutrinos at the Sudbury Neutrino Observatory Physical Review Letters 87: 071301.
9. Ahmad, Q. R., et al. (2002). Direct evidence for neutrino flavor transformation from neutral current interactions in the Sudbury Neutrino Observatory. Phys.Rev.Lett. 89 (2002) 011301
10. Ahmed, S. et al. (2004).Measurement of the total active B-8 solar neutrino flux at the Sudbury Neutrino Observatory with enhanced neutral current sensitivity. Phys. Rev. Lett., 92, 181301.
11. Altmann, M., et al. (2000). GNO solar neutrino observations: results for GNO I. Physics Letters B, 490(1–2), 16–26. https://doi.org/10.1016/s0370-2693(00)00915-1
12. All Nobel Prizes. NobelPrize.Org., from https://www.nobelprize.org/prizes/lists/all-nobel-prizes/. Erişim tarihi 30.08.2022.

13. Bahcall, J. N., and R. Davis (1989). "An Account of the Development of the Solar Neutrino Problem". In Neutrino Astrophysics. J. N. Bahcall, Cambridge, England: Cambridge University Press, pp. 487-530.
14. Bellini, G. et al. (2011). Precision measurement of the 7 Be solar neutrino interaction rate in Borexino, Phys. Rev. Lett. 107,141302, http://dx.doi.org/10.1103/PhysRevLett.107.141302
15. Choi, J., et al.(2016). Observation of Energy and Baseline Dependent Reactor Antineutrino Disappearance in the RENO Experiment. Physical Review Letters, 116(21). https://doi.org/10.1103/physrevlett.116.211801
16. Cleveland, B. T., Daily, T., Davis, Jr., R., Distel, J. R., Lande, K., Lee, C. K., Wildenhain, P. S., & Ullman, J. (1998). Measurement of the Solar Electron Neutrino Flux with the Homestake Chlorine Detector. The Astrophysical Journal, 496(1), 505–526. https://doi.org/10.1086/305343
17. Close, F. (2004). Particle Physics: A Very Short Introduction (1st ed.). Oxford University Press.
18. Danby, G., J.-M. Gaillard, K. Goulianos, et al. (1962). "Observation of High-energy Neutrino Interactions and the Existence of Two Kinds of Neutrinos." Physical Review Letters 9: 36-44.
19. Davis, R., D. S. Harmer, and K. C. Hoffman (1968). "Search for Neutrinos from the Sun." Physical Review Letters 20: 1205-1209.
20. Eskut, E., et al., 1997. The CHORUS experiment to search for $\nu\mu \rightarrow \nu\tau$ oscillation, Nuclear Instruments and Methods ın Physics Research A, 401:7-44.
21. Franklin, A. (2018). Are There Really Neutrinos? An Evidential History. Published 2018 by CRC Press Taylor & Francis Group.
22. Fukuda, Y., et al. (1996). Solar Neutrino Data Covering Solar Cycle 22. Physical Review Letters, 77(9), 1683–1686. https://doi.org/10.1103/physrevlett.77.1683
23. Gando, A. et al., (2011). Constraints on θ13 from a three-flavor oscillation analysis of reactor antineutrinos at KamLAND, Phys. Rev. D 83 (2011) 052002, http://dx.doi.org/10.1103/PhysRevD.83.052002, arXiv:1009.4771.
24. Gell-Mann M., and Pais A., (1955)“Behavior of neutral particles under charge conjugation,” Physical Review, vol. 97, no. 5, pp. 1387– 1389, 1955.
25. Hampel, W., et al. (1999). GALLEX solar neutrino observations: results for GALLEX IV. Physics Letters B, 447(1–2), 127–133. https://doi.org/10.1016/s0370-2693(98)01579-2
26. Kamışcıoğlu, Ç (2022). Log-normal and Negative Binomial Distributions of DONUT Data. Celal Bayar Üniversitesi Fen Bilimleri Dergisi, 18(2), 181 - 184. 10.18466/cbayarfbe.986699

27. Kodama, K., et al. (2001).“ Observation of TAU Neutrino Interactions.” Physics Letters B, vol. 504, no. 3, 2001, pp. 218–224., https://doi.org/10.1016 s0370-2693(01)00307-0.
28. Kodama, K. et al., 2002. Detection and analysis of tau–neutrino interactions in DONUT emulsion target. Nuclear Instruments and Methods in Physics Research A, 493:45–66.
29. Reines, E, C. L. Cowan, E B. Harrison, et al. (1960). "Detection of the Free Antineutrino." Physical Review 117: 159-173.
30. Sanchez, M.(2015). Results and prosects from the NOνA experiment, talk given at the XVII International Workshop on Neutrino Factories and Future Neutrino Facilities, Rio de Janeiro, Brazil, August 10–15, 2015.
31. Zhang, C.(2014). Recent results from Daya Bay, talk given at the XXVI International Conference on Neutrino Physics and Astrophysics, Boston, USA, June 2–7, 2014.

Chapter 5

Homology Modeling And Importance

Gizem KÖPRÜLÜLÜ KÜÇÜK[1]

1 Öğr. Gör. Dr., İstanbul Şişli Meslek Yüksekokulu, gizem.koprululu@sisli.edu.tr,
ORCID iD: 0000-0001-6667-4532

A homology modeling method is an approach in which a protein whose structure has been determined experimentally by x-ray crystallography or nuclear magnetic resonance spectroscopy (NMR) studies is used as a template and the three-dimensional (3D) structure of the target protein is determined based on similarities (1). Homology Modeling takes advantage of the fact that evolutionarily related proteins with similar sequences as measured by sequence identity have similar structures. Sequence id describes the length of the branch between two proteins of a phylogenetic tree. Amino acid sequences determine the 3D structure and function of the protein. Similar amino acid sequences have adapted to form similar structures throughout their evolution. Homology modeling techniques can obtain structures that are close the reality based on this knowledge (2).

The modeling process can be divided into 5 steps: (3,4,5,6).

1. Obtaining the appropriate template for the target sequence, these templates will select from the PDB
2. Alignment of the target sequence with the templates.
3. Alignment of 3D model coordinates
4. Replacement with rotamers taking into account stereochemical criteria, with mutated side chains and limited energy optimization.
5. The validation process is carried out.

Homology Modelling Studies With Swiss-Model

The Swiss Institute of Bioinformatics (SIB) is an independent research institute in Switzerland. SIB presents the collected bioinformatics information to the world. The Swiss-Model program presents the 3D protein structures to the user with a report. This report shows predictive models and templates, sequence similarities, resolution, GMQE, Global Model Quality Estimation, and QMEAN. First, an available model for the study is selected and this file is downloaded. The coordinate data of all atoms of the modeled protein in the three-dimensional spatial system are included in the file. The file extension of these themes is ".pdb".(7).

Model Selection

Swiss-Model is a data library containing experimentally determined protein models derived by the Protein Data Bank. It serves as the main repository of the structural information required for modeling studies. While studying homology, the Swiss-Model program uses themes with similar biological and chemical functions. The theme selection of the model is proportional to the common

sequence. Models with high sequence parity are selected. Swiss-Model offers the theme automatically in the theme selection. Sequence similarity in model selection is important in terms of resolution, GMQE, and QMEAN model suitability (8).

Figure 1 shows the protein model of the SARS nCoV2 spike domain from the Swiss model library. QMEAN value is used to select the most suitable model. The ideal model is the model of the QMEAN value closest to +1, and after selection, the model is downloaded to the computer as a file with a .pdb extension.

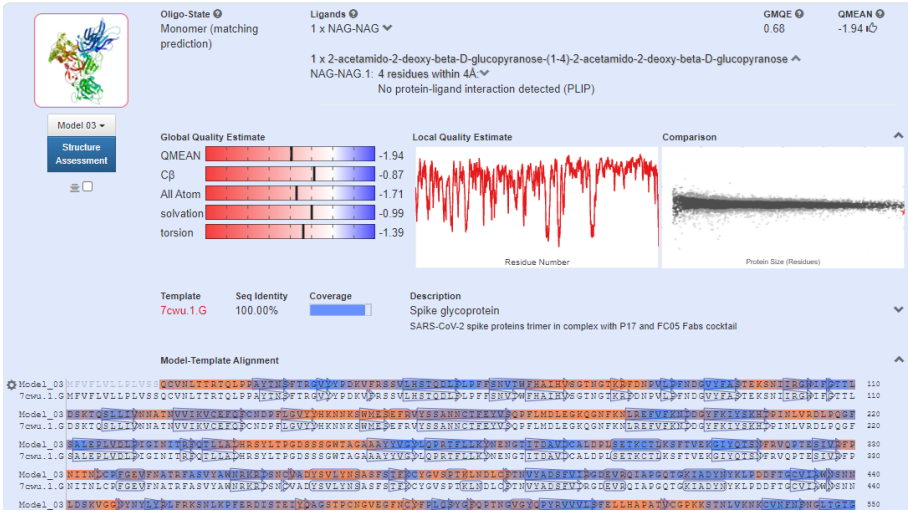

Figure 1: Demonstration of SARS nCoV2 spike domain model in Swiss-Model database (9).

Homology Modeling Tools

Rasmol (10), PyMOL (11), and UCSF Chimera (12) are the most widely used open-source programs for molecular visualization of protein structures and interactions. PDB database allows for visualization of the structure using Jmol. Pymol is a widely used molecular visualization system. It can be used to explore structures in detail and produces high-quality images. Another visualization system is UCSF Chimera. This program provides the interactive imaging and analysis of molecular structures, relevant data intensity maps, orbits and sequence alignments (13).

PyMOL visualizes high-quality three-dimensional images of small molecules such as proteins and biological macromolecules. PyMOL is one of some open-source model imaging tools that can be used structurally.

The properties of PyMol are visualizing multiple layouts of a single structure (the docking region or ligand interactions), an interface compatible with other programs, providing power graphics that can run under Windows, Mac, and Unix, and preparing broadcast quality images. RasMol is a molecular graphics program designed for the imaging of proteins, nucleic acids, and small molecules.

UCSF Chimera is designed as a highly extensible program for the visualization of files with the .pdb extension, as well as the interactive visualization and analysis of molecular structures and related data such as density maps, supermolecular structures, sequence sequences, insertion results, orbits, and conformational assemblies. Although it is used especially in the academic and pharmaceutical industries, it is also used for personal use and private companies.

Among the Chimera general structure analysis studies; atom types, hydrogen addition, charge, hydrogen bond contact, calculation of centers, measurment of volume, angle, distance and axes are identified automaticly. Ramachandran plots, suitable for calculating root-mean-square deviation (RMSD) value, protein theme map, overlapping proteins, showing hydrophobicity, displaying PDB and Mol2 formats (14).

Chimera Program

The model can be visualized in three different ways with The Chimera Program. The first of them is the “ribbons” structure. (Figure 2. A). This selection is preferred to observe the differences in general. The second selection is the “all atoms” option. (Figure 2. B).

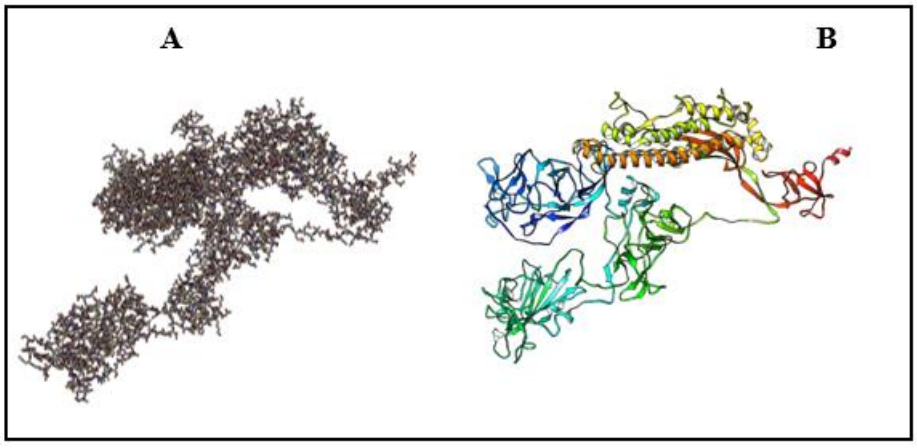

Figure 2: Model visualizing types in Chimera Program (12).

This option shows all atoms on the model. The third option is the "Hydrophobicity surface" selection (Figure 3). The hydrophobic surface option shows according to the hydrophobicity of the model. The program prefers red-white and blue colors to visualize in this option. While the hydropathy index changes from a negative value to a positive value, it turns from blue color to white and then to red color.

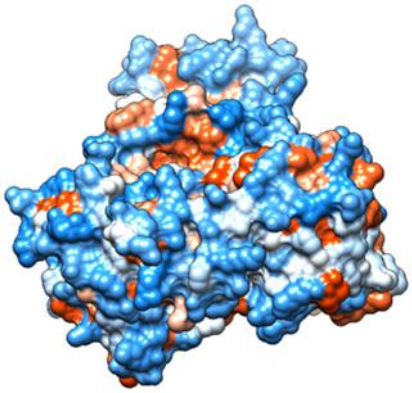

Figure 3: Hydrophobicity surface visualizing of the model in Chimera Program (12).

The root-mean-square deviation of atomic positions (RMSD) is defined as the measure of the average distance between atoms of overlapping proteins (15). The chimera program calculates RMSD values of multiple embedded models. If the RMSD value is "0", it means the models are the same. Therefore, the increase in the RMSD value means that the difference between the models increases.

Another extension tool in Chimera is the MODELLER interface. MODELLER is used for the comparative modeling of protein three-dimensional structures (16). MODELLER runs in the background and shows patterns displayed in a few minutes directly on the associated Chimera interface.

Understanding the protein mechanism is important for the protein and its structure. If we want to solve the protein's mechanism, we need to have the three-dimensional structure information of the protein (17). Methods are used to detection of protein structures such as X-ray crystallography and NMR spectroscopy (18). Determination of protein structures by experimental methods is a long and challenging process. When the experimental structure is known, evaluating the accuracy of models by homology is straightforward. Homology modeling is important to understand protein-protein interactions, protein insertion, molecular insertion, and also functional explanations of genes

identified in an organism's genome. Models obtained by homology modeling studies can be used in structure-based drug design, protein function, interaction, antigenic properties, and protein engineering studies. Relationships between changes in protein structure due to mutations and drug resistance can also be revealed by these studies.

Keywords: Homology modeling, hydrophobicity, ribbon structure

REFERENCES

1. Schneider M., Fu X., & Keating A. E. X-ray vs. NMR structures as templates for computational protein design. Proteins: Structure, *Function and Bioinformatics*. 2009; 77(1), 97–110. https://doi.org/10.1002/prot.22421
2. Muhammed M. T., & Aki-Yalcin E. Homology modeling in drug discovery: Overview, current applications, and future perspectives. Chemical Biology and Drug Design. *Blackwell Publishing.* 2019, January 1. https://doi.org/10.1111/cbdd.13388
3. Vyas V. K., Ukawala R. D., Ghate M., Chintha C., Homology Modeling a Fast Tool for Drug Discovery: Current Perspectives, *Indian Journel of Pharmaci Science*. 2012; 74(1): 1–17.
4. Arnold K., Bordoli L., Kopp J., Schwede T., The SWISS-MODEL workspace: a web-based environment for protein structure homology modelling. *Bioinformatics*. 2006; 22(2):195-201.
5. Fiser A., Do R.K., Sali A., Modeling of loops in protein structures. *Protein Science*, 2000; 9(9):1753-1773.
6. Berman H.M., Westbrook J., Feng Z., Gilliland G., Bhat T.N., Weissig H., Shindyalov I.N., Bourne P.E., The Protein Data Bank, *Nucleic Acids Research*. 2000; 28(1):235-242.
7. Dickerson R.E., Present at the Flood: How Structural Molecular Biology Came About. Sunderland, MA: *Sinauer Associates*, 2005.
8. Swiss Model-ExPASy. https://swissmodel.expasy.org/docs/help, Erişi Tarihi: 15.03.2021
9. https://swissmodel.expasy.org/interactive/16B5UU/models/ Erişim Tarihi: 15.03.2021
10. Sayle R.A., Milner-White E.J., RASMOL: biomolecular graphics for all, *Trends in Biochemical Sciences*, 1995; 20(9): p. 374.
11. Schrodinger – PyMOL. www.schrodinger.com/about, Erişi Tarihi: 15.03.2021.
12. Pettersen E.F., Goddard T.D., Huang C.C., Couch G.S., Greenblatt D.M., Meng E.C., Ferrin T.E., UCSF Chimera--a visualization system for exploratory research and analysis. *Journal of Computational Chemistry*, 2004; 25(13): p. 1605-12.
13. Morris J.H., Huang C.C., Ferrin T.E., structure Viz: linking Cytoscape and UCSF Chimera. *Bioinformatics*. 2007; 23(17): p. 2345-7.
14. UCSF Chimera. www.cgl.ucsf.edu/chimera/index.html/, Erişim Tarihi: 15.03.2021.

15. Coutsias E.A., Seok C., Dill K.A., Using quaternions to calculate RMSD .*Journal of Computational Chemistry*. 2004; 25 (15): 1849–1857.
16. Eswar N., Webb B., Marti-Renom M. A., Madhusudhan, M. S., Eramian, D., Shen, M. Y., Comparative Protein Structure Modeling using Modeller, *Current Protocols in Bioinformatics*, Chapter 5: Unit 5.6, 2006.
17. Blundell TL, Bedarkar S, Rinderknecht E, Humble RE. Proc Natl Acad Sci. 1978;75:180–184.
18. Johnson MS, Srinivasan N, Sowdhamini R, Blundell TL. Crit Rev Biochem Mol Biol 1994;29(1):1– 68.

Chapter 6

A Robust Numerical Method For The Singularly Perturbed Integro-Differential Equations

Derya ARSLAN[1]

1 Assoc. Prof. Dr. Bitlis Eren University 0000-0001-6138-0607 ayredlanu@gmail.com

1. INTRODUCTION

The study presents the numerical integration method for the approximate solution of singularly perturbed Fredholm integro-differential equations. The finite difference method is recommended on auniform mesh. Then the trapezoidal method is used for integrals. The resulting system of equations is solved with the Thomas algorithm. A sample application is made to demonstrate the reliability, speed and economy of the proposed method.

We can present the singularly perturbed Fredholm integro-differential equation with boundary conditions which we will apply the numerical integration method as follows:

$$-\varepsilon y''(x) + b(x)\, y'(x) + \gamma \int_0^1 M(x,s)\, y(s) ds = g(x), \quad x \in K = [0,1], \qquad (1)$$

$$y(0) = \mu_1, \quad y(1) = \mu_2, \qquad (2)$$

μ_1 and μ_2 are finite constants;

$\varepsilon \in (0,1)$; $b(x) \in K$, $g(x) \in K$ ve $M(x,s) \in K \times K$ are continuous functions.

Integro-differential equations also contain many mathematical formulas in the natural sciences. In particular, integro-differential equations with fixed integral bounds are called Fredholm integro-differential equations. They are found in various application areas of science and engineering. For example, economics, electrostatics, astronomy, physics, chemistry, mechanics, biology, fluid dynamics, electromagnetic theory, atomic physics, astronomy, fluid dynamics, etc. (Jerri 1999; Kythe and Puri, 2002; Polyanin and Manzhirov, 2008; Pandey, 2015). In most cases, it is difficult to reach exact solutions to such problems by most analytical methods. Thus, these problems should be solved by approximate methods. Also, there are different approaches for solving Fredholm integro-differential equations in the literature. These are Adomian decomposition method (Alao et al., 2014), reproducing kernel Hilbert space method (Arqub et al., 2008), Galerkin method (Chen et al., 2020), Legendre–Galerkin method (Fathy et al., 2014).), exponential spline method (Jalilian and Tahernezhad, 2020), hybrid Taylor and block-pulse functions method (Maleknejad and Mahmoudi, 2004), finite difference method (Amiraliyev et al., 2020; Durmaz and Amiraliyev, 2021; Erkan and Cakir, 2021).

The aim of the study is to obtain an economical and reliable approach for the approximate solution of the boundary value problems of the Fredholm integro-

differential equation on a smooth network. Our problem in the study is singular perturb (Miller et al., 1996; Ross et al., 1996; Farrell et al., 2000), that is, it has a positive, very small ε parameter in the coefficient of the highest order derivative. This parameter creates boundary multiples in the problem. In these parts, the behavior of the solution changes abruptly and rapidly. This creates non-limited derivatives in the solution of singular perturbation problems. In addition, the problems we deal with in the study include integral terms, which makes it difficult to reach analytical solutions. Many classical analytical and numerical methods that have been and are being applied so far cannot eliminate this problem. For this reason, the numerical integration method, which is one of the approximate methods that gives smooth convergence according to ε, is used in the study.

The flow of the study is as follows: In the first part, information about the problem is presented. In the second part, numerical integration method is given. In the third section, an application is made for an example problem of the proposed method. Obtained results are presented in tables and graphs.

2. NUMERICAL INTEGRATION METHOD and APPLICATION

The boundary value problems of Fredholm integro-differential equations, whose approximate solution is examined in the study, have a right boundary layer. Accordingly, the solution steps of the numerical integration method will be given as follows. It will be seen that the presented method satisfies the stability conditions.

First, the integral of the equation whose numerical solution is being investigated is taken over the interval $\left[x_{i-1}, x_i\right]$. Then the finite difference derivatives corresponding to the first two terms are obtained. The trapezoidal method is also used for integrals. For the solution of the equation system obtained from here, Thomas algorithm is applied and an approximate solution is reached. It is seen in the literature that the numerical integration method is applied to many equations (Andargie and Reddy, 2008; Ranjan and Prasad, 2018; Reddy, 1990; Soujanya and Phnaeendra, 2015; Arslan, 2020).

The problem (1)-(2) has right boundary layer for $b\left(x\right) < \alpha < 0$, where α is constant. That is, $x = 1$ is right boundary layer. The interval $\left[0,1\right]$ is divided into h segments of length N, so the grid is smooth.

The mesh points here are in the form of $x_i = x_0 + ih,\ \ i = 0,...,N-1$. In equation (1), each term is integrated from x_{i-1} to x_i.

$$\int_{x_{i-1}}^{x_i}\left[\varepsilon y''+b(x)y'\right]dx+\int_{x_{i-1}}^{x_i}\int_0^1 M(x,s)y(s)dsdx=\int_{x_{i-1}}^{x_i} g(x)dx,$$

Here the trapezoidal method is used for the second and third integrals and the following equation is obtained:

$$\begin{aligned}&\varepsilon\left[y'(x_i)-y'(x_{i-1})\right]+b_i y(x_i)-b_{i-1}y(x_{i-1})\\&+\frac{\gamma h^2}{2}\left[M(x_0,x_0)y(x_0)+2\sum_{k=1}^{i-1}M(x_0,x_k)y(x_k)+M(x_0,x_i)y(x_i)\right]=\frac{h}{2}\left[g_i+g_{i-1}\right].\end{aligned}\tag{3}$$

The finite difference derivatives $y_i'=\dfrac{y(x_{i+1})-y(x_i)}{h}$ and $\mathrm{y}_{i-1}'=\dfrac{y(x_i)-y(x_{i-1})}{h}$ for $y'(x_i)$ ve $\mathrm{y}'(x_{i-1})$ in equation (3) are written in their place and three diagonal system is found as

$$\begin{aligned}&\varepsilon\left[\frac{y(x_{i+1})-y(x_i)}{h}-\frac{y(x_i)-y(x_{i-1})}{h}\right]+b_i y_i-b_{i-1}y_{i-1}\\&+\frac{\gamma h^2}{2}\left[M(x_0,x_0)y(x_0)+2\sum_{k=1}^{i-1}M(x_0,x_k)y(x_k)+M(x_0,x_i)y(x_i)\right]=\frac{h}{2}\left[g_i+g_{i-1}\right],\end{aligned}\tag{4}$$

$$\begin{aligned}&y_{i-1}\left[-\frac{\varepsilon}{h}-b_{i-1}\right]-y_i\left[-\frac{2\varepsilon}{h}+b_i-\frac{\gamma h^2}{2}K(x_0,x_i)\right]+y_{i+1}\left[-\frac{\varepsilon}{h}\right]=\frac{h}{2}\left[g_i+g_{i-1}\right]\\&-\frac{\gamma h^2}{2}\left[M(x_0,x_0)y(x_0)+2\sum_{k=1}^{i-1}M(x_0,x_k)y(x_k)\right],\end{aligned}\tag{5}$$

$$y_0=\mu_1,\qquad \mathrm{y}_N=\mu_2.$$

The finite difference problem arises. The solution of this difference problem is reached by applying the Thomas algorithm given below in accordance with the problem.

$$A_i=-\frac{\varepsilon}{h}-b_{i-1},\quad B_i=-\frac{\varepsilon}{h},\quad C_i=-\frac{2\varepsilon}{h}+b_i-\frac{\gamma h^2}{2}K(x_0,x_i),$$

$$F_i=\frac{\gamma h^2}{2}\left[M(x_0,x_0)y(x_0)+2\sum_{k=1}^{i-1}M(x_0,x_k)y(x_k)\right]-\frac{h}{2}\left[g_i+g_{i-1}\right],$$

$$\alpha_{i+1}=\frac{B_i}{C_i-\alpha_i A_i},\quad \beta_{i+1}=\frac{F_i+\beta_i A_i}{C_i-\alpha_i A_i},\quad i=1,2,...,N-1,\quad \alpha_1=0,\quad \beta_1=\mu_1,$$

$$\mathrm{u}_i=\alpha_{i+1}y_{i+1}+\beta_{i+1},\quad i=N-1,...,2,1.$$

By following all these steps, an approximate solution is found.

$$A_i > 0,\ \mathrm{B}_i > 0 \ \text{ ve } \ \mathrm{C}_i > A_i + B_i > 0,$$
$$|\alpha_i| < 1, \quad \mathrm{i} = 0,1,...,N-1,$$

According to the conditions, the Thomas algorithm is stable and under these conditions (5) the difference problem has a solution and is unique (Amiraliyev and Amirali, 2018).

3. NUMERICAL METHOD AND ITS IMPLEMENTATION

In this section, the boundary value problem of a singularly perturbed Fredholm integro-differential equation with the following left boundary layer will be approximately solved in order to demonstrate the efficiency, reliability and time economy of the numerical integration method:

$$-\varepsilon y''(x) + \left(2 - e^{-x}\right) y'(x) + \frac{1}{2}\int_0^1 e^{x\cos(\pi s)} y(s)ds = \frac{1}{1+x}, \quad 0 < x < 1,$$
$$\mathrm{y}(0) = 1, \quad \mathrm{y}(1) = 0, \tag{6}$$

The exact solution to problem (6) is unknown. Therefore, the double mesh is used (Amiraliyev and Amirali, 2018). The maximum errors obtained are shown as:

$$e_\varepsilon^N = \max_i \left| y_i^{\varepsilon,N} - y_{2i}^{\varepsilon,2N} \right|.$$

Now, let's apply the numerical integration method to problem (6). First, in the problem (6), the integral of each term of the fredholm integro-differential equation is taken and the necessary adjustments are made.

$$\int_{x_{i-1}}^{x_i}\left[-\varepsilon y''(x)+\left(2-e^{-x}\right)y'(x)\right]dx+\frac{1}{2}\int_{x_{i-1}}^{x_i}\int_0^1 e^{x\cos(\pi s)}y(s)dsdx=\int_{x_{i-1}}^{x_i}\frac{1}{1+x}dx,\quad 0<x<1, \tag{7}$$
$$\mathrm{y}(0)=1,\quad \mathrm{y}(1)=0,$$

After taking the first integral in the equation, $y'(x_i)$ and $\mathrm{y}'(x_{i-1})$ difference approximations are used for the $y_i'=\frac{y_{i+1}-y_i}{h}$, $\mathrm{y}_{i-1}'=\frac{y_i-y_{i-1}}{h}$ derivatives. If the trapezoidal method is applied and edited in response to other integrals.

$$y_{i-1}\left[-\frac{\varepsilon}{h}-\left(2-e^{-x_{i-1}}\right)\right]-y_i\left[-\frac{2\varepsilon}{h}+\left(2-e^{-x}\right)-\frac{\gamma h^2}{2}e^{x_0\cos(\pi x_i)}\right]+y_{i+1}\left[-\frac{\varepsilon}{h}\right]=\frac{h}{2}\left[\frac{1}{1+x_i}+\frac{1}{1+x_{i-1}}\right]$$
$$-\frac{\gamma h^2}{2}\left[e^{x_0\cos(\pi x_0)}y(x_0)+2\sum_{k=1}^{i-1}e^{x_0\cos(\pi x_k)}y(x_k)\right],$$
$$y_0=1,\quad \mathrm{y}_N=0.$$

finite difference problem is obtained. Thomas algorithm is used to solve this system.

$$A_i=-\frac{\varepsilon}{h}-\left(2-e^{-x_{i-1}}\right),\quad B_i=-\frac{\varepsilon}{h},\quad C_i=-\frac{2\varepsilon}{h}+\left(2-e^{-x}\right)-\frac{\gamma h^2}{2}e^{x_0\cos(\pi x_i)},$$
$$F_i=\frac{\gamma h^2}{2}\left[e^{x_0\cos(\pi x_0)}y(x_0)+2\sum_{k=1}^{i-1}e^{x_0\cos(\pi x_k)}y(x_k)\right]-\frac{h}{2}\left[\frac{1}{1+x_i}+\frac{1}{1+x_{i-1}}\right],$$
$$\alpha_1=1,\quad \beta_1=0.$$

Approximate solution results of the boundary value problem of the singularly perturbed Fredholm integro-differential equation are obtained by using a suitable mathematical program with the flow of the Thomas algorithm given above. For N and ε values, approximate solution curves compared and error graphs are drawn. Maximum errors are found. Thus, it is revealed that the proposed method is suitable for boundary value problems of the singularly perturbed Fredholm integro-differential equation.

Table 1. Maximum errors for the value of ε and N.

N	$\varepsilon = 2^{-1}$	$\varepsilon = 2^{-2}$	$\varepsilon = 2^{-3}$	$\varepsilon = 2^{-4}$
16	0.0148915991	0.0317072199	0.0528845026	0.0829121967
32	0.0080281049	0.0178568290	0.0326101135	0.0416651252
64	0.0041765595	0.0094965848	0.0181430513	0.0221928854
128	0.0021289622	0.0049035729	0.0096175579	0.0118161927

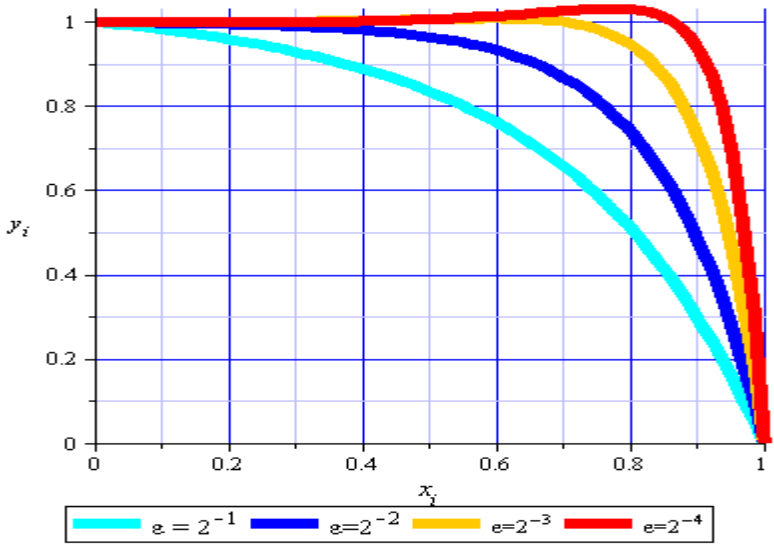

Figure 1. Approximate solutions curves for $N = 64$.

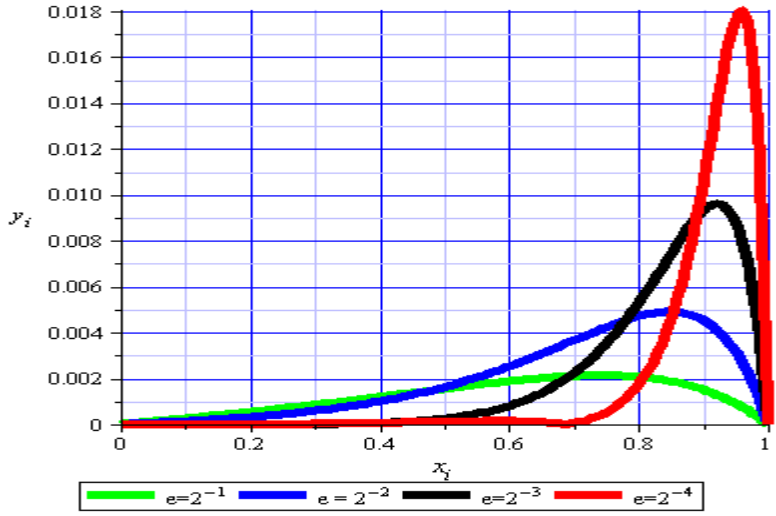

Figure 2. Maximum error curves for $N = 128$.

4. CONCLUSION

The boundary value problem of the singularly perturbed Fredholm integro-differential equation with a left boundary layer is solved numerically by the numerical integration method. Numerical solution and exact solution values are very close to each other. We see this situation as the maximum error values given in Table 1. In addition, According to Figure 1, as the value of ε decrease, the approximate solution curves lean towards the axes around $x = 1$. This means that the numerical method is reliable and convenient. As seen in Figure 2, the results of error in the boundary layer are the maximum due to the suddenly and rapidly change of the solution. In addition, the stability conditions of the Thomas algorithm are provided, that is, $|\alpha_i| < 1, \quad i = 0,1,...,N-1$. Since the maximum error values are reduced by half, the proposed method is convergent in the first order $\left(O(h)\right)$ on the uniform mesh. All these results show that the proposed method works well enough. Based on the results of this study, it can be said that it can be suitable for Volterra, Volterra-Fredholm integro-differential equations and their delayed types.

References

5. Alao, S., Akinboro, F. S., Akinpelu, F. O. and Oderinu, R. A. (2014). Numerical solution of integro-differential equation using Adomian decomposition and variational iteration methods, *IOSR J. of Math.,* 10 (4), 18-22.
6. Amiraliyev, G. M., Durmaz, M. E. and Kudu, M. (2020). Fitted second order numerical method for a singularly perturbed Fredholm integro-differential equation. *Bull. Belg. Math. Soc. Simon Stevin*, **27** (1), 71-88.
7. Amiraliyev, G. M. and Amirali, I. (2018). *Nümerik Analiz Teori ve Uygulamalarla. Seçkin Yayıncılık,* Ankara, Türkiye.
8. Andargie, A. and Reddy, Y. N. (2008). Numerical integration method for singular perturbation problems with mixed boundary conditions. *J. Appl. Math. & Informatics,* 26 (5-6), 1273-1287.
9. Arqub O. A., Al-Smadi M. and Shawagfeh N. 2013. Solving Fredholm integro-differential equations using reproducing kernel Hilbert space method. *Appl. Math. Comput.,* 219, 8938-8948.
10. Arslan, D. (2020). A numerical solution for singularly perturbed multi-point boundary value problems with the numerical ıntegration method. *BEU Journal of Science*, 9 (1), 157-167.
11. Chen, J., He, M. and Huang, Y. (2020). A fast multiscale Galerkin method for solving second order linear Fredholm integro-differential equation with Dirichlet boundary conditions. *J. Comput. Appl. Math.*, 364 (1).
12. Cimen, E. and Cakır, M. (2021). A uniform numerical method for solving singularly perturbed Fredholm integro-differential problem. *Comput. Appl. Math.*, 40.
13. Durmaz, M. E. and Amiraliyev, G. M. (2021). A robust numerical method for a singularly perturbed Fredholm integro-differential equation. *Mediterr. J. Math.*, 18.
14. Farrell, P. A., Hegarty, A. F., Miller, J. J. H., O'Riordan E. and Shishkin, G. I. (2000). *Robust Computational Techniques for Boundary Layers*. Chapman-Hall/CRC, New York.
15. Fathy, M., El-Gamel, M. and El-Azab, M.S. (2014). Legendre–Galerkin method for the linear Fredholm integro-differential equations. *Appl. Math. Comput.*, **243**, 789-800.
16. Jalilian, R. and Tahernezhad, T. (2020). Exponential spline method for approximation solution of Fredholm integro-diferential equation. *Int. J. Comput. Math.*, **97**(4), 79-80.
17. Jerri, A. (1999). *Introduction to Integral Equations with Applications.* Wiley, New York.

18. Kythe, P.K. and Puri, P. (2002). Computational Methods for Linear Integral Equations. Birkhauser, Boston.
19. Maleknejad, K. and Mahmoudi, Y. (2004). Numerical solution of linear Fredholm integral equation by using hybrid Taylor and block-pulse functions. *Appl. Math. Comput.,* **149**, 799–806.
20. Miller, J. J. H., O'Riordan, E. and Shishkin, G. I. (1996). *Fitted Numerical Methods for Singular Perturbation Problems. Error Estimates in the Maximum Norm for Linear Problems in One and Two Dimensions*. World Scientific, Singapore.
21. Pandey, P. K. (2015). Numerical solution of linear Fredholm integro-differential equations by non-standard finite difference method. *Appl. Appl. Math.,* 10(2), 1019-1026.
22. Polyanin, A. D. & Manzhirov, A. V. (2008). Handbook of Integral Equations. Chapman and Hall/CRC, Boca Raton (2008).
23. Ranjan, R. and Prasad, H. S. (2018). An Efficient Method of Numerical Integration for a Class of Singularly Perturbed Two Point Boundary Value Problems. *Wseas Transactions on Mathematics,* 17, 265-273.
24. Reddy, Y. N. (1990). A Numerical Integration Method for Solving Singular Perturbation Problems. *Applied Mathematics and Computation,* 37, 83-95.
25. Roos, H. G., Stynes, M. and Tobiska, L. (1996). *Numerical Methods for Singularly Perturbed Differential Equations, Convection-Diffusion and Flow Problems*. Springer Verlag, Berlin.
26. Soujanya, G. and Phnaeendra, K. (2015). Numerical intergration method for singular-singularly perturbed two- point boundary value problems. *Procedia Engineering,* 127, 545-552.

Chapter 7

Pseudo Quadratıc Modules

Elis SOYLU YILMAZ[1]

1 Dr. Araştırma Görevlisi, Matematik ve Bilgisayar Bilimleri Bölümü, Fen Fakültesi, Eskişehir Osmangazi Üniversitesi

Introduction

Simplicial algebras is a concept between K-theory, algebraic geometry, homotopy theory, and homological theory. There is a wealth of literature on their homotopy theory, and they have contributed significantly to improvements in each field over a sizable amount of time.

In (Whitehead, JHC. 1949), Whitehead defined crossed modules with a view to capture the relationship between first and second fundamental group of a space. Furthermore, Whitehead introduced homotopy systems to take into account the influence of first fundamental group. These systems are now known as free crossed complexes (Brown, R. & Higgins, PJ. 1981) or completely free crossed chain complexes (Baues, HJ. 1991, Baues, HJ. 1995).

The concept of a quadratic module was defined by Baues (Baues, HJ. 1991) as a model of connected 3-types. Crossed squares, simplicial groups were highly connected to the quadratic modules. Simplicial methods used in various categorical structures in (Arvasi, Z. & Porter, T. 1996, Arvasi, Z. & Ulualan, E. 2007, Mutlu, A. & Porter, T. 1998). Quadratic modules studied in (Yılmaz, K., & Yılmaz, E. S. 2019, Yılmaz, K., & Yılmaz, Ulualan, E. 2011, E. S. 2019, Soylu Yılmaz, E., & Yılmaz, K. 2022).

In the category of groups, nonabelian derived functors with values and homotopy group of pseudosimplicial groups were introduced by Inasaridze (c.f. Inasaridze, H. N. 1974, Inasaridze, H. N. 1975). In recent years, Akça and Pak studied the crossed modules and pseudosimplicial groups (Akça, İ.İ. & Pak, S. 2010). Pseudosimplical algebra was introduced by Pak in PhD thesis (Pak, S. 2006).

In this study, we introduce the pseudo quadratic module. We construct a pseudo quadratic module from a given pseudosimplicial algebra and vice versa.

2. Pseudosimplicial Algebras

A pseudosimplicial algebra E consists of $\{E_n\}$ algebras together with boundary algebra homomorphisms $\partial_i^n: E_n \to E_{n-1}, 0 \leq i \leq n, (n \neq 0)$ and degeneracies $s_i^n: E_n \to E_{n+1}, 0 \leq i \leq n,$ which satisfies the properties below:

$$\partial_i^{n-1}\partial_j^n = \partial_{j-1}^{n-1}\partial_i^n \qquad ,i < j$$
$$\partial_i^{n+1}s_j^n = s_{j-1}^{n-1}\partial_i^n \qquad ,i < j$$
$$\partial_j^{n+1}s_j^n = \partial_{j+1}^{n+1}s_j^n = 0$$

$$\partial_i^{n+1} s_j^n = s_j^{n-1} \partial_{i-1}^n \qquad , i > j+1$$

The pseudosimplicial algebra E is diagrammatized with

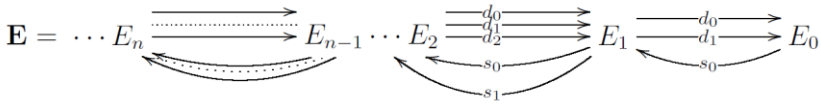

In order to get a simplicial algebra, we need to add $s_i^{n+1} s_j^n = s_{j+1}^{n+1} s_i^n$ condition, for $i \leq j$.

For any pseudosimplicial algebra E, let $NE_n = E_n \cap Ker\partial_0^n \cap \ldots \cap Ker\partial_{n-1}^n$ for $n \geq 0$ and $d_n = \partial_n^n$. Then $Im\ d_n$ is an ideal of E_{n-1}, and

$$Im\ d_{n+1} \subseteq Ker\ d_n$$

for $n > 0$. This determines the Moore complex $\boldsymbol{NE} = \{NE_n, d_n\}$. $\pi_n(E)$ is defined with nth order homotopy module of the pseudosimplicial algebra

$$\pi_n(E) \cong H_n(NE, \partial) = \frac{\bigcap_{i=0}^n Ker d_i^n}{d_{n+1}^{n+1}(NE_{n+1})} = \frac{NE_{n+1} \cap Ker d_n^n}{d_{n+1}^{n+1}(NE_{n+1})}$$

For $n > k$, if pseudosimplicial algebra of E_n is $\{0\}$, then this algebra is the k-truncated pseudosimplicial algebra. k- truncated pseudosimplicial algebra is denoted by $tr_k\ E$ and the truncation functor is:

$$tr_k : PseudosimpAlg \rightarrow Tr_k Pseudosimpalg$$

k-coskeleton is the right adjoint functor of the truncation functor

$$Cos_k : Tr_k PseudosimpAlg \rightarrow PseudosimpAlg$$

and k-skeleton functor is:

$$sk_k : Tr_k PseudosimpAlg \rightarrow PseudosimpAlg$$

Lemma 2.1: Let E be a pseudosimplicial algebra. The Moore complex of its k -coskeleton $cosk^k(tr^k E)$ is identical to the Moore complex of E in dimensions $\leq k$ and is of length $k+1$.

Definition 2.2: Let $[n] = \{0 < 1 < \cdots < n\}$ be the ordered set. $\delta_i^n : [n-1] \to [n]$ is the injective monotone transformation with

$$\delta_i^n(a) = \begin{cases} a & , a < i \\ a+1 & , a \geq i \end{cases}$$

For $0 \leq i \leq n$. On the other way, $\sigma_i^n : [n+1] \to [n]$ is the surjective transformation and denoted by

$$\sigma_i^n = \begin{cases} a & , a \leq i \\ a-1 & , a > i \end{cases}$$

3. Pseudo Quadratic Module

Definition 3.1: An algebra homomorphism of $\partial : E \to N$ with an action of N on E denoted $e \cdot n$ for $n \in N$ and $e \in E$ satisfies $\partial(e \cdot n) = \partial(e)n$ then $\partial : E \to N$ is a pre-crossed module. For $e, e' \in E$ if $\partial : E \to N$ satisfies the additional condition $e \cdot \partial(e') = ee'$, then $\partial : E \to N$ is a **crossed module**.

Let $\partial : E \to N$ be a pre-crossed module, $P_1(\partial) = E$ and $P_2(\partial)$ be the Peiffer ideals of E with generators

$$< e_1, e_2 >= e_1 e_2 - e_1 \cdot \partial e_2$$

for $e_1, e_2 \in E$ is called the Peiffer element in E. The pre-crossed module $\partial : E \to N$ with the extra 'nilpotency' condition is called a **nil(2)-module**. This is the condition $P_3(\partial) = 0$ in which $P_3(\partial)$ is the ideal of E with Peiffer element generators $< e_1, e_2, e_3 >$. The pre-crossed module $\partial : E \to N$ is associated with the homomorphism

$$\partial^{cr} : C^{cr} = C/P_2(\partial) \to N$$

which is a crossed module.

Theorem 3.2: A Nil(2)- module can be obtained from a given pseudosimplicial algebra.

Proof: Let E be a pseudosimplicial algebra with Moore complex of length 1. Define: $M = NE_0 = E_0, L = NE_1$ and $\partial = d_1|_L$, and the action of M on L as

$$m \cdot l = s_0(m) \cdot l$$

for $l \in L$ and $m \in M$. Since

$$\begin{aligned} \partial(m \cdot l) &= d_1(m \cdot l) \\ &= d_1\big(s_0(m)\big) \cdot l \\ &= m \cdot d_1(l) \end{aligned}$$

$\partial: M \to N$ is a pre-crossed module. Let P be the ideal of NE_1 with generators

$\ll a, b >, c >, < a, < b, c \gg$

for $a, b, c \in NE_1$. Then we can define quotient

$$q_1: NE_1 \to \frac{NE_1}{P} = \bar{L}$$

Since $\partial(P_3) = 0$,

$$\begin{aligned} &\bar{\partial}: \bar{L} \to M \\ &P + P_1 \to \partial(l) \end{aligned}$$

is well defined. Thus $\bar{\partial}: \bar{L} \to M$ becomes a nil(2)-module.

That is we get a functor

$$PSimpAlg_{\leq 1} \to Nil(2).$$

Theorem 3.3: A pseudosimplicial algebra can be obtained from a given Nil(2)- module.

Proof: Let $\partial: L \to M$ be a nil(2)-module. With the action of M on L, we can define $M \ltimes L$. Therefore

$$s_0: M \to M \ltimes L \text{ ,} m \mapsto (m, 1)$$

$$d_1: M \ltimes L \to M, (m, l) \mapsto \partial(l)m$$

$$d_0: M \ltimes L \to M, (m, l) \mapsto l$$

are homomorphisms. For $E_0 = M, E_1 = M \ltimes L, \{E_0, E_1\}$ is the pseudosimplicial algebra in which its coskeleton denoted by E^1. Using the action of M on $L, M \ltimes L$ on L via d_1. We form the semi-direct product $L \ltimes (L \ltimes M)$ then there are homomorphisms:

$$d_0 : L \ltimes (L \ltimes M) \to L \ltimes M, \big(l, (l', m)\big) \mapsto (l', m)$$

$$d_1 : L \ltimes (L \ltimes M) \to L \ltimes M, \big(l, (l', m)\big) \mapsto (ll', m)$$

$$d_0 : L \ltimes (L \ltimes M) \to L \ltimes M \ , \big(l, (l', m)\big) \mapsto \ (l, \partial(l')m)$$

$$s_0 : L \ltimes M \to L \ltimes (L \ltimes M), (l, m) \mapsto \big(1, (l, m)\big)$$

$$s_1 : L \ltimes M \to L \ltimes (L \ltimes M), (l, m) \mapsto \big(l, (1, m)\big)$$

For $E_2 = L \ltimes (L \ltimes M)$ we get a pseudosimplicial algebra $\{E_0, E_1, E_2\}$ and we denote the coskeleton with E^2. There is a unique simplicial map $E^2 \to E^1$ that is the identity in dimensions 0 and 1. We denote the image of E_2 in E_1 by $\overline{E_2}$. Since the length of Moore complex of E_2 is 2; it follows from Lemma 2.1 that the Moore complex of the pseudosimplicial algebra $\overline{E_2}$ is of length 1.

■

Let K, L, M be k −algebras and $\partial : L \to M$ be a pre-crossed module. A pseudo quadratic module is a diagram

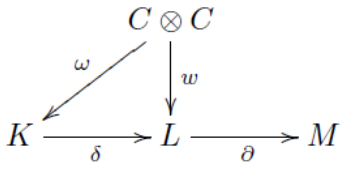

of k-algebra homomorphisms satisfying the axioms PQ1-PQ5 where the Peiffer product

$$\omega : C \otimes C \to L$$

$$[a] \times [b] \mapsto ab - a \cdot \partial(b)$$

of the pre-crossed module $\partial: L \to M$ is called quadratic map. ($C = L^{cr}/(L^{cr})^2$).

PQ1) $\partial: L \to M$ is a nil(2)-module and $\partial\delta = 1$.

PQ2) $\delta(m \cdot k) = m \cdot \delta(k)$

PQ3) $\delta\omega(l \otimes l') = w([l] \otimes [l']) = ll' - l \cdot \partial(l')$

PQ4) $\omega\big(\delta(k), \delta(k')\big) = kk'$

PQ5) $\omega([\delta(k)] \otimes [l] + [l] \otimes [\delta(k)]) = k \cdot \partial(l)$

for $m \in M, l, l' \in L$ and $k, k' \in K$.

Theorem 3.4: A pseudo quadratic module can be obtained from a given pseudosimplicial algebra.

Proof: Let E be pseudosimplicial algebra with Moore complex of length 2. To obtain a pseudo quadratic module we take $M = E_0, L = Ker(d_0: E_1 \to E_0)$ and $K = Ker(d_0: E_2 \to E_1) \cap Ker(d_1: E_2 \to E_1)$. The action of M on L and K defined as

$n \cdot m = s_0(n) \cdot n, n \cdot l = s_0 s_0(n) \cdot l$

respectively. Then we get diagram

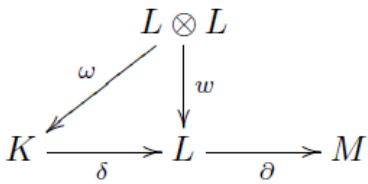

where $\delta = d_2|_L, \partial = d_1|_M$ and $\omega(l_1 \otimes l_2) = s_1(l_1)(s_1(l_2) - s_0(l_2))$ for $l_1, l_2 \in L$. To add nilpotency conditions we obtain quotient algebras $\overline{K} = K/P'_3$ and $\overline{L} = L/P_3$ where P_3 is the ideal defined in section 2 and P'_3 be the ideal of K with generators

$\omega(< l_1, l_2 > \otimes l_3), \omega(l_1 \otimes < l_2, l_3 >)$

for $l_1, l_2, l_3 \in L$.

Since $P_3(\partial) = 1$

$$\bar{\partial}: \bar{L} \to \bar{M}$$

$$l + P_3 \mapsto \partial(x)$$

is a well defined homomorphism and the diagram

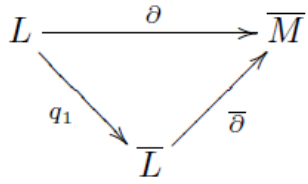

commutes. For $l_1, l_2, l_3 \in L$

$\delta\omega(l_1 \otimes < l_2, l_3 >) = Id_{l_1 \otimes <l_2, l_3>}$

$\delta\omega(< l_1, l_2 > \otimes l_3) = Id_{<l_1, l_2> \otimes l_3}$

we get $\delta\omega(P_3{}') \subset P_3$. That is the homomorphism

$$\bar{\delta}: \bar{L} \to \bar{M}$$

$$[l] + P_3' \mapsto [\delta(l)] + P_3$$

is well defined. Then we get a diagram

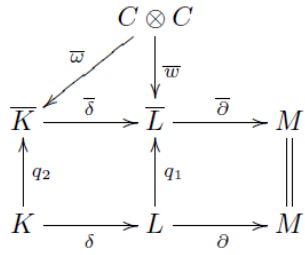

where q_1, q_2 are quotient maps and $C = L^{cr}/(L^{cr})^2$.

We claim that

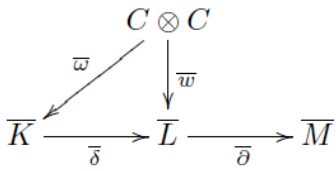

is a pseudo quadratic module with the quadratic map

$\bar{\omega}([q_1(l_1)] \otimes [q_1(l_2)]) = q_2(s_1 l_1(s_1 l_2 - s_0 l_2))$

PQ1) $\bar{\partial}\bar{\delta}(k) = d_1 d_2(k)$

$= d_1 d_1(k)$

$= d_1(k)$

$= 1(\because k \in Ker(d_1 : G_2 \to G_1))$

PQ2) $\bar{\delta}(m \cdot k) = \delta(s_0 s_0 m \cdot k)$

$= d_2(s_0 s_0 m \cdot k)$

$= d_2 s_0 s_0 m d_2(k)$

$= s_0 d_1 s_0 m d_2(k)$

$= s_0 m d_2(k)$

$= s_0 m \bar{\delta}(k)$

$= m \cdot \bar{\delta}(k)$

PQ3) $\bar{\delta}\bar{\omega}([q_1(l_1)] \otimes [q_1(l_2)]) = \bar{\delta} q_2(s_1 l_1(s_1 l_2 - s_0 l_2))$

$= q_1(d_2(s_1 l_1 - (s_1 l_2 - s_0 l_2)))$

$= q_1(l_1 l_2 - l_1 s_0 d_1 l_2)$

$$= q_1(l_1)q_1(l_2) - q_1(l_1) \cdot \bar{\partial}(q_1(l_2))$$

PQ4) $\bar{\omega}\left(\bar{\delta}q_2(k_1) \otimes \bar{\delta}q_2(k_2)\right) = q_1(s_1k_1(s_1k_2 - s_0k_2))$

$$= q_2(k_1k_2 - k_1k_2) + (s_1k_2 - s_0k_2)$$

$$= q_2(k_1k_2) - q_2(k_1k_2) + (s_1k_2 - s_0k_2)$$

$$= q_2(k_1)q_2(k_2) - q_2(k_1k_2) + (s_1k_2 - s_0k_2)$$

$$= q_2(k_1)q_2(k_2) - d_3s_2(k_1k_2) + (s_1k_2 - s_0k_2)$$

$$= q_2(k_1)q_2(k_2) - d_3s_2(k_1k_2) + d_3s_2k_1(d_3s_1k_2 - d_3s_0k_2)$$

$$= q_2(k_1)q_2(k_2) + d_0(-s_2(k_1k_2) + s_1k_2(s_1k_2 - s_0k_2))$$

$= q_2(k_1)q_2(k_2)$

PQ5) $\bar{\omega}\left(\left[\bar{\delta}(k)\right] \otimes [q_1(l)]\right) = \omega([q_1\delta(k)] \otimes [q_1(l)])$

$= q_2(s_1d_2k(s_1l - s_0l))$

Since $(s_0l - s_1l)s_1d_2k - (s_0l - s_1l)k \in L$ we get

$q_2\left(s_1d_2k(s_1l - s_0l)\right) = s_0d_1l(q_2k) - s_1l(q_2k)$

$= q_2k \cdot \bar{\partial}q_1(l) - l \cdot q_2(k)$

and

$\bar{\omega}\left([q_1(l)] \otimes \left[\bar{\delta}(k)\right]\right) = \omega([q_1(l)] \otimes [q_1\delta(k)])$

$= q_2(s_1l(s_1d_2k - s_0d_2l))$

Since $s_1l(s_0d_2k - s_1d_2k) + s_1lk \in L$ we get

$q_2(s_1l(s_1d_2k - s_0d_2l)) = l \cdot q_2(k)$

That is

$$\bar{\omega}\left(\left[\bar{\delta}(k)\right] \otimes [q_1(l)] + [q_1(l)] \otimes \left[\bar{\delta}(k)\right]\right) = q_2(k) \cdot \bar{\partial} q_1(l)$$

That is we get a functor

$$\nabla : PSimpAlg_{\leq 2} \to PQuad$$

Theorem 3.5: A pseudosimplicial algebra can be obtained from a given pseudo quadratic module.

Proof: We will define a pseudosimplicial algebra $\{E_0, E_1, E_2\}$ of length 2 from a pseudo quadratic module

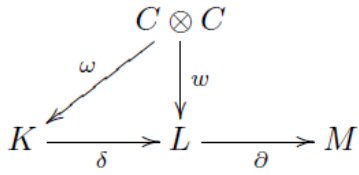

of commutative algebras. Let $E_0 = M$ and $E_1 = M \ltimes L$ then

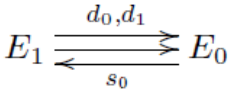

is a 1-truncated pseudosimplicial algebra with face and degeneres maps

$$d_0(l, m) = m, d_1(l, m) = \partial(l) + m, s_0(m) = (1, m)$$

The action of L on K

$$l \cdot k = k \cdot \partial(l) + \omega([\delta(k)] \otimes [l])$$

is well defined since the quadratic map is bilinear. Then we can form $K \ltimes L$. Furthermore the action of E_1 on $K \ltimes L$ given as

$$(l, m) \cdot (k, l') = (k \cdot \partial(l) + \omega([\delta(k)] \otimes [l]) + m \cdot k, ll' + m \cdot l)$$

Then we define $E_2 = (K \ltimes L) \ltimes (M \ltimes L)$.

Next we will show that

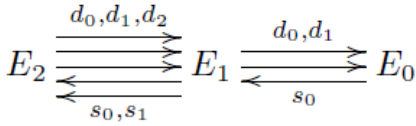

satisfies pseudosimplicial algebra identities where

$d_0(k, l_1, l_2, m) = (l_2, m), d_1(k, l_1, l_2, m) = (l_1 + l_2, m)$

$d_2(k, l_1, l_2, m) = (l_1, \partial l_2 + m), s_0(l, m) = (1,1, l, m)$

and

$s_1(l, m) = (1, l, 1, m)$

1. For $i < j$

$$\begin{aligned} d_0 d_1(k, l_1, l_2, m) &= d_0(l_1 + l_2, m) \\ &= m \\ &= d_0(m_2, n) \\ &= d_0 d_0(k, l_1, l_2, m) \end{aligned}$$

$$\begin{aligned} d_1 d_2(k, l_1, l_2, n) &= d_1(l_1, \partial l_2 + n) \\ &= \partial l_1 + \partial l_2 + n \\ &= d_1(l_1 + l_2, n) \\ &= d_1 d_1(k, l_1, l_2, n) \end{aligned}$$

$$\begin{aligned} d_0 d_2(k, l_1, l_2, m) &= d_0(l_1, \partial l_2 + n) \\ &= \partial l_2 + n \\ &= d_1(l_2, m) \\ &= d_1 d_0(k, l_1, l_2, m) \end{aligned}$$

we get

$$d_i^{n-1} d_j^n = d_{j-1}^{n-1} d_i^n$$

2. For $i < j$

$$\begin{aligned} d_0 s_1(l_2, m) &= d_0(1, l_2, 1, m) \\ &= (0, m) \end{aligned}$$

$$= s_0(m)$$
$$= s_0 d_0(l_2, m)$$

we get

$$d_0^2 s_1^1 = s_0^0 d_0^1$$

3. For $i = j$ or $i = j + 1$

$$d_1 s_1(l, m) = d_1(1, l_1, 1, m)$$

$$= (l \cdot 1, m)$$

$$= (l, m)$$

$$= Id_{(l,m)}$$

$$d_0 s_0(l, m) = d_0(1,1, l, m)$$

$$= (l, m)$$

$$= Id_{(l,m)}$$

$$d_1 s_0(l, m) = d_1(1,1, l, m)$$

$$= (1 \cdot l, n)$$

$$= (l, m)$$

$$= Id_{(l,m)}$$

we get

$$d_i^{n+1} s_j^n = Id$$

4. For $i > j + 1$

$$d_2 s_0(l, m) = d_2(1,1, l, m)$$

$$= (1, \partial(l) + n)$$

$$= s_0(\partial_1(l) + n)$$

$$= s_0\big(d_1(l,m)\big)$$

we get

$$d_i^{n+1} s_j^n = s_j^{n-1} d_{i-1}^m$$

As a result $\{E_0, E_1, E_2\}$ is a 2-truncated pseudosimplicial algebra. There exists a functor

$$\Delta: PQuad \to PSimpAlg_{\leq 2}$$

4. Conclusion

In this study, we give detailed categorical equivalences between pseudosimplicial algebras and pseudo quadratic modules. Some higher dimensional relations could be studied in the future works. Furthermore, the structures that equivalent to the quadratic modules can be demonstrated and can be given categorically.

5. References

[1] Whitehead, J.H.C. 1949 Combinatorial homotopy I and II, Bulletin of the American Mathematical Society, 55, 231-245 and 453-496.

[2] Brown, R. & Higgins, P.J. 1981 Colimit-theorems for relative homotopy groups, Journal of Pure Applied Algebra, 22, 1-41.

[3] Baues, H. J. 1991 Combinatorial homotopy and 4-dimensional complexes, Walter de Gruyter.

[4] Arvasi, Z. & Ulualan, E. 2007 Quadratic and 2-Crossed Modules of Algebras, Algebra Colloqium, 14(4), 669-686.

[5] Mutlu, A. & Porter, T. 1998 Freeness conditions of 2-crossed modules and complexes, Theory and Applications of Categories, Vol. 4, No. 8, 174-194.

[6] Yılmaz, K., & Yılmaz, E. S. 2019 Cebirler Üzerinde Kuadratik Modüller In Mathematics and Natural Sciences-2019/2, 135.

[7] Ulualan, E. 2011 Quadratic Modules for Lie Algebras Hacettepe Journal of Mathematics and Statistics, 40(3), 409-419.

[8] Yılmaz, K., & Yılmaz, E. S. 2019 Gruplar Üzerinde Kuadratik Modüller In Mathematics and Natural Sciences-2019/2, 105.

[9] Soylu Yılmaz, E., & Yılmaz, K. 2022 On relations among quadratic modules Mathematical Methods in the Applied Sciences, 1-14.

[10] Arvasi, Z. & Porter, T. 1996 Simplicial and crossed resolutions of commutative algebras, Journal of Algebra, 181, 426-428.

[11] Baues, H. J. 1995 Homotopy types, Handbook of Algebraic Topology, Edited by I. M. James, Elsevier, 1-72.

[12] Inasaridze, H. N. 1974 Homotopy of pseudosimplicial groups and nonabelian derived functors, Sakharth, SSR, Mecn. Akad. Moambe, 76, 533-536.

[13] Inasaridze, H. N. 1975 Homotopy of pseudosimplicial groupsand nonabelian derived functors and algebraic K-theory, Math. Sbornik, TOM, 98, (140), No: 3, 303-323.

[14] Akça, İ.İ. & Pak, S. 2010 Pseudo simplicial groups and crossed modules, Turkish Journal of Mathematics, 34, 474- 487.

Chapter 8

Age and Body Size of the Anatolian Banded Newt *Ommatotriton Nesterovi* (Litvinchuk, Zuiderwijk, Borkin & Rosanov, 2005)

Ufuk BÜLBÜL[1]
Hatice ÖZKAN[2]
Engin ZAMAN[3]

1 Prof. Dr., Karadeniz Technical University, ufukb@ktu.edu.tr

2 Dr., Karadeniz Technical University, haticeozkan@ktu.edu.tr

3 Elvanpazarcık District, Zonguldak, enginzaman67@hotmail.com

INTRODUCTION

The Anatolian Banded Newt, *Ommatotriton nesterovi* (Litvinchuk, Zuiderwijk, Borkin & Rosanov 2005), is an endemic newt species of Turkey. It has a limited distribution along the nortwestern parts of Anatolia (Litvinchuk et al. 2005; Bülbül and Kutrup 2013; van Riemsdijk et al. 2017; Üzüm et al. 2019; Baran et al. 2021; Bülbül et al. 2021).

After Litvinchuk et al. (2005) described new subspecies (*Ommatotriton ophryticus nesterovi*) of the Caucasian banded newt, *Ommatotriton ophryticus* (Berthold 1846) from northwestern Turkey, the taxon was raised to full species (*Ommatotriton nesterovi*) by Bülbül and Kutrup (2013) and it was recognized as full species "for convenience" by van Riemsdijk et al. (2017).

Studies related to the age of *Ommatotriton nesterovi* is limited to the studies of Başkale et al. (2013) who investigated age determination and population size of pedomorphic and metamorphic forms of the species (when it was formerly known as a subspecies of *Ommatotrion ophryticus*) in two distinct pools from Sakarya province of Turkey and Gümüş-Özcan and Üzüm (2015) who compared age structure and Snout-Vent Length SVL of *Ommatotriton ophryticus* (when it was formerly known as a subspecies of *O. ophryticus*) at different altitudes (located in Bilecik and Kastamonu provinces of Turkey).

Skeletochronology method estimates the ages of amphibans and lizards by observing the cyclicial growth forms in the bones of these animals. The ages of these animals are obtained by counting the lines of the arrested growth (LAGs) [Castanet and Smirina (1990) and Castanet (1994)].

Purpose of our study is: to assess some life history traits (e.g. mean and maximum age, sexual size dimorphism and SVL) in a population of *O. nesterovi* from western Black Sea Region of Turkish.

A total of 40 (22 ♂♂ and 18 ♀♀) *Ommatotriton nesterovi* museum specimens from Aksu population located in Devrek District, Zonguldak Province, Turkey (Fig. 1) were used. The population (41°04'423'' N, 31°46'106'' E) is found in a high elevated area (546 m a.s.l). The population has a habitat including an artificial irrigation pond surrounded by various fruit trees.

The active period of *O. nesterovi* in Aksu population lasts from April to October. The mean precipitation and annual temperature data, which were taken from the 9th Meteorology Regional Directorate of Ankara, over the last 30 years at the Aksu site were 103.21 mm and 14°C, respectively. Throughout the active season of the newts, the mean precipitation and temperature were 79.46 mm and 18.6 °C, respectively.

Sex determination was perfomed by examination of presence of the dorsal and caudal crest of male specimens. Body size of the newts was measured with a digital caliper.

For each newt, the 2nd phalange belonged to longest finger of the hind limb was used for subsequent histologic analyses. The experimental application of skeletochronology method is related to accounting of LAGs in the cross sections of the middle part of the second phalanx from the longest toe (Bülbül et al. 2018). We followed an experimental procedure used in the study of Eroğlu et al. (2018).

The ages of each lizard were found by skeletochronology method (Castanet and Smirina 1990; Smirina 1994). Numbers of LAGs were independently calculated by two observers and they compared their results. We considered the double line as one LAG in our study as in the studies of Guarino and Erişmiş (2008), Aragón and Fitze (2014), and Bülbül et al. (2018). The space between two adjacent LAGs is a well sign of growth of the newts in a dedicated year (Kleinenberg and Smirina 1969). The point, where an obvious decrease in spacing between two subsequent LAGs observed, was taken to point the age at sexual maturity was achieved (Ryser 1998; Bülbül et al. 2016).

SVLs and age classes were normally distributed (one-sample Kolmogorov-Smirnov test, $P > 0.05$). Thus, nonparametric independent sample Mann Whitney U-test ($P < 0.05$) was conducted to compare means and Spearman's correlation coeffiecient ($P < 0.01$) was used to resolve correlations. The processed applications were done with IBM SPSS 22.0 for Windows.

RESULT

In all phalangeal cross sections of the (n = 40), a hematoxylinophilic outer line which correspond to a winter line of arrested growth and the growth zone were present (Fig. 2). Within the all studied samples, the resorption zone did not reach the first LAG. In the present study, double line and endosteal resorption were observed in 3 (7.5%) and 2 (5%) individuals, respectively. Age at maturity was found to be 2-3 years in both sexes. It was 2 years (47.1%) and 3 years (47.1%) in females and 2 years (50.0%) and 3 years (43.8%) in males.

The means of SVL and age were 51.43 ± 0.70 mm and 7.15 ± 0.20 for all individuals of *O. nesterovi* (49.90 ± 1.30 mm and 6.89 ± 0.20 in females and 52.67± 0.70 mm and 7.41 ± 0.20 in males), respectively (Table 1).

The estimated ages from the cross sections ranged from 5-10 years for females and 6-11 years for males. No significant difference was found in the mean age (Mann Whitney U-test; U = 150, P = 0.177) between the sexes.

In addition, no significant difference was found between the sexes in the mean SVL (Mann Whitney U-test; U = 147, P = 0.166). A strong correlation was found

between SVL and age for females (Spearman's correlation coefficient (r = 0.886, P = P < 0.01) and males (r = 0.912, P = P < 0.01) individuals of the species (Fig. 3 and Fig. 4).

In the present study, the maximum lifespan of *Ommatotriton nesterovi* is 11 years in males while it is 10 years in females in the Zonguldak (Aksu) population. Approximately our findings, Gümüş-Özcan and Üzüm (2015) reported that longevity of *O. nesterovi* was 10 years in males and females in the Bilecik (Bahçesultan) population and 9 years in both sexes in the Kastamonu (Tosya) population. However, Başkale et al. (2013) found lower longevity (8 years in males and 6 years for metamorphs and 4 years in males and 5 years in females for pedomorphs) in the Sakarya population of *O. nesterovi*. The longevity depends on environmental and climatic factors such as altitude and latitude (Berven 1982; Miaud et al. 1999). Because the mean precipitation and annual temperature in habitats of the Anatolian banded newts in Aksu, Bahçesultan, Tosya, and Sakarya are nearly similar, the similar longevity results of our study and Gümüş-Özcan and Üzüm (2015) can be considered as normal. The lower maximum lifespan in the Sakarya population studied by Başkale et al. (2013) may be attributed to the low sample size (13 males and 10 females of metamorphs and 9 males and 12 females of pedomorphs) in this study or unknown effects, such as predator or anthropogenic press, food availability, etc.

The maximum life span for Caucasian banded newt, *Ommatotriton ophryticus* was reported to be 8–21 years in varied distribution areas of the species (Kuzmin 1999; Tarkhnishvili and Gokhelashvili 1999). In Turkey, Kutrup et al. (2005) studied the age of *O. ophryticus* in lowelevation (Gürbulak, 300 m a.s.l.) and highelevation (Hıdırnebi, 1300 m a.s.l.) populations. They reported the oldest *O. ophryticus* individual as 10 years old in the lowelevation site and 16 years old in the highelevation site. In addition, Gümüş-Özcan and Üzüm (2015) reported longevity of *O. ophryticus* as 12 years in a Turkish population (Tokat-Erbaa, 1239 m a.s.l.).

In a lowland Turkish population (Mersin-Tarsus, 25 m a.s.l.) of The banded newt, *Ommatotriton vittatus* (Gray in Jenys 1845), the maximum life span was found as 8 years by Altunışık (2018).

Amphibians at high altitudes or high latitudes grow more slowly and take longer to reach sexual maturity than do populations of the same species in warmer climate (Wells 2007). In the present study, both sexes of the *O. nesterovi* in Aksu population (located in 546 m a.s.l) attained sexual maturity in 2-3 years of age. In the higher altitudes (1015 m a.s.l. for Bahçesultan and 1202 m a.s.l. for Tosya population) Gümüş-Özcan and Üzüm (2015) reported higher values of maturation age (6 years in both sexes of Bahçesultan and 4 years in males and 5

years in females of Tosya). Similar to these results, Kutrup et al. (2005) suggested that sexual maturity age in *Ommatotriton ophryticus* was four years in a highland population and two–three years in a lowland population.

Snouth-vent length was not different significantly between the sexes of *O. nesterovi* in Aksu population. However, males of Bahçesultan and Tosya populations of *O. nesterovi* were larger than females in the study of Gümüş-Özcan and Üzüm (2015) and the differences were statistically significant. Similarly, Başkale et al. (2013) reported that males were significantly older than females in Sakarya population of the species.

In the Aksu population of *O. nesterovi*, a strong positive correlation between age and SVL was found for both females and males. Similarly, Başkale et al. (2013) reported a correlation between SVL and age in males and females of Anatolian banded newt. On the other hand Gümüş-Özcan and Üzüm (2015) reported this correlation for only males of *O. nesterovi*.

Double line and endosteal resorption rates might be affected some ecological factors (e.g. dry conditions, high temperatures, variation in availability of food sources and other infrequent environmental changes) which are unpredictable (Smirina 1972; Jakob et al. 2002; Guarino and Erişmiş 2008). Because the newts in the Aksu population were not exposed to unusually arid conditions (according to data of 9th Meteorology Regional Directorate, Ankara), drought was not an important factor causing the double lines.

Occurrence and rate of endosteal resorption in amphibians may vary in populations of the same species inhabiting regions having different weather conditions or daily and annual activity patterns (Esteban et al. 1996). The percentage of endosteal resorption was very low (5%) in the Aksu population of *O. nesterovi*. However, high percentages (90% in Bahçesultan and 98.33% in the Tosya population) were reported for *O. nesterovi* by Gümüş-Özcan and Üzüm (2015). These results cleary show that the newts in Aksu, Bahçesultan and Tosya populations live in different daily and annual activity patterns.

Results of our study exhibit the highest age of (11 years) *Ommatotriton nesterovi* ever found. It is possible to reach higher age values with the researches conducted along different populations of the species located in the other environments.

ACKNOWLEDGMENT

We wish to thank Dilay Çalışkan and Fatma Şeyma Özkan for their assistance in the laboratory studies.

REFERENCES

1. Altunışık A. 2018. The first demographic data and body size of the southern banded newt, *Ommatotriton vittatus* (Caudata: Salamandridae). Acta Herpetologica, 13(1): 13-19.
2. Aragón P. and Fitze P.S. (2014). Geographical and Temporal Body Size Variation in a Reptile: Roles of Sex, Ecology, Phylogeny and Ecology Structured inPhylogeny. PLoS ONE 9(8): e104026. doi:10.1371/journal.pone.0104026.
3. Baran İ., Avcı A., Kumlutaş Y., Olgun K. and Ilgaz Ç. 2021. Türkiye Amfibi ve Sürüngenleri. Palme Yayınevi, Ankara (in Turkish).
4. Başkale E., Yıldırım E., Çevik I.E. and Kaya U. 2013. Population size and age structure of metamorphic and pedomorphic forms of *Ommatotriton ophryticus* (Berthold, 1846) in the Northwestern Black Sea Region of Turkey. Journal of Herpetology, 47(2): 270–276.
5. Berven K.A. 1982. The genetic basis of altitudinal variation in the wood frog *Rana sylvatica* II. An experimental analysis of larval development. Oecologia, 52: 360–369.
6. Bülbül U. and Kutrup B. 2013. Morphological and genetic variation of *Ommatotriton* in Turkey. Animal Biology 63(3): 297–312.
7. Bülbül U., Kurnaz M., Eroğlu A.İ., Koç H. and Kutrup B. 2016. Age and growth of the red-belied lizard, *Darevskia parvula*. Animal Biology, 66(2016): 81–95.
8. Bülbül U., Kutrup B., Eroğlu A.İ., Koç H., Kurnaz M. and Odabaş Y. 2018. Life history traits of a Turkish population of the Yellow-bellied Toad, *Bombina variegata* (Linnaeus, 1758). Herpetozoa, 1(1/2): 11–19.
9. Bülbül U., Zaman E. and Koç-Gür H. 2021. Zonguldak Amfibi ve Sürüngenleri, Gökçe Ofset Matbaacılık Ltd. Şti, Ankara (in Turkish).
10. Castanet J. and Smirina E.M. 1990. Introduction to the skeletochronological method in amphibians and reptiles. Annales des Sciences Naturelles-Zoologie et Biologie Animale, 11: 191–196.
11. Castanet J. 1994. Age estimation and longevity in reptiles. Gerontology, 40: 174–192.
12. Eroğlu A.İ., Bülbül U., Kurnaz M. and Odabaş Y. 2018. Age and growth of the common wall lizard, *Podarcis muralis* (Laurenti, 1768). Animal Biology, 68 (2018): 147–159.
13. Esteban M., Garcia-Paris M., Castanet J. (1996). Use of bone histology in estimating the age of frogs (*Rana perezi*) from a warm temperate climate area. Canadian Journal Of Zoology, 74: 1914–1921.

14. Guarino F.M. and Erişmiş, U.C. 2008. Age determination and growth by skeletochronology of *Rana holtzi*, an endemic frog from Turkey. Italian Journal of Zoology, 75: 237–242.
15. Gümüş-Özcan Ç. and Üzüm N. 2015. Body size and age in three populations of the northern banded newt *Ommatotriton ophryticus* (Berthold, 1846) from Turkey. Turkish Journal of Zoology, 39: 672–679.
16. Jakob C., Seitz A., Alain C. and Miaud C. 2002. Growth cycle of the marbled newt (*Triturus marmoratus*) in the Mediterranean region assessed by skeletochronology. Amphibia-Reptilia, 23: 407–418.
17. Kleinenberg S.E. and Smirina, E.M. 1969. A contribution to the method of age determination in amphibians. Zoologicheskii Zhurnal, 48: 1090–1094.
18. Kutrup B., Bülbül U. and Özdemir N. 2005. Age structure in two populations of *Triturus vittatus ophryticus* at different altitudes. Amphibia-Reptilia, 26(1):49–54.
19. Kuzmin S.L. 1999. The Amphibians of the former Soviet Union. Pensoft, Sofia (in Bulgaria).
20. Litvinchuk S.N., Zuiderwijk A., Borkin L.J. and Rosanov J.M. 2005. Taxonomic status of *Triturus vittatus* (Amphibia: Salamandridae) in western Turkey: trunk vertebrae count, genome size and allozyme data. Amphibia-Reptilia, 26(2005): 305–323.
21. Miaud C., Guyetant R. and Elmberg J. 1999. Variations in life history traits in the common frog *Rana temporaria* (Amphibia: Anura): A literature review and new data from the French Alps. Journal of Zoology, 249:61–73.
22. Smirina E.M., 1972. Annual layers in bones of *Rana temporaria*. Zoologicheskii Zhurnal, 51: 1529-1534.
23. Tarkhnishvili D.N. and Gokhelashvili R.K. 1999. The amphibians of the caucasus. Advances in amphibian research in the former Soviet Union. Pensoft, Sofia (in Bulgaria).
24. Üzüm N., Avcı A., Olgun K., Bülbül U., Fahrbach M., Litvinchuk S.N. and Wielstra, B. 2019. Cracking cryptic species: external characters to distinguish two recently recognizedbanded newt species (*Ommatotriton ophryticus* and *O. nesterovi*). Salamandra, 55(2):131–134.
25. van Riemsdijk I., Arntzen J.W., Bogaerts S., Franzen M., Litvinchuk S.N., Olgun K. and Wielstra B. 2017. The Near East as a cradle of biodiversity: A phylogeography of banded newts (genus *Ommatotriton*) reveals extensive inter- and intraspecific genetic differentiation. Molecular Phylogenetics and Evolution, 114(2017) 73–81.

26. Wells, A. (2007). Cognition about cognition: Metacognitive therapy and change in generalized anxiety disorder and social phobia. Cognitive and Behavioral Practice, 14(1), 18–25.
27. Ryser, J., 1988. Determination of growth and maturation in the common frog, *Rana temporaria*, by skeletochronology, Journal of Zoology, 216: 673–685.



Figure 1. Map showing the locality (Aksu-Devrek, Zonguldak) of studied samples of *O. nesterovi*.

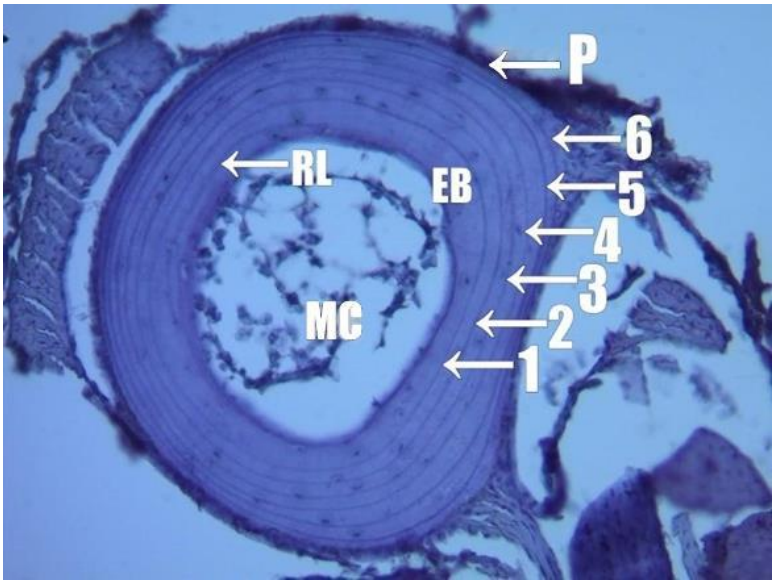

Figure 2. A cross-section (10 µm thick) of a phalange of a sex-year-old male (45.01 mm SVL) *O. nesterovi* from the Aksu population. For abbreviations, see text (MC, Marrow Cavity; EB, Endosteal Bone; RL, Resorption Line; P, Periphery). Periphery wasnot regarded as a LAG

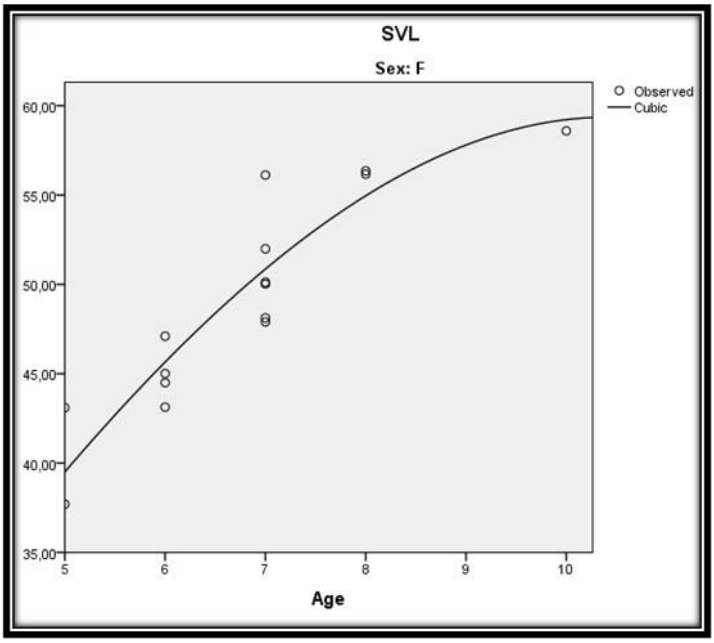

Figure 3. Age-SVL relationships of female individuals of *O. nesterovi* from Aksu population [(SVL (mm), age (year)]

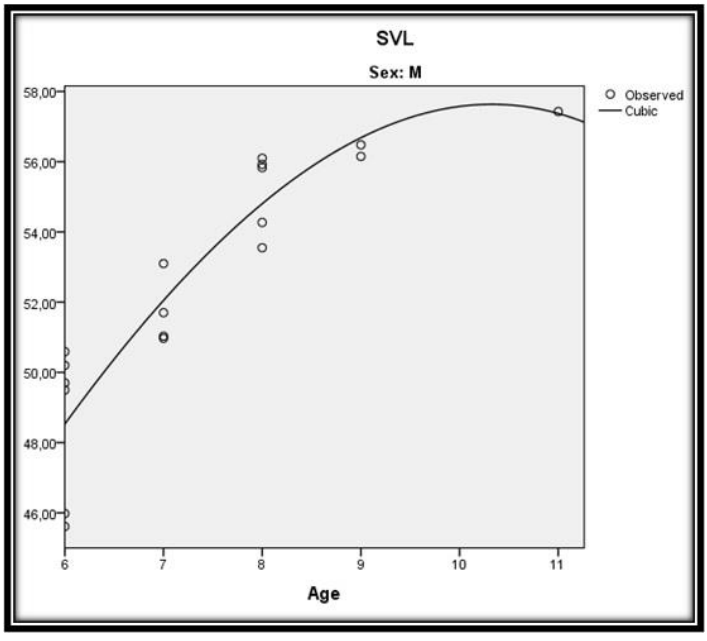

Figure 4. Age-SVL relationships of male individuals of *O. nesterovi* from Aksu population [(SVL (mm), age (year)]

Chapter 9

Leaves of Kermes Oak Induces a Priming Effect on Soil Organic Carbon Mineralization

Şahin CENKSEVEN[1]
Burak KOÇAK[2]

1 Lecturer Dr., Department of Soil Science and Plant Nutrition, Faculty of Agriculture, Cukurova University, E-mail: scenkseven@cu.edu.tr, ORCID ID: 0000-0003-2330-8668

2 Research Assistant Dr., Department of Biology, Faculty of Science and Arts, Cukurova University, Adana, Turkey, bkocak@cu.edu.tr, ORCID ID: 0000-0003-4144-6079

1. Introduction

Definition of soil organic carbon mineralization, which is one of the important indicators of soil microbial activity, is the conversion of soil organic carbon into carbon dioxide (CO_2) and is a natural and important biochemical process that occurs in the soil (Gregorich et al., 2001). This process plays an active role in the carbon dioxide concentration of the atmosphere, sustainable nutrient support, structural stability and diversity in the soil (Paterson and Sim, 2013). Many biotic and abiotic factors such as temperature, soil moisture, vegetation, soil pH, soil structure and soil organic matter regulate the soil organic carbon mineralization (Cenkseven et al., 2017; Tang et al., 2018; Qui et al., 2018).

Organic matter is the one of most important soil properties that influence the soil quality, fertility and release of greenhouse gases to the atmosphere. It's a both a continuous nutrient supply for the plants and an energy source for the microorganisms required for the decomposition processes in the soil. Most of the changes in the organic matter contents and dynamics were controlled by the soil biological activities and quality and quantity of plant residue inputs in the soil (Hussain et al. 2009).

Organic compounds enter into the soil system through litter, root exudates and dead roots which were decomposed to obtain carbon and nutrients for the growth and maintenance by heterotrophic microorganisms (Fig. 1) (Teklay et al., 2007). Plant residues are important nutrient and energy sources that are required for the growth and proliferation of soil microorganisms (Schimel et al. 2003). Most of the plant and animal residues that were introduced to the soil are breakdown depend on the suitable conditions and carbon dioxide, water, ammonium and some cations and anions as last products pass down to the environment (Çolak, 1995).

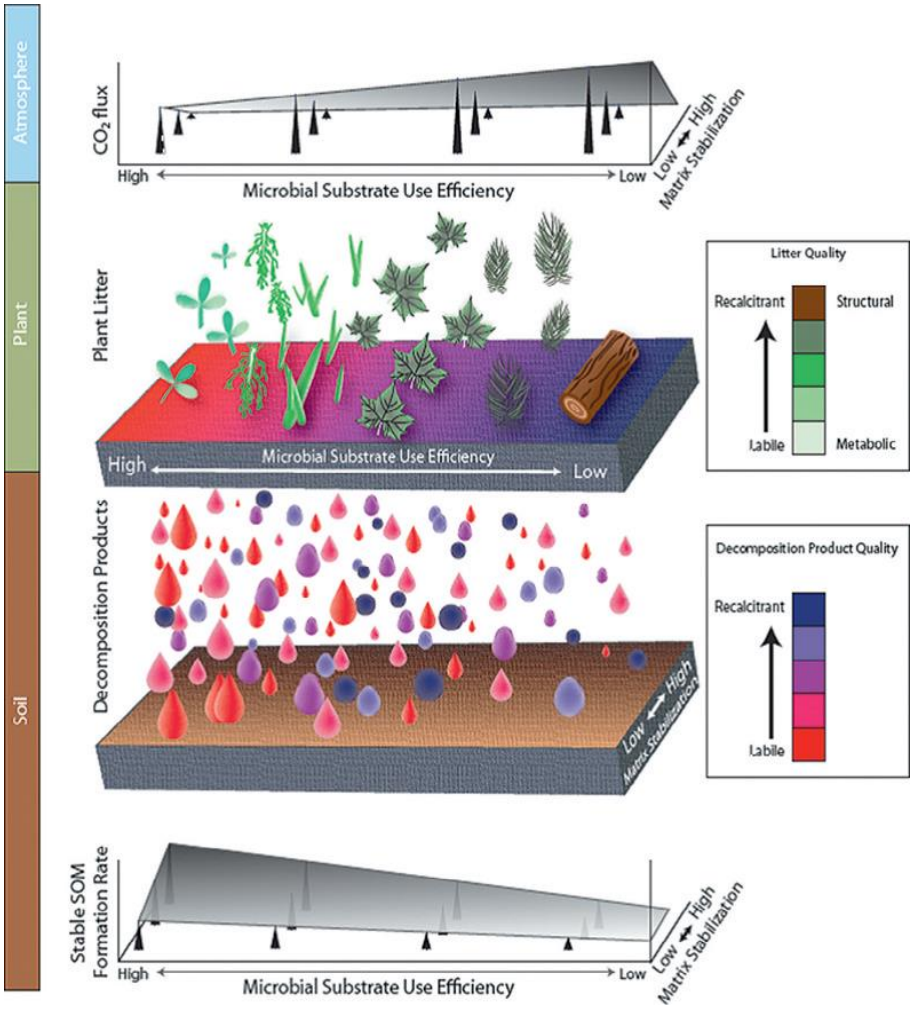

Figure 1 Effects of aboveground and belowground plant materials on soil organic carbon turnover and on quantity and quality of decomposition products (Cotrufo et al., 2013).

Soil organic matter (SOM) mineralization is one of the biggest flows in the global C cycling (Kirschbaum, 2000). Forest SOM is the greatest C sink in the terrestrial ecosystems and it was reported that any change in litter decomposition in the SOM can significantly influence the global C balance (Heimann and Reichstein, 2008). It was noted that understanding the factors regulating SOM turnover is essential for the prediction of terrestrial feedback in the climate change (Finzi et al., 2015). In contrast, fresh organic matter in the process of litter decomposition can produce new soil organic matter (Schlesinger et al., 2016).

Priming effect (PE) is the term that was defined as the stimulation of decomposition of stabilized SOM by fresh organic substrates (Kuzyakov, 2010). PE is characterized as the effects occurred by addition of exogenous substates into the SOM mineralization (Kuzyakov et al., 2000). In many studies, it was shown that addition of exogenous organic matter changed the decomposition of soil organic carbon and thus, PE became a universal phenomenon in the literature (Yu et al., 2019). However, trends of PE inducted by litter showed variability and addition of substate had positive priming (Di Lonardo et al., 2018), negative priming (Zhang and Wang, 2012) or neutral priming effects (Wang et al., 2015). It was known that when high quality litter such as fresh leaves introduced to the soil, microorganisms can decompose soil organic matter by their extracellular enzymes for energy source (Fig. 2) (Cenkseven et al., 2017). In addition, it was reported that litter amount and quality are the important factors that affect the microbial communities in the soil (Berg and McClaugherty, 2014). For instance, it was indicated that when substrates that are resistant to decompose added to the soil, actinomycetes and fungi populations increases (Gul and Whalen, 2013) and labile substates increase the bacterial populations (Meidute et al., 2008). It was reported that any change occurred in the soil microbial community structure can influence the magnitude and trend of SOM mineralization (Yao et al., 2012). Unfortunately, there are a few studies about the effects of plant organs on priming effects and microbial community structure in the literature (Kuzyakov, 2010).

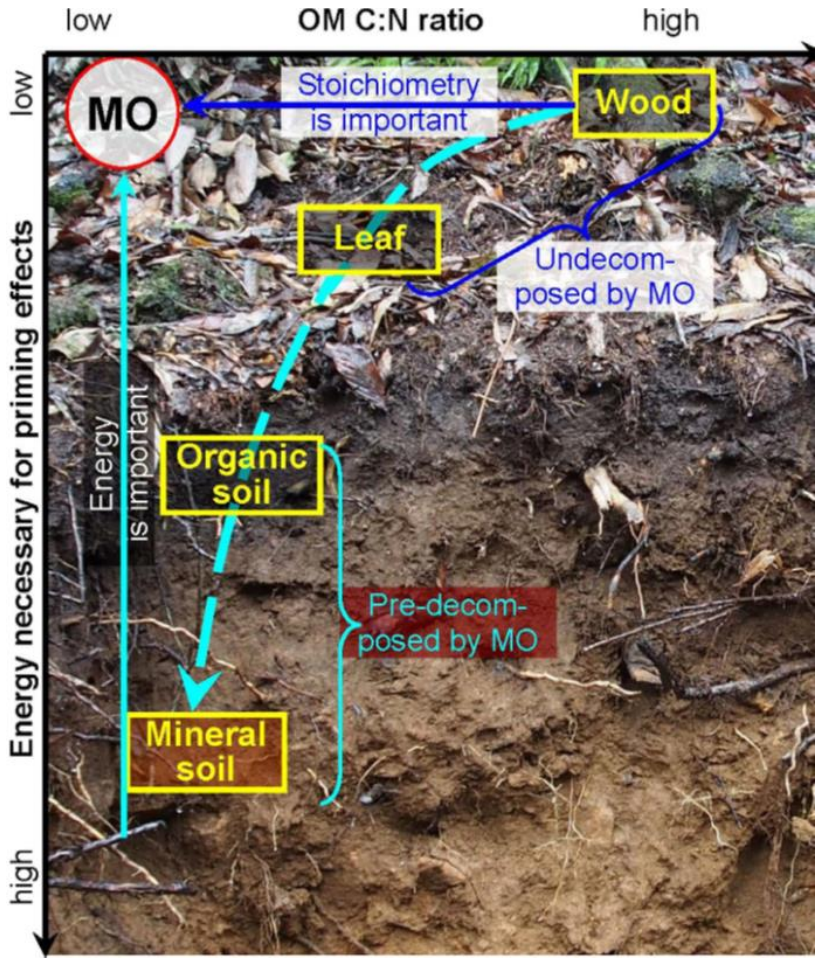

Figure 2 Conceptual model of decomposition of organic matter through priming effects (MO: decomposing microorganisms, OM: organic matter) (Qiao et al., 2016)

Genus Quercus ("meşe" in Turkish language), which belongs to Fagaceae, consists of 32 taxa and is important for the Anatolian forestlands in Türkiye (Güner et al., 2012). Plant species of Quercus are commonly used for the building materials and serve as a food source for animals (mostly goats) (Özcan and Bayçu, 2005). It's estimated that oak trees compose the 26.34% of the forestland in Türkiye (Şenol et al., 2018). *Quercus coccifera* L. (kermes oak) is one of the dominant plant species in the Mediterranean basin which can grow under Mediterranean climate with a long drought period in summer and on many soil types (Babalik et al., 2021).

In this study, the objective of this study was to determine the soil microbial activities of *Quercus coccifera* L. (Kermes oak) and the effects of amendment of their leaves on these activities at different concentrations (0.5% leaves and 1% leaves). For this purpose, soils amended with plant leaves were incubated at 28°C for 52 days to measure soil carbon mineralization. It was hypothesized that due to their different chemical structure, plant leaves have different decomposition rates in the soil and leaf amendments would increase the soil carbon mineralization.

2. Material and Methods

2.1. Material and Study Area

Soil and leaf samples of kermes oak (*Quercus coccifera* L., Fagaceae) have been taken from a in Cukurova University Campus, Adana (37°3'26" N, 35°21'19" E), Turkey, in November 2021. Mean annual precipitation and temperature in Adana were 659 mm and 19.1°C for 35 years and this region had the semi-arid Mediterranean climate (Kum and Celik, 2014).

After air drying, soils of kermes oak were sieved through a 2 mm mesh sieve and kermes oak leaves were powdered before analysis. Soil texture, soil pH and soil field capacity were determined by Bouyoucos hydrometer (Bouyoucos, 1951), a 1:2.5 soil-water suspension with pH-meter (inoLab pH/Cond 720, WTW GmbH, Weilheim, Germany) (Jackson, 1958) and 1/3 atmospheric pressure with a vacuum pump (Demiralay, 1993), respectively. Organic carbon and total nitrogen concentrations in the olive soil, leaf and litter samples were measured by using a modified Walkley and Black method (Anne, 1945) and Kjeldahl method (Bremner, 1965), respectively.

2.2. Soil Carbon Mineralization and Kinetics

Leaves of kermes oak were mixed with its soil at 0.5% (0.5% Leaf) and at %1 (1% Leaf) doses. For this purpose, 100 g soil and leaves were first mixed and then placed in 750 ml incubation vessels. These mixtures were humidified at the 80% of soil field capacity and then were incubated at 28°C for 52 days. Soils untreated with leaves were used as control. As a result of soil microbial activity, CO_2 was trapped periodically by 10 ml 1 M NaOH solution in beakers which are placed in incubation vessels. Amount of respired CO_2 was determined with the titration with 1 M HCl in the incubation vessels (Alef, 1995). Three replicates were used for each treatment and control. After 52 days of incubation, all measured CO_2 during the incubation were summed up to calculate cumulative carbon mineralization (Cmin, mg CO_2-C/100 g soil) and these values were

divided by soil organic carbon level to obtain the rate of Cmin (Koçak and Darici, 2016). A first order kinetic model proposed by Ajwa and Tabatabai (1994) was used to simulate the relationship between the cumulative Cmin quantity and incubation time in all treatments: $C_{min} = C_0\ (1 - e^{-kt})$.$C_{min}$ is the amount of cumulative carbon mineralization through incubation period (days) while C_0 is the quantity of potentially mineralizable carbon in the soil and k (day^{-1}) is the mineralization rate constant.

2.3. Statistical Analysis

The data obtained from the laboratory incubation were submitted to ANOVA to show the differences between treatments by using the SPSS v.20 software. The separation of averages of control and treatments were made by using Tukey's HSD and differences between the means of control and treatments were declared as significant at $P<0.05$.

3. Results and Discussion

3.1. Some Properties of Kermes Oak Soil and Leaf Samples in Cukurova University Campus

Some physical and chemical properties of kermes oak soils and organic carbon and total nitrogen contents of leaves of kermes oak were given in Table 1. Kermes oak soils were sandy clay loam and slightly basic. Organic carbon, total nitrogen contents and C/N rate of soils were 3.82%, 0.28% and 13.56, respectively (Table 1). Aka and Darici (2005) reported that soils of kermes oak in Cukurova University Campus were sandy loam and slightly basic while while organic carbon, total nitrogen contents and C/N of these soils were 4.41%, 0.39% and 11.2. Cenkseven et al. (2011) reported that soils of kermes oak in Cukurova University Campus were silty loam and slightly basic while organic carbon, total nitrogen contents and C/N of these soils were 2.30%, 0.20% and 11.5. Differences between these latter studies and current study may originated from the different sampling times and locations in Cukurova University Campus. Organic carbon, total nitrogen contents and C/N rate of kermes oak leaves were 39.26%, 1.42% and 27.74.

Table 1. Some physical and chemical properties of kermes oak (*Quercus coccifera* L.) soil and organic carbon and nitrogen contents of kermes oak leaves (mean±standard error, n=3)

	Quercus coccifera	
Soil	Sand (%)	53.17 ± 0.99
	Silt (%)	21.03 ± 1.36
	Clay (%)	25.8 ± 0.78
	Texture	Sandy Clay Loam (SCL)
	FC (%)	29.84 ± 0.26
	pH	7.46 ± 0.02
	C (%)	3.82 ± 0.12
	N (%)	0.28 ± 0.00
	C/N	13.56 ± 0.61
Leaf	C (%)	39.26 ± 0.55
	N (%)	1.42 ± 0.02
	C/N	27.74 ± 0.17

3.2. Influence of Kermes Oak Leaves on Soil Carbon Mineralization

Cumulative carbon mineralizations [mg $C(CO_2)$/100 g soil] in the soils added with kermes oak leaves at 0% as control, 0.5% and 1% were 139.23, 221.73 and 265.49 in the end of incubation period, respectively (Fig. 3). Addition of kermes oak leaves in both amounts significantly stimulated soil carbon mineralization ($P<0.001$).

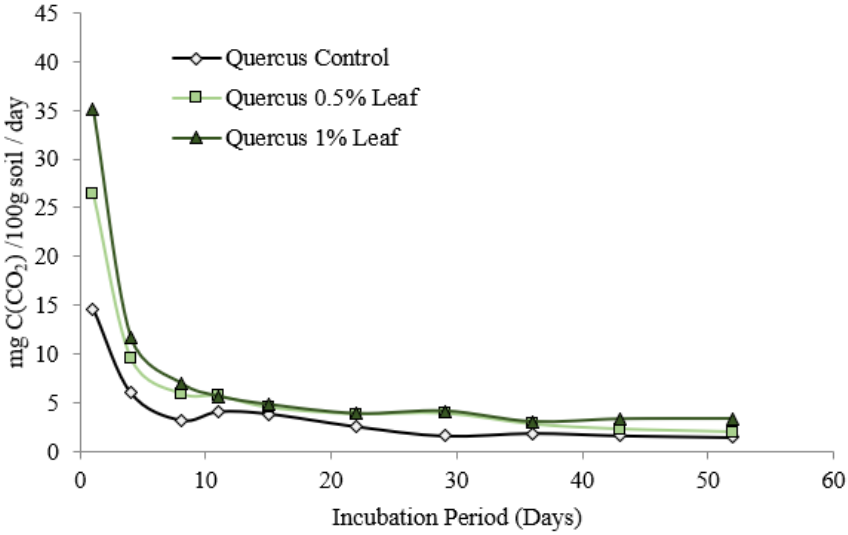

Figure 3 Daily carbon mineralization in the soils added with and without kermes oak leaves (n=3)

Carbon mineralization ratios in the soils added with kermes oak leaves at 0% as control, 0.5% and 1% were found 3.65%, 5.53% and 6.31%, respectively (Fig. 4). Addition of kermes oak leaves in both amounts significantly stimulated the rate of soil carbon mineralization ($P<0.001$).

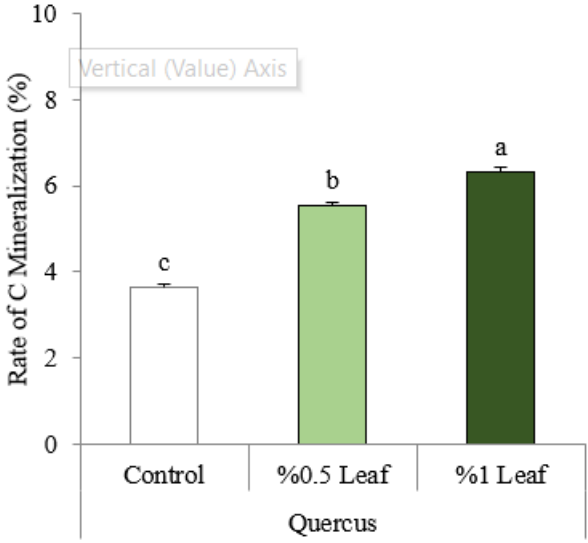

Figure 4 Rate of soil organic carbon mineralization in kermes oak soils added with and without kermes oak soils. Data are the mean values±standard error (n=3). Lowercase letters indicate that values differ significantly between control and treatments on one-way ANOVA followed by Tukey's honestly significant difference test ($P<0.05$)

The first-order equation values of control, 0.5% and 1% leaves for C_0 ($mgC(CO_2)/100g$ soil) were in order as 148.51, 235.90 and 270.55 while k values in the same order were 0.044, 0.046 and 0.048 (Table 2).

Table 2 Parameter estimates according to the first-order equation model for carbon mineralization in the kermes oak soils added with its leaves (C0: potentially mineralizable carbon in the soil, Cmin: mineralized soil carbon at the end of the incubation period, k: mineralization rate constant)

		C_0	k	C_{min}
		$mgC(CO_2)/100g$ soil	(day^{-1})	$mgC(CO_2)/100g$ soil
Quercus	Control	148,51 ± 7,72	0,044 ± 0,005	139,23 ± 0,47
	%0.5 Leaf	235,90 ± 13,54	0,046 ± 0,006	221,73 ± 0,22
	%1 Leaf	270,55 ± 21,15	0,048 ± 0,008	265,49 ± 1,54

If a substrate enters into the soil organic matter (SOM) mineralization externally then there can occur some changes in the mineralization and this is called "Priming Effect (PE)" (Blagodatskaya, and Kuzyakov, 2008). However,

there is no general consensus about the effects of fresh organic matter quality on soil organic carbon (SOC) mineralization/PE (Wang et al., 2015). The input of high-quality organic substrate to the soil, which is characterized by low C/N rate and low lignin content, has been reported to cause a greater (Cenkseven et al., 2017, Boga et al. 2017), an equal (Guenet et al., 2010) or lower positive PE on soil carbon mineralization (Potthast et al., 2010). In the recent years, two theories are explaining the pathways of positive PE when fresh organic matter introduced: 1) Addition of fresh organic matter enhances the growth of microbial populations, releases nutrients and increases SOM mineralization and if the SOM has higher N and other nutrients quantity than this external organic matter, this is defined as "N-mining" theory (Fontaine et al. 2003; Blagodatskaya, and Kuzyakov, 2008) 2) This external fresh organic matter can provide as an energy source for soil microbial populations to produce extracellular enzymes which can decompose recalcitrant SOM and regulate the mineralization of SOM and thus, it is defined as "Co-metabolism" theory (Kuzyakov et al., 2000). According to second theory, it was reported that residues of stems and roots which have high C/N rate and high lignin content can cause lower PE than residues of leaves which have C/N rate close to 20 and low lignin content (Wang et al., 2015). In this study, addition of kermes oak leaves, which have C/N rate close to 30, enhanced soil carbon mineralization at 0.5% and 1%.

Conclusions

This study demonstrated that microorganisms in kermes oak soil can easily mineralize the kermes oak leaves at 0.5% and 1% doses when they were added into the soil. Microflora in kermes oak soil can utilize kermes oak leaves as an energy source for their growth. In summary, kermes oak leaves showed positive priming effects in its soil.

Acknowledgements

This work was funded through Scientific Research Projects Unit in Cukurova University under the project number FBA-2021-12879. Authors thank Ecem Abay, Güneş Ayma and İbrahim Mert Kayıran (Cukurova University, Department of Biology) for their contributions in the soil sampling in the field and soil physical and chemical analysis.

References

1. Aka, H., & Darici, C. (2005). Carbon and nitrogen mineralization in carob soils with Kermes oak and Aleppo pine leaf litter. European Journal of Soil Biology, 41(1-2), 31-38.
2. Alef, K. 1995. Soil Respiration. In: Alef, K. and Nannipieri, P., Eds., Methods in Soil Microbiology and Biochemistry, Academic Press Inc., San Diego, 214-215.
3. Anne, P. 1945. Carbone organique (total) du sol et de l'humus. Ann. Agron., 15: 161-172.
4. Babalik, A. A., Sarikaya, O., & Orucu, O. K. (2021). The Current and future compliance areas of Kermes Oak (Quercus coccifera L.) under climate change in Turkey. Fresenius Environmental Bulletin, 30(01), 406-413.
5. Berg, B., McClaugherty, C., 2014. Plant Litter: Decomposition, Humus Formation, Carbon Sequestration 1st Edition, Kindle Edition, Springer 286p.
6. Blagodatskaya, E., and Kuzyakov. Y. (2008). "Mechanisms of real and apparent priming effects and their dependence on soil microbial biomass and community structure: critical review." Biology and Fertility of Soils 45.2 (2008): 115-131.
7. Boga, T., Aka Sagliker, H., & Cenkseven, S. (2017). The first effect of Eucalyptus camaldulensis leaves and eucalyptol additions on soil carbon mineralization. Fresen. Environ. Bull, 26, 1052-1060.
8. Bouyoucos, G.S., 1951. A Recalibration of the Hydrometer for Mohing Mechanical Analysis of Soil. Agron. Jour., 43: 434-438.
9. Bremner, J.M. 1965. Total nitrogen. In: Black C.A. (Ed). Methods of soil analysis. Part 2, Agronomy 9, American Society of AgronomyInc., Madison, Wisconsin, USA. 1149–1178.
10. Cenkseven, Ş., Darici, C., & Sağliker, H. A. (2011). Farklı kompost oranları ilave edilmiş kermes meşesi topraklarının karbon mineralizasyonu. TÜBAV Bilim Dergisi, 4(3), 172-178.
11. Cenkseven, S., Kocak, B., Kuzu, S.B., Korkmaz-Guvenmez, H., Darici, C. 2017. Response of microbial activity to addition of Nerium oleander L. leaves in soil under different moisture conditions. Fresen. Environ. Bull. 26:377–385
12. Cotrufo, F., Wallenstein, M., Boot, C., Denef, K., Paul, E.A., 2013. The molecular efficiency-matrix stabilization (MEMS) framework integrates plant litter decomposition with soil organic matter stabilization. Do labile

plant inputs form stable soil organic matter? Glob. Chang. Biol. http://dx.doi.org/10.1111/gcb.12113.
13. Çolak, A.K. 1995. Toprak Mikrobiyolojisi ve Biyokimyası. Çukurova Üniv. Ziraat Fakültesi. Yayın No: 98.
14. Demiralay, İ., 1993. Toprak Fiziksel Analizleri. Atatürk Üniversitesi Ziraat Fakültesi Yayınları No: 143, Erzurum, sf: 78-89.
15. Di Lonardo, D.P., Manrubia, M., De Boer, W., Zweers, H., Veen, G.F., Van der Wal, A., 2018. Relationship between home-field advantage of litter decomposition and priming of soil organic matter. Soil Biology & Biochemistry 126, 49-56.
16. Fontaine, S., Mariotti, A., & Abbadie, L. (2003). The priming effect of organic matter: a question of microbial competition?. Soil Biology and Biochemistry, 35(6), 837-843.
17. Finzi, A.C., Abramoff, R.Z., Spiller, K.S., Brzostek, E.R., Darby, B.A., Kramer, M.A., Phillips, R.P., 2015. Rhizosphere processes are quantitatively important components of terrestrial carbon and nutrient cycles. Global Change Biology 21: 2082-2094.
18. Gregorich, E.G., Turchenek, L.W., Carter, M.R., Angers, D.A. 2001. Soil and Environmental Science Dictionary. CRC Press. 1–600.
19. Guenet, B., Neill, C., Bardoux, G., & Abbadie, L. (2010). Is there a linear relationship between priming effect intensity and the amount of organic matter input?. Applied Soil Ecology, 46(3), 436-442.
20. Gul, S., Whalen, J., 2013. Plant Life History and Residue Chemistry Influences Emissions of CO_2 and N_2O From Soil Perspectives for Genetically Modified Cell Wall Mutants. Critical Reviews in Plant Sciences 32: 344-368.
21. Güner A, Aslan S, Ekim T, Vural M, Babaç MT (eds.). (2012). Türkiye Bitkileri Listesi (Damarlı Bitkiler). İstanbul, Turkey: Nezahat Gökyiğit Botanik Bahçesi ve Flora Araştırmaları Derneği Yayını.
22. Heimann, M., Reichstein, M., 2008. Terrestrial ecosystem carbon dynamics and climate feedbacks. Nature 451: 289-292.
23. Hussain, S., Siddique, T., Saleem, M., Arshad, M. and Khalid, A. 2009. Chapter 5 Impact of pesticides on soil microbial diversity, enzymes, and biochemical reactions. Advances in Agronomy. Academic Press. Pages 159-200.
24. Jackson, M. L.,1958. Soil Chemical Analysis. Pretice-Hall, Inc. Englewood Cliffs, New Jersey, U.S.A., p: 1-498.

25. Kirschbaum, M.U.F. 2000. Forest growth and species distribution in a changing climate. Tree Physiology 20: 309-322.
26. Kocak, B., Darici, C. 2016. Priming effects of leaves of Laurus nobilis L. and 1,8-cineole on carbon mineralization. Chilean Journal of Agricultural Research, 76: 100–104.
27. Kum, G., & Çelik, M. A. (2014). Impacts of Global Climate Change on the Mediterranean Region: Adana as a Case Study. Procedia-Social and Behavioral Sciences, 120, 600-608.
28. Kuzyakov, Y., Friedel, J.K., Stahr, K., 2000. Review of mechanisms and quantification of priming effects. Soil Biology & Biochemistry 32: 1485-1498.
29. Kuzyakov, Y., 2010. Priming effects: Interactions between living and dead organic matter. Soil Biology & Biochemistry 42: 1363-1371.
30. Meidute, S., Demoling, F., Baath, E., 2008. Antagonistic and synergistic effects of fungal and bacterial growth in soil after adding different carbon and nitrogen sources. Soil Biology & Biochemistry 40: 2334-2343.
31. Özcan T, Bayçu G (2005). Some elemental concentrations in the acorns of Turkish Quercus L. (Fagaceae) taxa. Pak J Bot 37: 361-371.
32. Paterson, E., Sim, A. 2013. Soil-specific response functions of organic matter mineralization to the availability of labile carbon. Global Change Biology, 19: 1562–1571.
33. Potthast, K., Hamer, U., & Makeschin, F. (2010). Impact of litter quality on mineralization processes in managed and abandoned pasture soils in Southern Ecuador. Soil Biology and Biochemistry, 42(1), 56-64.
34. Qiu, H. S., Ge, T. D., Liu, J. Y., Chen, X. B., Hu, Y. J., Wu, J. S., Su, Y. R., Kuzyakov, Y. 2018. Effects of biotic and abiotic factors on soil organic matter mineralization: Experiments and structural modeling analysis, Eur. J. Soil Biol., 84: 27–34.
35. Qiao, N., Xu, X., Hu, Y., Blagodatskaya, E., Liu, Y., Schaefer, D., & Kuzyakov, Y. (2016). Carbon and nitrogen additions induce distinct priming effects along an organic-matter decay continuum. Scientific Reports, 6(1), 1-8.
36. Schimel, J.P., Weintraub, M.N. (2003) The implications of exoenzyme activity on microbial carbon and nitrogen limitation in soil: a theoretical model, Soil Biol. Biochem. 35: 549-563.
37. Schlesinger, W.H., Dietze, M.C., Jackson, R.B., Phillips, R.P., Rhoades, C.C., Rustad, L.E., Vose, J.M., 2016. Forest biogeochemistry in response to drought. Global Change Biology, 22: 2318-2328.

38. Şenol, F. S., Şekeroğlu, N., Gezici, S., Kilic, E., & Orhan, İ. E. (2018). Neuroprotective potential of the fruit (acorn) from Quercus coccifera L. Turkish Journal of Agriculture and Forestry, 42(2), 82-87.
39. Tang, Z., Sun, X., Luo, Z., He, N., Sun, O.J. 2018. Effects of temperature, soil substrate, and microbial community on carbon mineralization across three climatically contrasting forest sites. Ecol. Evol. 8: 879–891.
40. Teklay, T., Nordgren, A., Nyberg, G. and Malmer, A. 2007. Carbon mineralization of leaves from four Ethiopian agroforestry species under laboratory and field conditions. Applied Soil Ecology 35(1): 193-202.
41. Wang, H., Boutton, T.W., Xu, W.H., Hu, G.Q., Jiang, P., Bai, E., 2015. Quality of fresh organic matter affects priming of soil organic matter and substrate utilization patterns of microbes. Scientific Reports 5.
42. Yao, H.Y., Thornton, B., Paterson, E. 2012. Incorporation of C-13-labelled rice rhizodeposition carbon into soil microbial communities under different water status. Soil Biology & Biochemistry 53: 72-77.
43. Yu, X., Chao, L., Zhang, W., Chen, L., Yang, Q., Zhang, G., Wang, S., 2019. Effects of inorganic nitrogen and litters of Masson Pine on soil organic carbon decomposition. Plos One 14, e0222973-e0222973.
44. Zhang, W.D., Wang, S.L., 2012. Effects of NH4+ and NO3- on litter and soil organic carbon decomposition in a Chinese fir plantation forest in South China. Soil Biology & Biochemistry 47: 116-122.

Chapter 10

Variational Approach For Optimal Control of A Nonlocal Elasticity Theory Based-Single Walled Carbon Nanotube Model

Seda GÖKTEPE KÖRPEOĞLU[1]

1 Ph. D. Department of Mathematical Engineering, Faculty of Chemical and Metallurgical Engineering, Yildiz Technical University, Istanbul, Turkey.

1. INTRODUCTION

Applications, where the calculus of variations is directly relevant, are continuously on the rise. There are several now-classic texts on the calculus of variations from up until the mid-1960s, including Weinstock (1952) and Gelfand and Fomin (1963), which can be found in the reference list at the end of the study. The majority of the discussion of variational methods in the classic texts that highlight applications, such as Morse and Feshback (1954) and Courant and Hilbert (1953), often focuses on classical mechanics, including dynamics, statics, vibrations, and elasticity. Since then, books on particular subjects, such as mechanical vibrations, dynamical systems, optimal control theory, elasticity, and finite-element approaches, have simply incorporated the necessary elements of variational calculus (Cassel, 2013).

Because of their potential applications in the fields of physics, nano-engineering, chemistry, construction engineering, and materials science, carbon nanotubes (CNTs), which were discovered by Iijima, have received attention on a global scale (Iijima, 1991). Due of their remarkable electrical, mechanical, electrochemical, and thermal features, CNT analysis has recently attracted the attention of numerous researchers (Liu et al., 2005; Wang and Ni, 2008; Lee and Chang, 2009). At a critical flow velocity, the CNTs' structural stability could become unstable. Nevertheless, when the CNTs are placed in an uncomfortable surrounding elastic media such a polymer matrix, the effects of flow velocity on the resonance frequencies and the instability of CNTs would be altered. The effect of fluid flow on the free vibration and instability of fluid-conveying single-walled carbon nanotubes (SWCNTs) was studied by Reddy et al (Reddy et al., 2007). With reference to nonlocal elasticity theory, an elastic Bernoulli-Euler beam model is created in the study to account for the thermal-mechanical vibration and buckling instability of SWCNT conveying fluid (Chang, 2012).

The aim of economists, engineers, and each of us individually has always been to optimize the systems, processes, and things that we develop, supervise, and manage. Heuristic optimization approaches are gradually giving way to the unified theory of optimization and control based on variational principles described in this study as they become more and more mathematically founded. The calculus of variations has some of its most extensive applications in the fields of optimization and control, where mathematics and applications are closely related. Variational calculus is used to address the optimization or control objective if it is specified as an integral objective.

In this study, we focus on a control system, which is governed by a partial differential equation modelled as SWCNT. Unlike the linear quadratic problem

for discrete systems, the application of optimal control theory to partial differential state equations may not provide for a straightforward formulation.

2. THERMAL-NONLOCAL BEAM MODEL

Numerous studies have shown that the traditional Euler-elastic beam offers a straightforward and trustworthy model for the total mechanical deformation of carbon nantubes (CNTs), given that the characteristic wavelength is significantly larger than the CNTs' diameter. Chang analyzed the impacts of temperature change, nonlocal small scale, and elastic medium constant on the vibration frequency and buckling instability of fluid-conveying single-walled carbon nanotube (SWCNT) based on the nonlocal elasticity theory and traditional Bernoulli-Euler beam model, as illustrated in Figure 1 (Chang, 2012). SWCNT is supposed to be fixed at both ends and embedded in an elastic media, such as polymer, in this study. The SWCNT's length is represented by the character L. Let U and M stand for the fluid's mass per unit length and mean flow velocity, respectively. Based on nonlocal elasticity theory, the governing equation for thermal vibration and structural instability of an SWCNT conveying fluid can be written as (Chang, 2012)

$$Aw_{xxxx} - Bw_{xxxt} - Cw_{xxtt} + Dw_{xx} + Ew_{xt} + Fw_{tt} + Kw = 0 \quad (1)$$

in which

$$\begin{aligned} A &= EI + (e_0a)^2N_t - (e_0a)^2MU^2, \\ B &= 2(e_0a)^2MU, \\ C &= (e_0a)^2(M+m), \\ D &= MU^2 - N_t - (e_0a)^2K, \\ E &= 2MU, F = M + m. \end{aligned} \quad (2)$$

where subscripts represent partial differentiation with respect to the indicated variable. In equation (1), $w(x,t)$ is the SWCNT's deflection, t is time, x is an axial coordinate, m is its mass per unit length, E and I are its Young's modulus and moment of inertia, and K is the Winkler constant of the surrounding elastic medium, which is referred to as a Winkler-like elastic foundation (Fu et al., 2006). N_t is the axial force that is constant as a result of thermal processes. The small scale coefficient (e_0a) is used to account for small size effects. The SWCNT is

defined as fixed at both ends in the current study. Accordingly, the SWCNT's boundary and initial conditions are

$$w(0,t) = \frac{\partial w(0,t)}{\partial x} = w(L,t) = \frac{\partial w(L,t)}{\partial x} = 0, \qquad (3)$$
$$w(x,0) = w_0(x), \qquad \frac{\partial w(x,0)}{\partial t} = w_1(x).$$

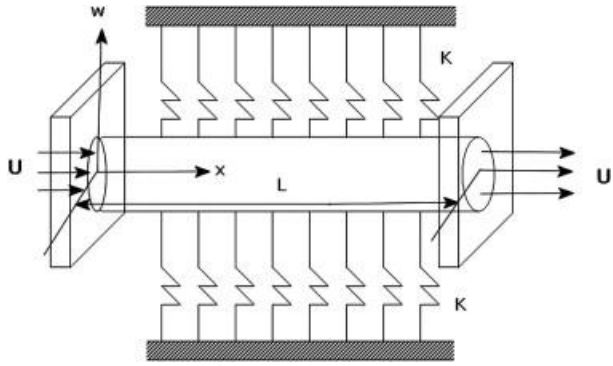

Figure 1. A single-walled carbon nanotube that is capable of transporting fluid with two fixed ends (Chang, 2012).

3. OPTIMAL CONTROL PROBLEM WITH QUADRATIC COST

We consider a single-walled carbon nanotube conveying fluid based on nonlocal elasticity theory. The control input is $\phi(t) = F(t)$ since the control is imposed by the external force $F(t)$. We search for a state equation (1) solution that minimizes the following cost, or objective, functional throughout the time range $0 \leq t \leq t_f$, as well as the corresponding control input $\phi(t)$

$$\mathcal{J}[w,\phi] = \frac{1}{2}\int_0^{t_f}\int_0^{L}(\gamma^2 w^2 + \phi^2)dxdt. \qquad (4)$$

In general, the performance measure is the first term, and the penalty function is the second term. Time and space are both included in the definite integral.

4. VARIATIONAL APPROACH

The state (governing) equation (1) must be satisfied in order for the functional (4) to be minimized subject to differential constraint. To do this, we introduce the Lagrange multiplier $\lambda(x,t)$ and integrate to create the augmented functional in equation (4). The influence function here is the Lagrange multiplier (adjoint variable), and it shows how sensitive the cost function is to changes in the system's state (Cassel, 2013).

$$\begin{aligned}\tilde{J}[w,\phi,\lambda] = \int_0^{t_f}\int_0^{L}\Big\{&\frac{1}{2}(\gamma^2 w^2+\phi^2)+\lambda(x,t)(Aw_{xxxx}\\ &-Bw_{xxxt}-Cw_{xxtt}+Dw_{xx}+Ew_{xt}+Fw_{tt}\\ &+Kw-\phi)\Big\}dxdt.\end{aligned} \tag{5}$$

Taking $\delta\tilde{J}=0$ gives

$$\begin{aligned}\int_0^{t_f}\int_0^{L}\{&\gamma^2 w\delta w+\phi\delta\phi+\lambda(A\delta w_{xxxx}-B\delta w_{xxxt}-C\delta w_{xxtt}\\ &+D\delta w_{xx}+E\delta w_{xt}+F\delta w_{tt}+K\delta w\\ &-\delta\phi)\}dxdt=0.\end{aligned} \tag{6}$$

The terms that contain derivatives are then integrated by parts. The third term is integrated by parts twice according to

$$A\int_0^{t_f}\int_0^{L}\lambda\delta w_{xxxx}dxdt$$

$$\begin{aligned}&=\int_0^{t_f}\Big[A\lambda(L,t)\delta w_{xxx}(L,t)\\&-A\lambda(0,t)\delta w_{xxx}(0,t)\\&-A\lambda_x(L,t)\delta w_{xx}(L,t)\\&+A\lambda_x(0,t)\delta w_{xx}(0,t)\\&+A\lambda_{xx}(L,t)\delta w_x(L,t)\\&-A\lambda_{xx}(0,t)\delta w_x(0,t)\\&-A\lambda_{xxx}(L,t)\delta w(L,t)\\&+A\lambda_{xxx}(0,t)\delta w(0,t)\\&+A\int_0^{L}\lambda_{xxxx}\delta w dx\Big]dt\end{aligned}\tag{7}$$

The fourth term produces

$$-B\int_0^{t_f}\int_0^{L}\lambda\delta w_{xxxt}dxdt$$

$$\begin{aligned}&=\int_0^{L}\big[-B\lambda\big(x,t_f\big)\delta w_{xxx}\big(x,t_f\big)\\&+B\lambda(x,0)\delta w_{xxx}(x,0)\big]dx\\&+B\int_0^{t_f}\Big[\lambda_t(L,t)\delta w_{xx}(L,t)\\&-\lambda_t(0,t)\delta w_{xx}(0,t)-\lambda_{xt}(L,t)\delta w_x(L,t)\\&+\lambda_{xt}(0,t)\delta w_x(0,t)+\lambda_{xxt}(L,t)\delta w(L,t)\\&-\lambda_{xxt}(0,t)\delta w(0,t)-\int_0^{L}\lambda_{xxxt}\delta w dx\Big]dt\end{aligned}\tag{8}$$

The fifth term brings about

$$
\begin{aligned}
&-C\int_0^{t_f}\int_0^{L}\lambda\delta w_{xxtt}dxdt \\
&=\int_0^{L}\big[-C\lambda\big(x,t_f\big)\delta w_{xxt}\big(x,t_f\big)+C\lambda(x,0)\delta w_{xxt}(x,0) \\
&\qquad\qquad +C\lambda_t\big(x,t_f\big)\delta w_{xx}\big(x,t_f\big) \\
&\qquad\qquad -C\lambda_t(x,0)\delta w_{xx}(x,0)\big]dx \\
&\qquad\qquad +\int_0^{t_f}[-C\lambda_{tt}(L,t)\delta w_x(L,t) \\
&\qquad\qquad +C\lambda_{tt}(0,t)\delta w_x(0,t)+C\lambda_{xtt}(L,t)\delta w(L,t) \\
&\qquad\qquad -C\lambda_{xtt}(0,t)\delta w(0,t)]dt \\
&\qquad\qquad -C\int_0^{t_f}\int_0^{L}\lambda_{xxtt}\delta w dxdt
\end{aligned}
\tag{9}
$$

The sixth term generates

$$
\begin{aligned}
&D\int_0^{t_f}\int_0^{L}\lambda\delta w_{xx}dxd \\
&\qquad\qquad =D\int_0^{t_f}[\lambda(L,t)\delta w_x(L,t)-\lambda(0,t)\delta w_x(0,t) \\
&\qquad\qquad -\lambda_x(L,t)\delta w(L,t)+\lambda_x(0,t)\delta w(0,t)]dt \\
&\qquad\qquad +D\int_0^{t_f}\int_0^{L}\lambda_{xx}\delta w dxdt
\end{aligned}
\tag{10}
$$

The seventh term results in

$$E\int_0^{t_f}\int_0^{L}\lambda\delta w_{xt}dxdt$$
$$= E\int_0^{L}\big[\lambda(x,t_f)\delta w_x(x,t_f) - \lambda(x,0)\delta w_x(x,0)\big]dx - E\int_0^{t_f}[\lambda_t(L,t)\delta w(L,t) - \lambda_t(0,t)\delta w(0,t)]dt + E\int_0^{t_f}\int_0^{L}\lambda_{xt}\delta w dxdt \quad (11)$$

The eighth term produces

$$F\int_0^{t_f}\int_0^{L}\lambda\delta w_{tt}dxdt$$
$$= F\int_0^{L}\big[\lambda(x,t_f)\delta w_t(x,t_f) - \lambda(x,0)\delta w_t(x,0) - \lambda_t(x,t_f)\delta w(x,t_f) + \lambda_t(x,0)\delta w(x,0)\big]dx + F\int_0^{t_f}\int_0^{L}\lambda_{tt}\delta w dxdt \quad (12)$$

The terms for odd-order derivatives change sign as a result of the integration by parts, but the terms for even-order derivatives do not. The state equation's initial and boundary conditions (3) lead to the conclusion that $\delta w(x,0) = \delta w(0,t) = \delta w(L,t) = 0$ because they are specified and don't change. The following natural boundary conditions should be true for the remaining terms evaluated at the boundaries and at $t = t_f$ to vanish:

$$\lambda(x,t_f) = 0, \qquad \lambda(0,t) = 0, \qquad \lambda(L,t) = 0, \quad (13)$$

that represent the control (adjoint) equation's initial and boundary conditions. Equation (5) is formed again by gathering terms and substituting the remaining terms from the integration by parts.

$$\begin{aligned}\int_0^{t_f}\int_0^{L}\{&A\lambda_{xxxx} - B\lambda_{xxxt} - C\lambda_{xxtt} + D\lambda_{xx} + E\lambda_{xt} + F\lambda_{tt} + K\lambda \\ &+ \gamma^2 w\}\delta w dx dt \\ &+ \int_0^{L}\{-B\lambda(x,t_f)\delta w_{xxx}(x,t_f) \\ &- C\lambda(x,t_f)\delta w_{xxt}(x,t_f) \\ &+ C\lambda_t(x,t_f)\delta w_{xx}(x,t_f) \\ &+ E\lambda(x,t_f)\delta w_x(x,t_f) + F\,\lambda(x,t_f)\delta w_t(x,t_f) \\ &- F\lambda_t(x,t_f)\delta w(x,t_f)\}dx \\ &+ \int_0^{t_f}\int_0^{L}(\phi - \lambda)\delta\phi dx dt = 0.\end{aligned} \tag{14}$$

Each of the equations in square brackets must vanish separately over the whole domain $0 \le x \le L,\ 0 \le t \le t_f$ since $w(x,t)$ and $\phi(x,t)$ vary. Therefore, the necessary equations are

$$A\lambda_{xxxx} = B\lambda_{xxxt} + C\lambda_{xxtt} - D\lambda_{xx} - E\lambda_{xt} - F\lambda_{tt} - K\lambda - \gamma^2 w \tag{15}$$

$$\lambda = \phi \tag{16}$$

Where

$$B\lambda_{xxx}(x,t_f) + C\lambda_{xxt}(x,t_f) = E\,\lambda_x(x,t_f) + F\lambda_t(x,t_f) \tag{17}$$

$$C\lambda_{xx}(x,t_f) = F\,\lambda(x,t_f). \tag{18}$$

Equation (16) is known as the optimality condition because it connects the optimal control $\phi(x,t)$ to the Lagrange multiplier $\lambda(x,t)$, also known as the adjoint variable. Equation (15) is the adjoint equation. As a result, for $w(x,t)$ and $\phi(x,t)$, we have the coupled state equation and control equation. The Lagrange multiplier, also known as the adjoint variable and related expenses to as the adjoint equation, is governed by equation (15). The optimality condition, expressed in equation (16), connects the control variable $\phi(t)$ to the Lagrange multiplier $\lambda(t)$. The coupled state and control equations can be seen as a single boundary-value problem in time with boundary conditions at $t = 0$ and $t = t_f$, or as two initial-value problems to be integrated forward and backward in time, respectively.

CONCLUSION

In this study, a variational approach is used to derive the optimal control conditions to a partial differential equation with domain-based control. The investigated model is utilized to explain the single-walled carbon nanotube model based on nonlocal elasticity theory. This study's optimal control problem uses control to act throughout the domain, and the measurement presupposes that state information is accessible all over the entire domain. However, in many realistic conditions, the state is established by sensors, and the control is carried out by actuators, and it might not be possible to perceive and operate all across the entire domain. As a result, boundary-based control and/or boundary-based performance measures may also be taken into account. The variational approach is used to obtain the necessary optimality conditions in the problem. Using the variational framework, any combination of boundary- or domain-based performance measures or control can be taken into account. The conjugate-gradient method or a modification of Newton's method are two optimization algorithms that can be used as solution methods to the approach outlined here to solve the coupled state-control problem. Sensitivity or influence functions that offer the gradient of the state variables concerning the control variable are used to calculate the gradients.

REFERENCES

1. Cassel, K. W. (2013). Variational methods with applications in science and engineering. Cambridge University Press.
2. Chang, T. P. (2012). Thermal–mechanical vibration and instability of a fluid-conveying single-walled carbon nanotube embedded in an elastic medium based on nonlocal elasticity theory. *Applied Mathematical Modelling*, *36*(5), 1964-1973.
3. Courant, R., & Hilbert, D. (1953). Methods of Mathematical Physics, Interscience Publ. Inc., New York, 1, 173.
4. Fu, Y. M., Hong, J. W., & Wang, X. Q. (2006). Analysis of nonlinear vibration for embedded carbon nanotubes. *Journal of Sound and Vibration*, *296*(4-5), 746-756.
5. Gelfand, I. M., & Fomin, S. V. (1963). Calculus of Variations Prentice-Hall. *Inc., Englewood Cliffs*.
6. Iijima, S. (1991). Helical microtubules of graphitic carbon. nature, 354(6348), 56-58.
7. Lee, H. L., & Chang, W. J. (2009). Vibration analysis of a viscous-fluid-conveying single-walled carbon nanotube embedded in an elastic medium. Physica E: Low-dimensional Systems and Nanostructures, 41(4), 529-532.
8. Liu, J. Z., Zheng, Q. S., Wang, L. F., & Jiang, Q. (2005). Mechanical properties of single-walled carbon nanotube bundles as bulk materials. Journal of the Mechanics and Physics of Solids, 53(1), 123-142.
9. Morse, P. M., & Feshbach, H. (1954). Methods of theoretical physics. *American Journal of Physics*, *22*(6), 410-413.
10. Reddy, C. D., Lu, C., Rajendran, S., & Liew, K. M. (2007). Free vibration analysis of fluid-conveying single-walled carbon nanotubes. Applied Physics Letters, 90(13), 133122.
11. Wang, L., & Ni, Q. (2008). On vibration and instability of carbon nanotubes conveying fluid. Computational Materials Science, 43(2), 399-402.
12. Weinstock, R. (1974). *Calculus of variations: with applications to physics and engineering*. Courier Corporation.

Chapter 11

The Behaviors Of Heavy Ion Therapy In Layer Bio Structures

Fatih EKİNCİ[1]

1 Dr.,

1- Introduction

Heavy ion therapy is a variation of external beam radiotherapy. Heavy ion beams obtained from the accelerator are sent onto the target tissue. Heavy ion beam reduces scattering in tissue. The heavy ion beam coming to the target can leave most of its energy on the tumor without being scattered too much, so that the healthy tissue is not damaged [1-3]. Heavy ion beam provides an advantage in radiotherapy in terms of accumulating the dose in the targeted volume and minimizing the dose in the surrounding healthy tissues [4]. Energy, mass, momentum and charge properties contribute to the interaction of particles with matter. Various absorption and scattering interactions cause excitation or ionization of atoms or molecules of the medium [2,5]. As the heavily charged ions travel through the tissue, they slow down until they stop and gradually lose their energy. When a charged particle enters the medium, it transfers its energy to the medium, approximately inversely proportional to the square of its velocity. For this reason, as the particle slows down, the probability of ionization of the atoms in the environment increases and the maximum dose is transferred to the depth where the ionization events are maximum. All this energy loss is represented by the Bragg curve [6].

The rationale for the clinical use of heavy ion therapy is that higher doses can be given to the tumor and better preservation of healthy tissue compared to photon-utilizing radiotherapy. The main advantage of ions over photons is that the ions stay at a known depth in matter and a maximum energy is stored at the Bragg peak. This effect is characterized by the stopping power, which is defined as the average energy loss of the particle per unit length of the medium, resulting from Coulomb interactions with electrons and atomic nuclei [7]. The doses given in photon radiotherapy are usually at limited energies to prevent harmful effects on healthy tissue. However, higher doses provide higher tumor control [8]. The transfer of a large part of the dose to the tumor is greater for heavy ions than for photons. Because of the high compatibility and calibration that can be achieved with heavy ion therapy, better results have been obtained in the treatment of tumors located very close to critical tissues [3]. The dose given to healthy tissues at risk close to the tumor is low in hadron therapy. Therefore, the use of hadron therapy in tumors of the head and nervous system is common [9].

Organs such as the head, neck and jaw have a layered structure. These layers have different atomic and bulk densities. each layer forming these structures; For example, skin, adipose tissue, cortical bone, brain tissue, tooth enamel, cavities, etc., have properties such as different ionization, recoils, lateral scattering. The heavy ion beam that passes through these layers and goes to the target tissue, decreases and increases in each layer, and processes such as ionization, recoils,

and lateral scattering occur that affect the success of the treatment. In this book chapter, radiotherapy applications close to critical tissues and tissues such as head and teeth are examined. The importance of considering layered textures is emphasized with case studies.

2- Material and Method

In these studies, Monte Carlo (MC) based TRansport of Ions in Matter (TRIM) simulation was used to contribute to the literature since there is no experimental heavy ion beam line. Radiation properties of layered biological structures such as head and teeth were investigated in order to develop new approaches for biophysical dosimetry and define robust criteria. The MC method is a statistical simulation technique developed for the solution of mathematical problems that are difficult to solve analytically. The simulation systems developed on this technique, based on the assumption that the quantities describing particle interactions have certain probability distributions, follow the traces of each particle traveling through matter, one by one. For many particles, quantities such as flux, energy loss and absorbed dose are recorded and average values are calculated for these distributions [10]. The TRIM simulation program, developed using the MC technique, can calculate all interactions of ions within the target. Type of ions, energy, target phantom type and shape, parameter to be calculated, number of particles and probability can be entered on the TRIM screen. The program saves all calculation fields and can be viewed as needed [11].

It is widely accepted that the correct result of the phantom is related to the tissue equivalence of the phantom building materials [12]. Different biomaterials have been proposed for standard different tissue phantoms of the International Atomic Energy Agency (IAEA) [13]. One of the main reasons for this proposition is that the bulk density is close to soft tissue [14]. With the help of MC TRIM simulation, the biological layers that make up the organ were created. Thus, it is aimed to evaluate the stopping powers, Bragg curve properties and nuclear interaction results phantom material properties for each layer. However, although less digitized and understood, interactions such as recoil, collisions events, phonon generation, and lateral scattering have been largely investigated for biological structures [2,3,15]. The head phantom used is shown in Figure 1 and the atomic composition percentages, mass and atomic densities of the biological layers are presented in Table 1. The other phantom used, the dental phantom, is presented in Figure 2 and the atomic composition percentages, mass and atomic densities of the biological layers are presented in Table 2. Biological layers were formed by taking the thickness closest to human physiology [2,3].

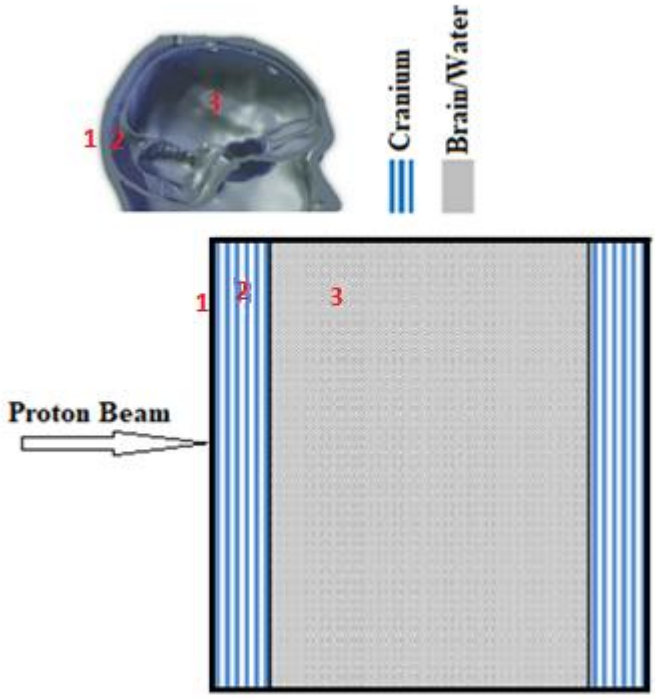

Şekil 1 Başkesiti fantom geometrisi: (1) deri, (2) kortikal kemik (cranium) ve (3) beyin dokusu olarak kurgulanmıştır [15].

Table 1 Atomic percentage (%), atomic density (×1022atom/cm3) and density (g/cm3) of biomaterials and embilization materials used in the cross-section phantom [16]

Biomaterial	Chemical Composition (%)	Atomic density (10^{22}atom/cm^3)	Density (g/cm^3)
1. Skin	H 10; O 59.4; C 25; N 4.6; S 0.3; Cl 0.3; P 10,3; Na 0.2; K 0.1	9.88	1.02
2. Craium	H 3.4; O 43.5; C 15.5; N 4.2; S 0,3; Ca 22.5; P 10.3; Mg 0.2	9.946	1.92
3. Brain	H 10.7; C 14.5; N 2.2; O 71.2; CI 0.3; Na 0.2; P 0.4; S 0.2; K 0.2	8.879	1.04

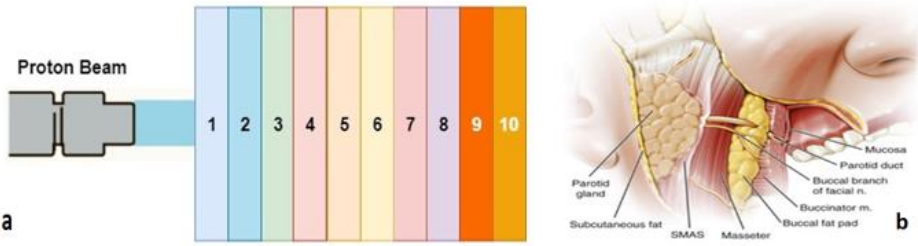

Figure 2. (a) A cross-sectional view of the focused mouth area (b) Molar phantom section of mandibular region tooth plate [2].

Table 1. Atomic percentage, atomic density and density of the biological layers forming from the mandible [16].

Biomaterial	Chemical Composition (%)	Atomic density (10^{22}atom/cm^3)	Density (g/cm^3)
1. Skin	H 10; O 59.4; C 25; N 4.6; S 0.3; Cl 0.3; P 10,3; Na 0.2; K 0.1	9.88	1.02
2. Parotid gland	H 62.5; C 16.4; N 1.27; O19.6; S 0.037; Cl 0.016; Na 0.025; P 0.019	10,32	1,02
3. SMAS	H 58.3; C 37.4; N 1.45; O 1.89; F 0.532; Ca 0.266	10.65	1.027
4. Masseter muscle	H 52.6; C 8.9; N 1.6; O 26.6; S 5.85; Cl 1.76; K 0.64; P 0.404	10.11	1.05
5. Buccal Fat	H 63.4; C 28.4; N 0.304; O 7.77; Cl 0.018; Na 0.011	10.35	0.92
6. Mucosa	H 10.1; C 77.5; N 3.50; O 5.23; F 1.74; Ca 1.83	5.24	1.028
7. Saliva	H 66.6; O 33.3	10.02	1
8. Gum	H 52.6; C 32.9; N 0.862; O 7.89; Cl 1.72; Mg 3.63	8.88	1
9. Cortical bone	H 39.2; C 15; N 3.48; O 31.6; S 0.108; P 3.86; Ca 6.53; Mg 9.57	9.94	1.92
10. Cancellous bone	H 57.7; C 23; N 1.36; O 15.7; S 4.27; P 0.752; Ca 1.26; Fe 1.23	10.42	1.18

3- Results

The results were analyzed in two ways as head and molar phantom. The focus of this review is to discuss the largest LET transmission after the Bragg peak. Thus, the secondary highest ionization that occurs in layered structures is the detection of heavy ion beam and target interaction point. Thus, the presence of structures that affect the Bragg peak range in layered structures and thus affect the course of treatment has been revealed.

3.1 Head plate phantom

The proton beam advancing in the head plate phantom interacted due to the density difference while passing through the biological layers. Since the densities of skin and brain tissue were close to each other, the proton beam showed similar interactions. However, by creating more ionization in cortical bone, which is denser than these two tissues, it created a secondary peak such as Bragg peak as given in Table 3. It was observed that this peak increased with cortical bone thickness in the same energy proton beam. It was observed that the peak value decreased as the energy of the proton beam increased in the same cortical bone thickness. Due to the second peak, the energy of the proton beam decreased. Thus, the Bragg peak position of the proton beam, in other words, its range decreased. This demonstrated the importance of cortical bone in head-based phantom measurements.

Table 3. Bragg peak positions (cm) of protons for cortical bone of different thickness and second peak LET (eV/A) values after cortical bone

Energy	Bragg Peak Location	Second peak (eV/A)
For 0.4		
80	4.9	0.1611
100	7.2	0.1319
120	10	0.1151
140	13.4	0.0938
160	17.1	0.0893
180	21.1	0.0767
200	25.2	0.0783
For 0.6		
80	4.6	0.1668
100	7.3	0.1233
120	10.0	0.1151
140	13.4	0.0945
160	16.9	0.0914
180	20.9	0.0841
200	25.2	0.0730
For 0.8		
80	4.6	0.1735
100	7.1	0.1234
120	10.0	0.1155
140	13.2	0.1029
160	16.7	0.0863
180	20.8	0.0803
200	24.9	0.0745
For 1.0		
80	4.3	0.1816
100	7.3	0.1233
120	9.7	0.1188
140	13.0	0.1040
160	16.7	0.0935
180	20.6	0.0796
200	24.8	0.0791
For 1.2		
80	4.2	0.1352
100	6.8	0.1337
120	9.6	0.1209
140	12.9	0.1053
160	16.7	0.0877
180	20.5	0.0851
200	24.8	0.0778

3.2 Molar plate phantom

Bragg curves were obtained by excluding the parotid gland and masseter layers in the man-dibular molar plate phantom section (Figure 2). This calculations using mandibular tooth plate molar phantom (Figure 2-b), a total of 40 different energy proton bundles were used in the 89.8 -93.7 MeV energy range. With this wide energy range, the maximum LET has been transferred over an area of 60.99-64.9 mm. Referring to Figure 3(a), maximum LET was transferred by forming a Bragg peak at the last 0.87 mm of the cortical bone and 0.65 mm of the cancellous bone. As seen in Figure 4 (b), (c) and (d), Bragg peaks formed along the cancellous bone were formed. Referring to Figure 4 (d), the LET transfer after the Bragg peak occurred in the oral cavity. Bragg curve profile fractures were observed due to LET decrease in the cancellous bone region, which was less dense than cortical bone. As the energy of the proton beam decreased from 89.8 MeV to 93.7 MeV, the Bragg peak amplitude decreased from 0.7567 eV / A to 0.5453 eV / A, which was 28%.

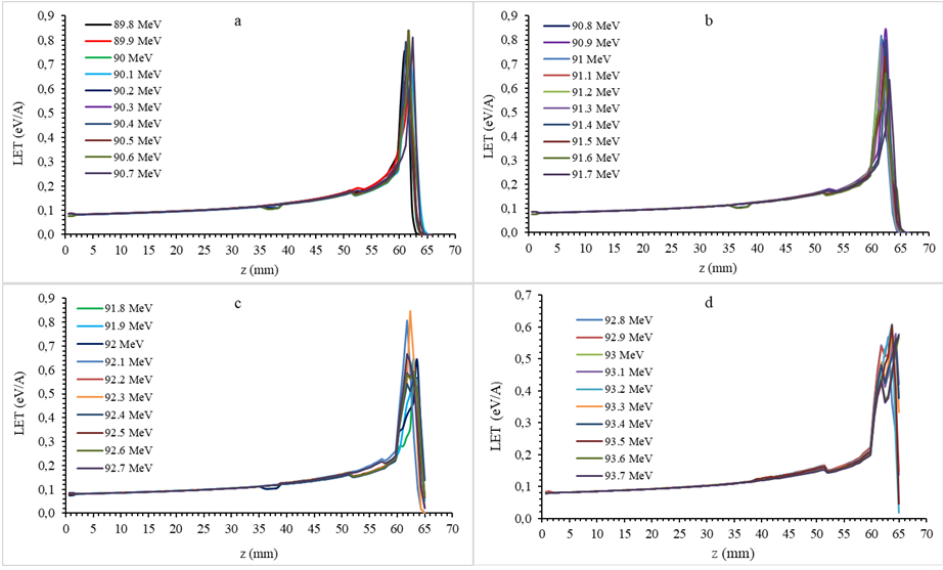

Figure 3. Bragg curves formed by 89.8-93.7 MeV energy protons in molar plate phantom

4- Tartışma

Proton beam therapy is one of the most advanced types of radiotherapy [17]. The physical and radiobiological properties of protons allow a superior dose distribution as compared to current photon (X-ray) radiotherapy, thereby minimizing the dose to normal tissues and significantly reducing acute and late

side effects [18]. Conventional radiation therapy faces challenges from side effects because of a relatively high entrance dose as well as a non-zero exit dose. By contrast, proton therapy has a substantially lower entrance dose and no exit dose that reduces damage to healthy tissue surrounding a tumor [19]. Since the use of proton beam radiothera-py, the number of diseases which can be curatively treated has increased [20]. The method mentioned in this article is designed in phantom jaw model. In future studies, treatment mod-els in which radiation effects are optimized can be applied by working with a patient group and calculating personal tissue thicknesses [2,3,15]. Dosimetry studies have shown an advantage for proton beam therapy compared with photon-based therapy for the treatment of oropharyngeal carcinoma in terms of sparing of multiple critical organs, especially with the use of smaller proton spot sizes [21,22]. In our study, bone and soft tissue thicknesses were established based on previous studies, but a more standardized or individualized method can be developed by using advanced imaging methods to calculate the appropriate LET. Reduction in toxicity potential after radiotherapy using proton therapy has been found in studies [23,24]. In some studies, a significant reduction of the risk of side effects was observed in nearly 70% of the cases, according to existing and validated normal tissue complication probability models [25]. The method mentioned in this article is designed in phantom jaw model. In future studies, treatment models in which radiation effects are optimized can be applied by working with a patient group and calculating personal tissue thicknesses [2,3]. In head and neck cancer, in particular, proton beam therapy is uniquely suited for the complex anatomy of tumors and sensitive surrounding organs [26]. A previous study reported acute toxicities and early outcomes following the use of proton beam therapy for pediatric head and neck malignancies. As a result of the study, it has been found that there are low acute toxicity rates with proton beam therapy and it is safe for the pediatric patient population in accordance with previous studies [3].

5- References

1- Ekinci F., Bostanci E., Güzel M.S., Dagli O. (2022). Effect of different embolization materials on proton beam stereotactic radiosurgery Arteriovenous Malformation dose distributions using the Monte Carlo simulation code. Journal of Radiation Research and Applied Sciences, 15,3, 191-197.

2- Senirkentli G.B., Ekinci F., Bostanci E., Güzel M.S., Dağli Ö., Karim A.M., Mishra A. (2021). Therapy for Mandibula Plate Phantom. Healthcare. 9. 167.

3- Ekinci F., Bölükdemir M.H. (2019). The Effect of the Second Peak formed in Biomaterials used in a Slab Head Phantom on the Proton Bragg Peak. Journal of Polytechnıc. 23,1, 129-136.

4- Khan F.M. (2010). The physics of radiation therapy (Forth Edition), USA: Lippincott Williams & Wilkins, 560.

5- Ekinci F., Bostanci E., Dagli O., Guzel M.S. (2021). Analysis of Bragg Curve Parameters and Lateral Straggle for Proton and Carbon Beam. Communications Faculty of Sciences University of Ankara Series A2-A3 Physical Sciences and Engineering. 2021. 63. 1. 32–41. DOI: 10.33769/aupse.864475

6- Bragg W. H., Kleeman R. (1905). XXXIX. On the α particles of radium, and their loss of range in passing through various atoms and molecules. The London, Edinburgh, and Dublin Philosophical Magazine and Journal of Science, 10(57), 318-340.

7- ICRU Report 49. (1993). International Commission on Radiation Units and Measurements: Stopping Powers and Ranges for Protons and Alpha Particles.

8- Niemierko A., Urie M., Goitein M. (1992). Optimization of 3D radiation therapy with both physical and biological end points and constraints. International Journal of Radiation Oncology* Biology* Physics, 23(1), 99-108.

9- Cozzi L., Fogliata A., Lomax A., Bolsi A. (2001). A treatment planning comparison of 3D conformal therapy, intensity modulated photon therapy and proton therapy for treatment of advanced head and neck tumors. Radiother Oncol. 61(3), 287-97.

10- Foster D.G. (1982). “Avarege Neutronic Properties of “Prompt” Fission Poducts”, Los Alamos National Laboraty Report LA-9168-MS.

11- Ziegler J.F. (2006). SRIM The stopping and range of ion in matter. https://www.srim.org accessed: 20.10.2021

12- Lourenço A., Wellock N., Thomas R., Homer M., Bouchard H., Kanai T., MacDougall N., Royle G., Palmans H. (2016). Theoretical and experimental characterization of novel water-equivalent plastics in clinical high-energy carbon-ion beams. Physics in Medicine and Biology. 61(21), 7623–7638.
13- Arib M., Medjadj T., Boudouma Y. (2006). Study of the influence of phantom material and size on the calibration of ionization chambers in terms of absorbed dose to water. J. Appl. Clin. Med. Phys. 7, 55–64.
14- Samson D.O., Jafri M.Z.M., Shukri A., Hashim R., Sulaiman O., Aziz M.Z.A., Yusof M. F.M. (2020a). Measurement of radiation attenuation parameters of modified defatted soy flour–soy protein isolate-based mangrove wood particleboards to be used for CT phantom production. Radiat. Environ. Biophys. 59. 483–501.
15- Ekinci F., Bostanci E., Guzel M.S.G., Dagli O. (2022). Analysing the effect of a cranium thickness on a Bragg peak range in the proton therapy: a TRIM and GEANT4 based study. St. Petersburg State Polytechnical University Journal. Physics and Mathematics. 15,2, 64–78.
16- ICRU. (1979). International Commission on Radiation Units and Measurements. Average Energy Required to Produce an Ion Pair, ICRU Report 31 (International Commission on Radiation Units and Measurements, Bethesda, MD)
17- Konishi M., Suei Y., Fujita M., Tanimoto K. (2017). Radiographic changes of the mandible after proton beam radiotherapy for oral cancer: A case report. Int. J. Case Rep. Images. 8:787–791.
18- Steneker M., Lomax A., Schneider U. (2006). Intensity modulated photon and proton therapy for the treatment of head and neck tumors, Radiother Oncol. 2006; 80:263–267.
19- Morimoto K., et al. (2014). Particle radiotherapy using protons or carbon ions for unresectable locally advanced head and neck cancers with skull base invasion, Japanese Journal of Clinical Oncology. 44(5):428–434.
20- Konishi M., Suei Y., Fujita M., Tanimoto K. (2017). Radiographic changes of the mandible after proton beam radiotherapy for oral cancer: A case report, Int J Case Rep Images 2017; 8:787–791.
21- Van de Water T., et al. (2011). Potential benefits of scanned intensity-modulated proton therapy versus advanced photon therapy with regard to sparing of the salivary glands in oropharyngeal cancer, Int J Radiat Oncol Biol Phys. 71: 1216-1224.

22- Cozzi L., Fogliata A., Lomax A., Bolsi A. (2001). A treatment planning comparison of 3D conformal therapy, intensity modulated photon therapy and proton therapy for treatment of advanced head and neck tumours, Radiother Oncol. 61: 287-297.
23- Jakobi A., et al. (2015). Identification of patient benefit from proton therapy for advanced head and neck cancer patients based on individual and subgroup normal tissue complication probability analysis, Int J Radiat Oncol Biol Phys. 2015; 92:1165-1174.
24- Langendijk J.A., et al. (2013). Selection of patients for radiotherapy with protons aiming at reduction of side effects: The model- based approach. Radiother Oncol. 107:267-273.
25- Van de Water T., et al. (2008). Comparative treatment planning study between scanned intensity modulated proton therapy and photon therapy in complex oropharyngeal carcinoma, Radiother Oncol. 88:77–78.
26- Leeman J.E., Romesser P.B., Zhou Y., McBride S., Riaz N., Sherman E., Cohen M.A., Cahlon O, Lee N. (2017). Proton therapy for head and neck cancer: expanding the therapeutic window, Lancet Oncol. 18:254-265.

Chapter 12

Fruit Micromorphology Of Some *Myosotis* L. (Boraginaceae) Species From Turkey

Pınar AKDOĞAN ŞİRİN[1]
Öznur ERGEN AKÇİN[2]

1 Ordu University, Fatsa Faculty of Marine Science, ordu, Turkey

2 Ordu University, Faculty of Science and Art, Department of Molecular Biology and Genetics, Ordu, Turkey
email: oakcin@gmail.com

1. Introduction

The genus *Myosotis* is the fourth largest genus in the family Boraginaceae in Turkey. *Myosotis*is represented by 30 taxa (24 species, 3 of which are endemic, 6 subspecies) (Çıngay 2012). Boraginaceae family has been divided into four subfamily according to fruit and stillus characters. The genus *Myosotis* belong to subfamily Boraginoideae (Rendle 2005). *Myosotis* is known as 'unutmabeni' and "mine çiçeği" in Turkish. Some *Myosotis* species are used as ornamental plants because of their beautiful flowers (Heywood 1978; Baytop 1994**)**. Ecological (Dickinson et al. 2007), chemical (Shinkarenko and Vasil'ev 2008), morphological (Pihu et al. 2009) and anatomical (Akçin et al. 2013a) studies were carried out on *Myosotis* species. Metcalfe and Chalk (1979) explained characteristic features of Boragianceae family, including some details of the genus *Myosotis.* Bigazzi et al. (1997) reported that nutlet shape and surface ultrastructure are used to distinguish taxa in Boraginaceae family. The morphology of fruits are used in the taxonomy of *Myosotis.* Especially nutlet shape, attachment structures have major taxonomic importance (Grau 1978).

Studies on the morphology, micromorphological and anatomy of fruits, seeds, stems, flowers e.g. have been useful to support the delimitations of individual or groups of taxa (Juan et al. 2000; Akbulut et al. 2016a, b). Many authors have examined fruit surface micromorphologies by SEM and they stated that fruit micromorphologies play an important role in genera and species delimitation in Boraginaceae (Dasti et al. 2003; Bobrov et al. 2005; Akçin 2007; Akçin 2008; Pakravan et al. 2009; Yu et al. 2012). The aim of the present study was to determine the nutlet surface patterns using the SEM and to demonstrate their taxonomic significance.

2. Material and methods

This study is based on dry herbarium specimens of *Myosotis* taxa from Gazi University Herbarium (GAZİ) and Hacettepe University Herbarium (HUB). The distribution areas and the collection data for the specimens are given in Table 1.

For morphological studies, measurements (widht and lenght) and observations of fruits were made using with Nikon Eclipse 80i NIS-Elements Image Analysis Systems. Fruit types and attachment scar shapes of fruits were obtained with both Light and Scanning Electron Microscopies (SEM). Size, colour, shape and attachment scar shape of examined *Myosotis* species are given in Table 2. The shapes of fruits and attachment scar were drawn with CorelDraw Program (Fig. 1). General features of *Myosotis* taxa were determined as in Grau (1978). For scanning electron microscopy, dried fruits were mounted stubs using double-sided adhesive tape. Samples were coated with 12.5-15 mm of gold. Coated fruits

were examined and photographed with JEOL-JMS 6060 Scanning Electron Microscope. General appearances of nutlets were photographed with SEM (Fig. 2). Attachment scar shape of nutlets (Fig. 3) and surface types of nutlets (Fig. 4) were investigated with scanning electron microscope. Observations were made on the surface patterns of fruits as in Stearn (1985). Fruit surface types and micromorphological properties of examined *Myosostis* species were showed at Table 3.

Table 1 The localities of the examined *Myosotis* taxa

Taxa	Localite	Herbarium Number
Myosotis alpestris F. W. Schmidt subsp. *alpestris* F. W. Schmidt	B8 Bingöl: Bingöl Mountain, Beritan Plateaus, Basalt Rubble; 3000 m. Ekim.	GAZİ-7884
M. arvensis (L.) Hill subsp. *arvensis* (L.) Hill.	A3 Düzce: Akçakoca, Gebeseke Village, hazelnut garden, 75- 90 m. Doğru Koca, 1327.	HUB-1327
M. discolor Pers.	A8 Artvin: Yusufeli, Öğdem, Kapreşet District, fountains environment, 1800 m. Demirkuş, 1562.	HUB-19898
M. heteropoda Trautv.	A5 Amasya: Kuzgeçe Köyü, 500 m. Rocky areas. Peker, 1191.	GAZİ-1191
M. incrassata Guss.	C2 Muğla: Between Fethiye-Çameli, 23 kilometer north of Üzümlü, sparse larch areas, 1396 m. Güner.	GAZİ-14624
M. lazica M. Popov	A8/9 Artvin: Between Pırnallı Village-Kaçkar Mountain,along the forest path, 1600- 3100 m. Demirkuş, 2623.	HUB-2623
M. laxa Lehm subp. *caespitosa*(C. F. Schultz) Hyl. ex Bordh.	A9 Kars: Between Aspacay Tamarlı- Karakale Villages, Doli Creek, moist areas, 1700 m. Ocakverdi, 1816.	GAZİ-1816
M. lithospermifolia (Wild.) Hornem	C3 Isparta: Sütçüler, Kuzca Village, Totabeli, *Pinus nigra* forest, limestone cliffs, 1400- 1500 m. Peşmen & Güner, 2095.	HUB-19943
M. olympica Boiss.	A9 Kars: Between Göle, Karlıyazı, Sürügiden Villages, Harabahive Creek environment. Demirkuş, 1026.	HUB-19957
M. propingua Fisch et. Mey. ex Dc.	A8 Rize: Çamlıhemşin, Orta Yayla Village, Verçenik Plateaus and environment, meadows, annual, 2500 m. Güner & Vural, (AG) 6540.	HUB-19974
M. ramosissima Rochel ex Schultes subsp. *ramosissima* Rochhel ex Schultes	C3 Antalya: Kemer, West of Göymük Creekcoastal dune, 0- 5 m. Peşmen, 3723.	HUB-19980
M. ramosissima Rochel ex Schultes subsp. *uncata* (Boiss. et Bal.) Grau	C2 Muğla: Ortaca, Dalyan- iztuzu, Gökbel Village, 120- 170 m., red pine forest. Vural 5693, Güner, Duman, Dönmez, Mutlu.	GAZİ-5693

M. refracta Boiss. subsp. *refracta* Jaub. et Spach	B4 Kırıkkale: Keskin, Böbrek Mountain Köprü Village, stony places, 1000 m. Güler	GAZİ-1448
M. sicula Guss.	A4 Çankırı, Atkaracalar, Dumanlı Mountain, Ulucay, Haşislamlar Bridge environment, near water, 1200 m. Duran.	GAZİ-1412
M. stricta Link ex Roemer et Schultes	A4 Kırıkkale: Sulakyurt, Kalekışla Village, stony internal of oak forest, 1000 m. Dönmez 2074.	HUB-20003
M. sylvatica Ehrh. ex Hoffm. subsp. *cyanea* Vestergren	A1 Kırklareli: Demirköy, İğne Island, Saka Lake, reeds 0- 5 m. Ekici, 3501.	GAZİ-3501
M. sylvatica Ehrh ex Hoffm. subsp. *rivularis* Vestergen	B6 Kahramanmaraş: Göksun, Binboğa Mountain, Sıcak Plateau, 2700- 2800 m. Aytaç 5457 & Duman.	GAZİ-54578

Table 2 Comparison between morphological characters, attachment scar shape and micromorphological characters of fruits in examined *Myosotis* taxa

Taxa	Nutlet Width (mm) Mean± SD	Nutlet Lenght (mm) Mean± SD	Nutlet Colour	Nutlet Shape	Attachment Scar Shape	Type of Nutlet Surface	Wax
Myosotis alpestris subsp. *alpestris*	1.22 ±0.09	1.89 ±0.20	Blackish-brown	Ovate, Obtuse	Reniform	Rugose	-
M. arvensis subsp. *arvensis*	0.80 ±0.12	1.41 ±0.08	Blackish-brown	Ovate, Narrow obtuse	Reniform	Reticulate- Areolate	-
M. discolor	0.66 ±0.06	1.27 ±0.03	Pale-brown	Wide-Ovate	Reniform	Rugose	-
M. heteropoda	0.77 ±0.12	1.21 ±0.05	Dark-brown	Wide-Ovate, Narrow obtuse	Reniform	Reticulate- Areolate	+
M. incrassata	1.34±0.05	2.18±0.03	Brown	Long-Ovate-Acute	Narrow- Reniform	Elongated	-
M. lazica	0.92 ±0.08	1.75 ±0.05	Dark-brown	Wide-Ovate, Obtuse	Reniform	Rugose	-
M. laxa subsp. *caespitosa.*	1.00 ±0.07	1.85 ±0.04	Dark-brown	Triangular, Obtuse	Reniform	Reticulate- Areolate	+
M. lithospermifolia	1.16 ±0.12	1.70 ±0.05	Black	Wide- Narrow obtuse	Ellipsoid- Reniform	Rugose	-
M. olympica	1.23 ±0.12	2.03 ±1.17	Black	Wide-Ovate, Obtuse	Ellipsoid- Reniform	Rugose	-
M. propingua	1.67 ±0.05	1.71 ±0.05	Pale-brown	Wide-Ovate, Narrow obtuse	Tongue-like	Reticulate	-
M. ramosissima subsp. *ramosissima*	0.74 ± 0.06	1.15 ± 0.02	Pale-brown	Wide-Ovate, Narrow obtuse	Reniform - Triangular	Reticulate- Areolate	-
M. ramosissima subsp. *uncata*	0.75 ±0.08	0.74 ±0.06	Dark-brown	Wide-Narrow obtuse	Narrow- Reniform	Reticulate- Areolate	-
M. refracta subsp. *refracta*	0.57 ±0.08	2.00 ±0.09	Pale-brown	Ovate, Acute	Reniform	Reticulate- Areolate	-
M. sicula	1.15 ±0.13	1.50 ±0.07	Blackish-brown	Wide, Rounded, Obtuse	Reniform with narrow tongue-like	Reticulate- Areolate	-
M. stricta	0.71 ±0.05	1.21 ±0.03	Pale-brown	Wide, Ovate, Narrow obtuse	Reniform	Reticulate- Areolate	-
M. sylvatica subsp. *cyanea*	1.11 ±0.16	1.52 ±0.07	Dark-brown	Wide, Ovate, Obtuse	Reniform	Reticulate- Areolate	+
M. sylvatica subsp. *rivularis*	1.08 ±0.11	2.00 ±0.13	Dark-brown	Wide, Ovate, Obtuse	Ellipsoid-Reniform	Rugose	-

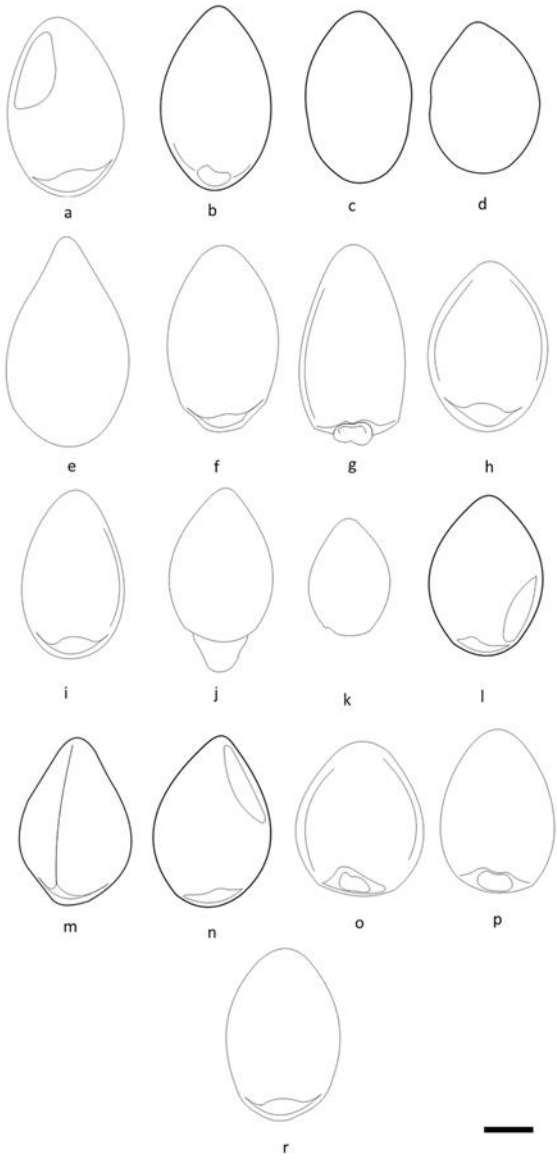

Fig. 1 General appearance of *Myosotis* fruits (with CorelDraw program): a- *M. alpestris* subsp. *alpestris*, b- *M. arvensis* subsp. *arvensis*, c- *M. discolor*, d- *M. heteropoda*, e- *M. incrassata*, f- *M. lazica*, g- *M. laxa* subsp. *caespitosa*, h- *M. lithospermifolia*, i- *M. olympica*, j- *M. propinqua*, k- *M. ramosissima* subsp. *ramosissima* l- *M. ramosissima* subsp. *uncata*, , m- *M. refrecta* subsp. *refrecta*, n- *M. sicula*, o- *M. stricta*, p- *M. sylvatica* subsp. *cyaneae*, r- *M. sylvatica* subsp. *rivularis*. Scale Bar: 0.5 mm.

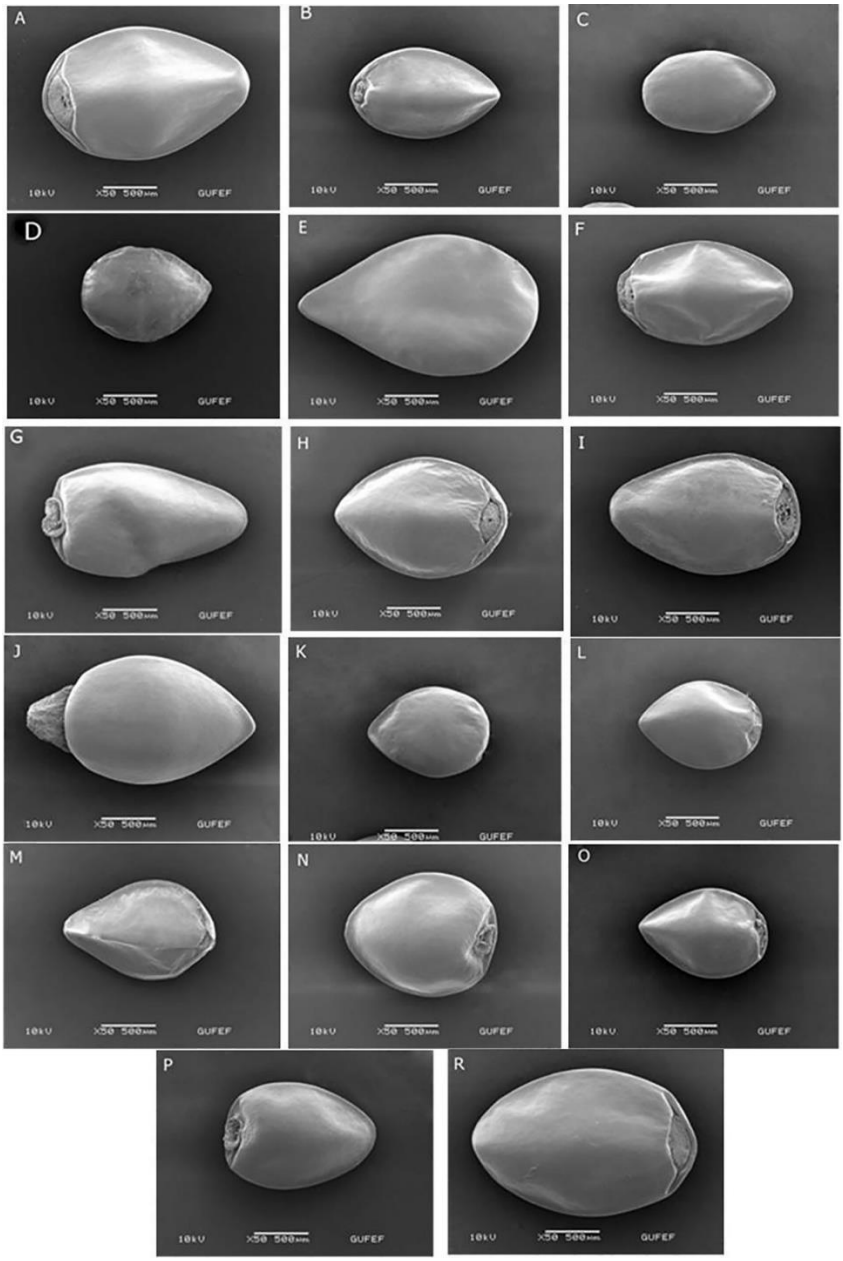

Fig. 2 General apperance of *Myosotis* fruits. A- *M. alpestris subsp. alpestris,* B- *M. arvensis subsp. arvensis,* C- *M. discolor,* D- *M. heteropoda,* E- *M. incrassata,* F- *M. lazica,* G- *M. laxa subsp. caespitosa,* H- *M. lithospermifolia,* I- *M. olympica*, J- *M. propinqua,* K- *M. ramosissima subsp. ramosissima* L- *M. ramosissima subsp. uncata,* M- *M. refrecta subsp. refrecta,* N- *M. sicula,* O- *M. stricta,* P- *M. sylvatica subsp. cyaneae,* R- *M. sylvatica subsp. rivularis.*

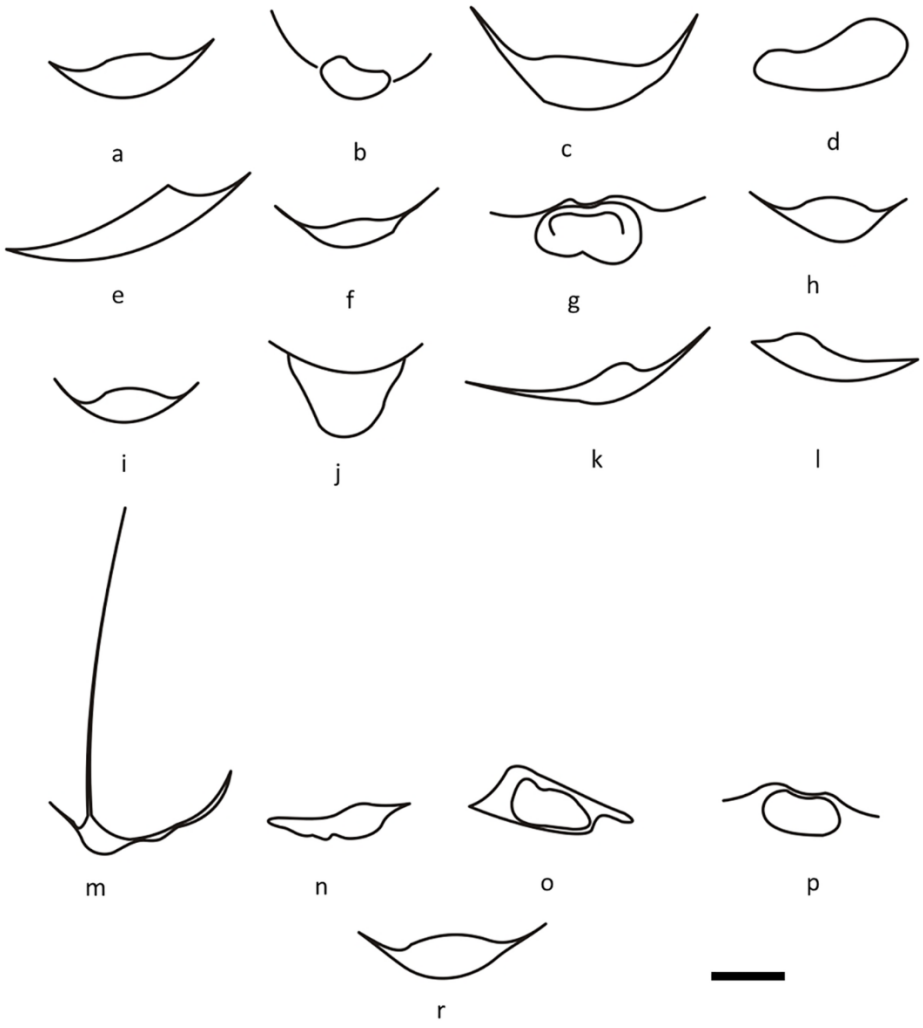

Fig. 3 Attachment scar shapes of *Myosotis* fruits (with CorelDraw program): a- *M. alpestris* subsp. *alpestris,* b- *M. arvensis* subsp. *arvensis,* c- *M. discolor,* d- *M. heteropoda,* e- *M. incrassata,* f- *M. lazica,* g- *M. laxa* subsp. *caespitosa,* h- *M. lithospermifolia*, i- *M. olympica*, j- *M. propinqua,* k- *M. ramosissima* subsp. *ramosissima* l- *M. ramosissima* subsp. *uncata,* m- *M. refrecta* subsp. *refrecta*, n- *M. sicula,* o- *M. stricta,* p- *M. sylvatica* subsp. *cyaneae,* r- *M. sylvatica* subsp. *rivularis* Scale Bar: 100 µm.

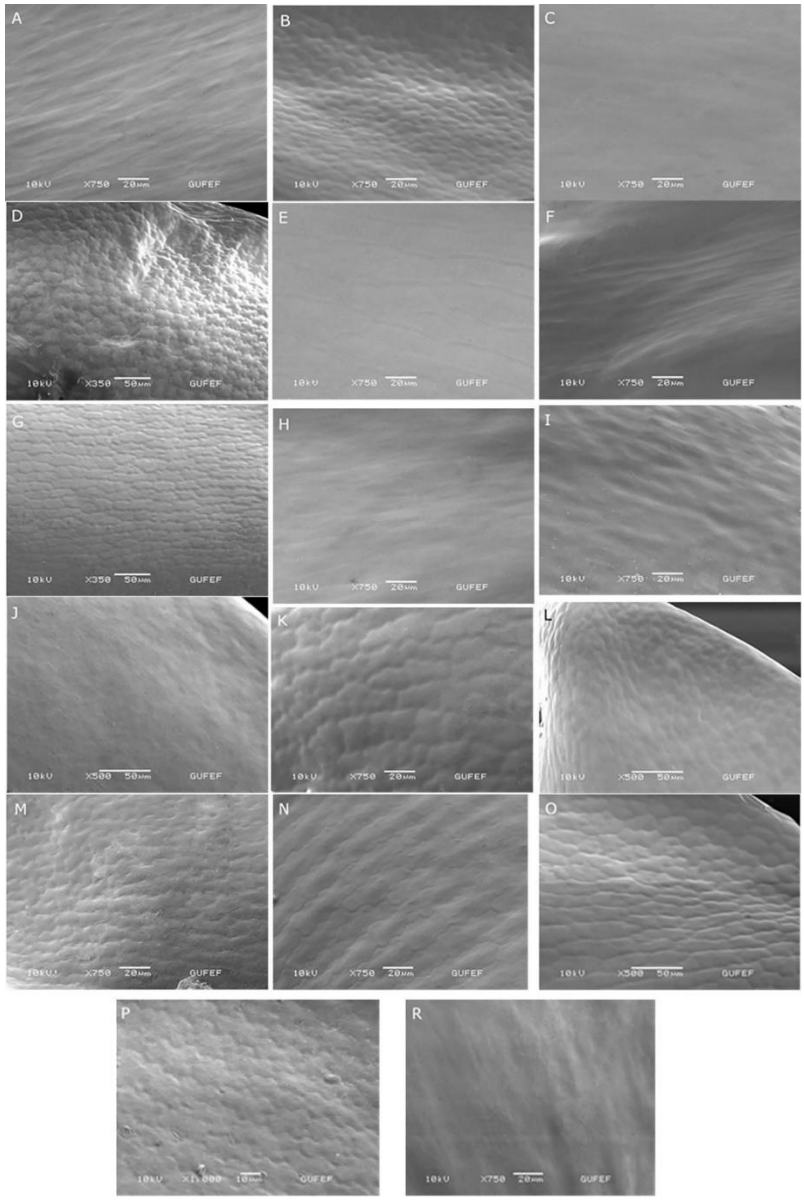

Fig. 4 Fruit surface of the examined *Myosotis* taxa: A- *M. alpestris* subsp. *alpestris*, B- *M. arvensis* subsp. *arvensis*, C- *M. discolor*, D- *M. heteropoda*, E- *M. incrassata*, F- *M. lazica*, G- *M. laxa* subsp. *caespitosa*, H- *M. lithospermifolia*, I- *M. olympica*, J- *M. propinqua*, K- *M. ramosissima* subsp. *ramosissima* L- *M. ramosissima* subsp. *uncata*, M- *M. refrecta* subsp. *refrecta*, N- *M. sicula*, O- *M. stricta*, P- *M. sylvatica* subsp. *cyaneae*, R- *M. sylvatica* subsp. *rivularis*.

Table 3 Fruit epidermal features of examined *Myosotis* taxa

Taxa	Shape	Width (mm) Mean± SD	Lenght (mm) Mean± SD	Structure of Anticlinal Wall	Structure of Periclinal Wall
Myosotis alpestris subsp. *alpestris*	Spindle-shaped	0.06 ± 0.02	0.46 ±0.09	Curved	Smooth-Repand
Myosotis arvensis subsp. *arvensis*	Irregular	0.05 ± 0.01	0.09 ± 0.02	Sinuate	Sinuate
Myosotis discolor	Rectangular	0.09 ± 0.02	0.34 ± 0.08	Smooth or Curvature	Smooth-Repand
Myosotis heteropoda	Irregular	0.09 ± 0.02	0.09 ± 0.02	Sinuate	Sinuate
Myosotis incrassata	Rectangular	0.15 ± 0.04	0.50 ± 0.06	Smooth	Smooth-Repand
Myosotis lazica	Spindle-shaped	0.04 ± 0.01	0.66 ± 0.27	Curvature	Smooth-Repand
Myosotis laxa subsp. *caespitosa*	Irregular	0.07 ± .01	0.23 ± 0.06	Sinuate	Repand
Myosotis lithospermifolia	Spindle-shaped	0.06 ± 0.02	0.17 ± 0.04	Curvature	Smooth-Repand
Myosotis olympica	Spindle-shaped	0.05 ± 0.01	0.18 ± 0.05	Curvature	Smooth-Repand
Myosotis propingua	Rounded	0.05 ± 0.01	0.10 ± 0.02	Repand	Repand
Myosotis ramosissima subsp. *ramosissima*	Rounded	0.11 ± 0.02	0.17 ± 0.05	Repand	Repand
Myosotis ramosissima subsp. *uncata*	Rounded	0.05 ± 0.01	0.11 ± 0.03	Sinuate	Sinuate
Myosotis refracta subsp. *refracta*	Rounded	0.06 ± 0.01	0.17 ± 0.05	Repand	Repand
Myosotis sicula	Rectangular	0.10 ± 0.01	0.31 ± 0.06	Sinuate	Sinuate
Myosotis stricta	Irregular	0.06 ± 0.01	0.19 ± 0.09	Repand	Sinuate or Repand
Myosotis sylvatica subsp. *cyanea*	Irregular	0.09 ± 0.02	0.23 ± 0.05	Sinuate	Sinuate
Myosotis sylvatica subsp. *rivularis*	Spindle-shaped	0.10 ± 0.03	0.42 ± 0.10	Curvature	Smooth-Repand

3. Results And Discussion

3.1. Fruit shape

Fruit type of *Myosotis* species is nutlet. Studied nutlet shapes show variations. Wide-ovate, wide-ovate-obtuse, ovate-acute, long-ovate-acute, ovate-narrow obtuse, triangular, rounded nutlet shapes were observed in studied *Myosotis* taxa. Wide ellipsoid type was main condition. Only *M. sicula* has rounded and *M. laxa* subsp. *caespitosa* has triangular nutlet shape.

Rib structure is very significant in *M. arvensis* subsp. *arvensis*, *M. lazica*, *M. alpestris* subsp. *alpestris*, *M. lithospermifolia*, *M. refracta* subsp. *refracta, M. stricta. M. heteropoda, M. incrassata, M. laxa* subsp. *caespitosa, M. propinqua* and *M. sicula* have not rib structure. The other species have significantly less prominent or not significant rib (Table 2, Figs. 1 - 2).

3.2. Fruit colour

Colour of *Myosotis* nutlets varies from black to light brown. Generally species have dark and light brown nutlets. Two species (*M. lithospermifolia* and *M. olympica*) have black nutlets (Table 2).

3.3. Fruit size

Studied nutlet sizes show some variations. *M. incrassata* has the largest nutlets ($1.34 \pm 0.05 \times 2.18 \pm 0.03$ mm). The smallest nutlets were seen in *M. ramosissima* subsp. *uncata*, *M. discolor*, *M. heteropoda*, *M. ramosissima* subsp. *ramosissima* and *M. stricta* (Table 2).

3.4. Attachment scar shape

Attachment scar shapes show variations in studied *Myosotis* species. Reniform, narrow reniform, ellipsoid reniform, reniform - triangular and narrow tongue shaped scar were seen in studied *Myosotis* taxa. Scar has long and big lateral grooves in *M. alpestris* subsp. *alpestris*. Lateral grooves are short and markedly in *M. lazica*. *M. lithospermifolia, M. olympica* and *M. stricta* has very short lateral grooves. Lateral groove is very big in *M. sylvatica* subsp. *rivularis.* The other species have not lateral groove.

Protruding spongiform structure with reniform shaped was observed at attachment scar of *M. laxa* subsp. *caespitosa, M. sylvatica* subsp. *cyanea. M. sicula* and *M. arvensis* subsp. *arvensis. M. propinqua* has tongue-shaped spongiform structure (Table 2, Fig. 3).

3.5. Fruit surface:

Four surface types were identified as reticulate-areolate, rugose, elongated and reticulate (Table 3, Fig. 4). The most common type is reticulate-areolate. Surface types in the examined taxa as follows:

Reticulate-areolate type: The epidermal cells of surface formed in reticulate-areolate ornamentation. Cell sizes and cell shapes show some variations. Epidermal cells of fruit are irregular shape in *M. arvensis, M. heteropoda, M. laxa* subsp. *caespitosa, M. stricta* and *M. sylvatica* subsp. *cyanea.* Some epidermal cells are rectangular while some are roundish. In *M. ramosissima* subsp. *ramosissima, M. ramosissima* subsp. *uncata* and *M. refracta* subsp. *refracta* have roundish epidermal cells. Only rectangular epidermal cells are seen in *M. sicula.*

Rugose type: Rugose type of fruit surface was observed in *M. alpestris* subsp. *alpestris, M. discolor, M. lazica, M. lithospermifolia, M. olympic*a, *M. sylvatica* subsp. *rivularis*. The epidermal cells of the fruit surface formed in rugose type with varied sizes and shapes. Epidermal cells of fruit surface are rectangular in *M. discolor*. In the other rugose type nutlets have spindle-shaped epidermal cells.

Reticulate type: Reticulate type fruit surface was observed in *M. propinqua*. Epidermal cells of fruit are roundish.

Elongated type: Elongated type fruit surface was observed in *M. incrassata*. Epidermal cells of fruit are rectangular.

3.6. Epidermal cell size

Epidermal cell sizes of fruit surface show some variations. The smallest epidermal cells were seen in *M. arvensis* subsp. *arvensis* ($0.05 \pm .01 \times 0.09 \pm 0.02$ mm), *M. propingua* ($0.05 \pm 0.01 \times 0.10 \pm 0.02$ mm) and *M. ramosissima* subsp. *uncata* (0.05 ± 0.01 x 0.11 ± 0.03 mm). *M. incrassata* and *M. lazica* have the largest epidermal cells (Table 3).

3.7. Cell wall structures

Anticlinal and periclinal walls of epidermal cells are straight, sinuous, curved and repand type. The most common types of anticlinal walls are curved and sinous. Only *M. discolor* and *M. incrassata* have straight anticlinal walls. Generally repand and straight periclinal walls are seen in studied nutlets. Anticlinal and periclinal walls are evident in the most of the epidermal cells (Table 3).

3.8. Epicuticular wax

The epicuticular waxes were observed in *M. heteropoda*, *M. laxa* subsp. *caespitosa* and *M. sylvatica* subsp. *cyanea.* Epicuticular wax is not found in the other species.

Some *Myosotis* species are very similar and diffucult to separate from each other. New useful characters are necessary for a new classification. Nutlet shape and surface morphologies provide comprehensive taxonomic data. In this study, nutlet of 17 *Myosotis* taxa were examined for morphological and micromorphological. Nutlet shape and size, attachment scar shape, nutlet surface type and epicuticular wax were observed important characters.

In *Myosotis* genus, especially nutlet shape and attachment structures have major taxonomic importance (Grau 1978). Attachment scar shapes show variations in studied taxa; reniform, narrow reniform, ellipsoid reniform, reniform -triangular and narrow tongue. *M. alpestris* subsp. *alpestris*, *M. lazica*, *M. lithospermifolia*, *M. olympica*, *M. stricta* and *M. sylvatica* subsp. *rivularis* have lateral groove. Position of attachment scar are valuable for the Boraginaceae family (Yu et al. 2012). Studied nutlet shapes show variations. Wide ovate type was seen mostly. Only *M. sicula* has rounded nutlet shape.

The nutlet colour of studied *Myosotis* species are determined from black to light brown. Most of species have dark and light brown nutlets. Therefore, the colour of nutlet was not useful character to distinguish *Myosotis* species. Binzet and Akçin (2009) reported that nutlet colour of *Onosma* L. species is not used for systematics. Greuter (1965) used the mericarp colour to distinguish *Anchusa* L. species. However, Aytaş Akçin and Ulu (2008) studied *Anchusa* species and they reported that the colour of mericarp was not used as diagnostic character to distinguish investigated *Anchusa* species.

Scanning electron microscopy (SEM) studies show that fruit surface, seed surface and leaf surface pattern characteristics are important taxonomic characteristics for different families and taxa (Shahi Shavvon et al. 2012; Bona 2013; Akçin et al. 2013b). The fruit surfaces of some Boraginaceae genera have been examined using SEM, and this character provides useful information for the classification of Boraginaceae. Nutlet surface micromorphology has been used to identify *Onosma* species (Akçin 2007; Binzet and Akçin 2009). Mericarp properties are useful for the identification of *Anchusa* taxa (Aytaş Akçin and Ulu 2008). Fruit surface and seed coat micromorphologies are benefit characters for species identification of *Cynoglossum* L. (Akçin 2008). Pakravan et al. (2009) has pointed out the diagnostic value of micromorphological features in *Nonea* Medicus. Nutlet surface ornamentation of *Microula* Benth. species can be used to assess the relationships among taxa (Yu et al. 2012). In present study, four

surface types were identified. The most common type is reticulate-areolate. *M. propinqua* has reticulate type and *M. incrassata* has elongated type. Six taxa have rugose type. Nutlet surface patterns of several plant fruits have been examined by scanning electron microscopy and their systematic importance has been proved by many authors (Bobrov et al. 2005; Akçin 2007; Binzet and Akçin 2009; Akçin and Binzet 2010; Yu et al. 2012).

The epicuticular waxes were observed only *M. heteropoda*, *M. laxa* subsp. *caespitosa* and *M. sylvatica* subsp. *cyanea*. The other species have not epicuticular waxes. Anticlinal and periclinal walls of the epidermis cells varies among the studied *Myosotis* species. Anticlinal and periclinal walls of epidermal cells are straight, sinuous, curved and repand type. The most common types of anticlinal walls are curved and sinous. Generally repand and straight periclinal walls are seen in studied nutlets. Only *M. discolor* and *M. incrassata* have straight anticlinal walls. Akçin (2007) reported that some *Onosma* species had straight-sided, wavy, concave, elevated and undulate cell walls.

Consequently, fruit characters, especially surface types, nutlet type, epidermal features and position of attachment scar have diagnostic value for *Myosotis* species.

Acknowledgement: We would like to thank the Gazi University Herbarium (GAZİ) and Hacettepe University Herbarium (HUB).

References

1. Akbulut MK, Şeker ŞS, Şenel G, Akçin ÖE (2016a) A comparative study based on labellum color analysis of certain Ophrys (Orchidaceae) species in Turkey. Rend. Fis. Acc. Lincei. Online Article.
2. Akbulut MK, Akçin ÖE, Şenel G (2016b) Anatomical and micromorphological properties of holoparasite Orobanche gracilis and Orobanche fuliginosa (Orobanchaceae) species. Rend. Fis. Acc. Lincei. Online Article.
3. Akçin ÖE (2007) Nutlets micromorphology of some *Onosma* L. (Boraginaceae) species from Turkey. Biologia 62: 684-689
4. Akçin ÖE (2008) Seed coat and fruit surface micromorphology of some *Cynoglossum* L. (Boraginaceae) species. Bangladesh J Botany 37: 115-119
5. Akçin ÖE, Binzet R (2010) The micromorphological and Anatomical Properties *Onosma angustissimum* Hausskn. & Bornm. and *O. cassium* Boiss. (Boraginaceae). Bangladesh J. Plant Taxon 17: 1-8
6. Akçin ÖE, Aktaş T, Altıntaş MY (2013a) *Myosotis alpestris* F.W.Schmidt (Boraginaceae) türünün anatomik özellikleri. Ordu Univ J Sci Tech 3: 61-68
7. Akçin ÖE, Şenel G, Akçin Y (2013b) Leaf epidermis morphology of some *Onosma* (Boraginaceae) species from Turkey. Turk J Bot 37: 55–64
8. Aytaş Akçin T, Ulu Ş (2008) Micromorphological characters of fruit of some *Anchusa* L. (Boraginaceae) species from Turkey. IJNES 2: 63-67
9. Baytop T (1994) Türkçe Bitki Adları Sözlüğü. Atatürk Kültür, Dil ve Tarih Yüksek Kurumu Türk Dil Kurumu Yayınları, Ankara.
10. Bigazzi M, Nardi E, Selvi F (1997) *Anchusella*, a new genus of Boraginaceae from the Central – Eastern Mediterranean. Plant Syst Evol 205: 241-264
11. Binzet R, Akçin ÖE (2009) Nutlet size, shape and surface ornamentation in 14 *Onosma* species (Boraginaceae). Acta Bot Croat 68: 117-126
12. Bobrov AVFCH, Endress PK, Melikian AP, Romanov MS, Sorokin AN, Bejerano AP (2005) Fruit structure of *Amborella trichopoda* (Amborellaceae). Bot J Linn Soc 148: 265-274
13. Bona M (2013) Seed-coat microsculpturing of Turkish *Lepidium* (Brassicaceae) and its systematic application. Turk J Bot 37: 662-668
14. Dasti AA, Bokharı TZ, Malik AS, Akhtar R (2003) Epidermal morphology in some members of family Boraginaceae in Baluchistan. Asian J Plant Sci 2: 42–47

15. Çıngay B (2012) A Checklist of the Flora of Turkey (Vascular Plant). Nezahat Gökyiğit Botanical Garden and Flora Research Society, Istanbul
16. Dickinson KJM, Kelly D, Mark AF, Wells G, Clayton R (2007) What limits a rare alpine plant species? Comparative demography of three endemic species of *Myosotis* (Boraginaceae). Austral Ecol 32: 155-168
17. Grau J (1978) Flora of Turkey and East Aegan Islands. Edinburgh University Press, Edinburgh
18. Greuter W (1965) Beitröge zur Flora der Südögöis. Candollea 20: 167-218
19. Heywood VH (1978) Flowering plants of the World. Hardcover, Oxford
20. Juan R, Pastor J, Fernandez I (2000) SEM and light microscope observations on fruit and seeds in Scrophulariaceae from southwest Spain and their systematic significance. Ann Bot 86: 323–338
21. Metcalfe CR, Chalk L (1979) Anatomy of Dicotyledons I. Oxford University Press, London.
22. Pakravan M, Nejhad Falatoury A, Tavassoli A (2009) Morphological and Micromorphological Studies of Nonea (Boraginaceae: tribe Boragineae) in Iran. Iran J Bot 15: 129-139
23. Pihu S, Öpik M, Kook E, Reier Ü (2009) Morphological and genetic relation ships of *Myosotis laxa* ssp. *baltica* and s*sp. caespitosa* and typification of *M. laxa* ssp. *baltica.* Acta Soc Bot Pol 78: 37-49
24. Rendle AB (2005) Flowering Plants and Their Classification. Chawla Ofset Printes, New Delhi
25. Shahi Shavvon R, Saeidi Mehrvarz S, Golmohammadi N (2012) Evidence from micromorphology and gross morphology of the genus *Loranthus* (Loranthaceae) in Iran. Turk J Bot 36: 655–666
26. Shinkarenko YV, Vasil'ev VG (2008) Phenolcarboxylic acids from *Myosotis krylovii* and *M. palustris.* Chem Nat Compd 44: 632-633
27. Stearn WT (1985) Botanical Latin. Redwood Burn Limited, London
28. Yu WT, Jacques FMB, Chen ST, Zhou ZK (2012) Nutlet micro-morphology of the genus *Microula* (Boraginaceae) from the Qinghai-Tibetan Plateau, and its systematic implications. Nord J Bot 30: 596-612

Chapter 13

A Deadly Virus In Computer: In Silico World Of Sars-Cov-2, Homology Modeling And Molecular Docking

Nazlı Irmak GİRİTLİOĞLU[1]
Gizem KÖPRÜLÜLÜ KÜÇÜK[2]

1 Yıldız Technical University, Graduate School of Science and Engineering, Department of Molecular Biology and Genetics, İstanbul, Turkey.
ngiritlioglu@outlook.com, ORCID ID: 0000-0001-5034-0984

2 İstanbul Şişli Vocational School, Radiotherapy Program, İstanbul, Turkey.
gizem.koprululu@sisli.edu.tr, ORCID ID: 0000-0001-6667-4532

INTRODUCTION

COVID-19 has been a worldwide threat since 2019 and has transformed our lifestyles. As of March 10, 2021; there are 117 million cases and 2.61 million deaths in the world (*COVID-19 Statistics - Google*, n.d.). This situation will continue until a proper treatment whose exact effects are known is found. In this context, the studies of drug discovery and drug repurposing have become very important issues. Mostly SARS-CoV-2 main structural protein, spike protein has been chosen as the target for this purpose. Molecular docking is the best method to determine protein-ligand interactions computationally. Prediction of the free binding energy of protein-ligand complex gives us thoughts about further *in vitro*/*in vivo* studies but it does not provide the exact result (Wang & Zhu, 2016) because the biological systems show the dynamic properties, so they work differently. On the other hand, we can't display easily the effects of millions of compounds *in vitro*/*in vivo* due to two basic reasons: 1) the costs of kind of these studies, 2) too much time-consuming. Drug discovery is a very complex process that takes 10-15 years and the cost is up to over $1 billion (Issa et al., 2019). Molecular docking programs/software are time and money savers for scientists who study protein-ligand interactions. Also running the mechanistic studies (protein-protein, protein-DNA interactions, etc.) are possible in this way.

Before a docking study, we need the proper structures of the molecules. Generally, these structures have .pdb extensions and RCSB Protein Data Bank (PDB) (Berman et al., 2000; Burley et al., 2021) is utilized for this purpose. If we can not find a proper PDB file of the molecule, our approach will be homology modeling of the amino acid sequence. A homology modeling method is an approach in which a protein whose structure has been determined experimentally by x-ray crystallography or NMR studies is used as a template and the 3-dimensional structure of the target protein is determined based on similarities (Schneider et al., 2009). Homology modeling takes advantage of the fact that evolutionarily related proteins with similar sequences as measured by sequence identity have similar structures. Sequence id describes the length of the branch between two proteins of a phylogenetic tree. Amino acid sequences determine the 3D structure and function of a protein. Similar amino acid sequences have adapted to form similar structures throughout evolution. Homology modeling techniques can obtain structures closest the reality based on this knowledge (Muhammed & Aki-Yalcin, 2019).

In this chapter, homology modeling and molecular docking perspectives on SARS-CoV-2 were discussed.

1. HOMOLOGY MODELING and VISUALISATION TOOLS

The homology modeling process has five steps. These steps are the protein amino acid sequence is obtained, alignment of the target sequence with the templates, three-dimensional coordinates are arranged, detection of mutant side chains made, and replacement of rotamers is made according to the limited energy optimization respectively (Arnold et al., 2006; Berman et al., 2000; Fiser et al., 2000; Vyas et al., 2012).

1.1. Homology Modelling Studies with SWISS-MODEL

The Swiss Institute of Bioinformatics (SIB) is independent research that collects bioinformatics information. The SWISS-MODEL program presents the 3D protein structures, Global Model Quality Estimation (GMQE) values of models, and Ramachandran graphics for amino acids to the user with a report. The available model is selected on the program and this file is downloaded. (Benkert et al., 2011; Kovac & Dickerson, 2006; Waterhouse et al., 2018). SWISS-MODEL is presented protein models by the PDBs.

The model is selected according to the sequence parity and QMEAN value. If the QMEAN value is closest to +1, the model will be an ideal template. SWISS-MODEL program automatically offers many models for our sequence information. The model of the SARS-CoV-2 spike domain was shown in Figure 1.1. QMEAN value is used to select the most suitable model. After the selection of the most suitable model, it is downloaded to the computer as a .pdb document (Benkert et al., 2011; Waterhouse et al., 2018).

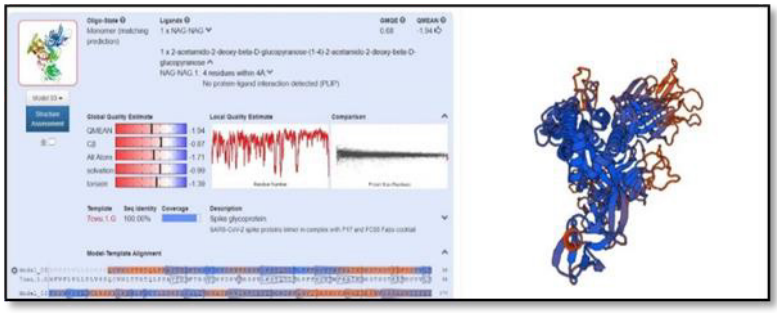

Figure 1.1. Demonstration of SARS-CoV-2 Spike Model in SWISS-MODEL (*Sars N-CoV Spike | Models, n.d.)*.

1.2. Visualization Tools

Molecular visualization programs are most important for demonstrating protein interactions and structures. Open-source programs such as PyMOL (Schrödinger, LLC, 2015), UCSF Chimera (Pettersen et al., 2004), and RASMOL (Sayle & Milner-White, 1995) are the most widely used to demonstrate protein structures and interactions. PyMOL provides high-quality three-dimensional images and a detailed exploration of the protein's structure. Nucleic acids, RASMOL is a molecular graphics program designed for the visualization of proteins, nucleic acids, and small molecules.

UCSF Chimera is another open-source program for visualization. It serves density maps, sequence alignments, and the molecular structure of a protein (J. H. Morris et al., 2007). Three different visualizations can obtain for the model with the UCSF Chimera program. The first is the "ribbons" structure. (Figure 1.2A). This type uses to observe the general differences such as amino acid changes in protein structure. The second selection is the "all atoms" option. (Figure 1.2B).

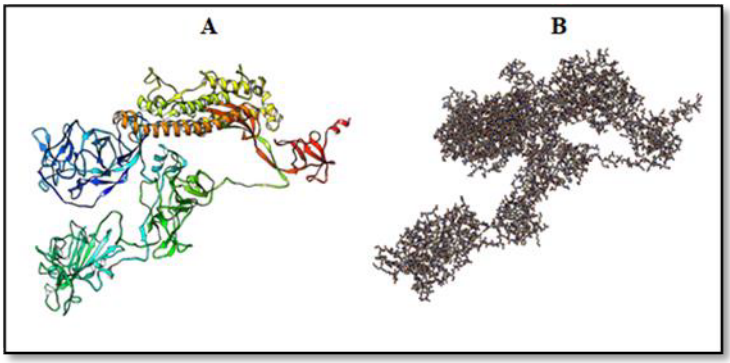

Figure 1.2. The Visualizing of SARS CoV-2 Spike Protein model with UCSF Chimera (Created by Chimera 1.15 ver.)
(Pettersen et al., 2004). A. Ribbons, B. All atoms.

The third option is the "Hydrophobicity surface" (Figure 1.3) and it shows model hydrophobicity. The Hydrophobicity surface selection prefers red-white and blue colors to visualize the protein model. While the hydropathy index changes from a negative value to a positive value, it turns from blue color to white and then to red color (Pettersen et al., 2004).

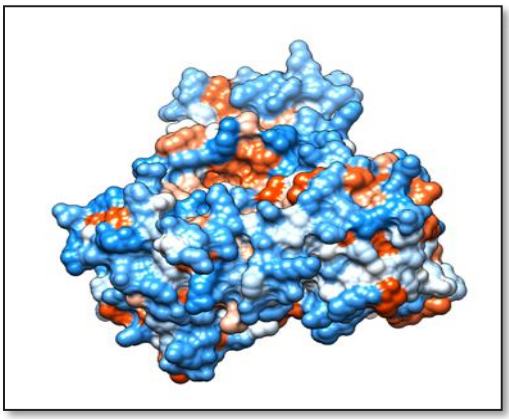

Figure 1.3. Hydrophobicity surface visualizing of a model in UCSF Chimera (Created by UCSF Chimera ver. 1.15) (Pettersen et al., 2004).

2. OUTLINES OF MOLECULAR DOCKING

Molecular docking is a computer-based method that displays the interactions between proteins and protein or non-protein ligands. In a drug development process, docking can be run before *in vitro* and *in vivo* analysis. Safety and efficacy concerns are very important to evaluate a drug before it will be commercial. Also *in vitro* and in *vivo* studies have several limitations: *In vitro* can not mimic the entire system, it is just a bunch of cells. *In vivo* gives efficacy information about our interesting drug on the system base, but animals have short lifetimes. We can not apply a drug for the long-term and can not predict further effects from today to many years later (Gupta et al., 2018). Molecular docking studies have increased dramatically since 1989 and there are 51,404 results in PubMed (https://pubmed.ncbi.nlm.nih.gov/) and 1,067 of them are related to COVID-19 as of March 13, 2021.

Molecular docking is based on the prediction of the orientation of a ligand and the software/programs generally provide a table that contains binding affinity scores. We can choose the best score and the best model of the protein-ligand complex (Figure 2.1) but it should not be forgotten that the best docking score can be failed in the molecular dynamic simulation (Chen, 2015). With current knowledge of substrate-enzyme binding, there are two hypotheses called "lock and key" and "hand-in-glove (or induced fit)". The “pose” term is important to understand receptor-ligand relations. Pose means a conformation of intermolecular interactions of the receptor-ligand couple (*Docking (Molecular)*, n.d.) and it affects the binding energy of this couple. Figure 2.1 shows a basic example. Briefly, different poses cause different binding energies. More negative binding free energies are favorable for a biological system.

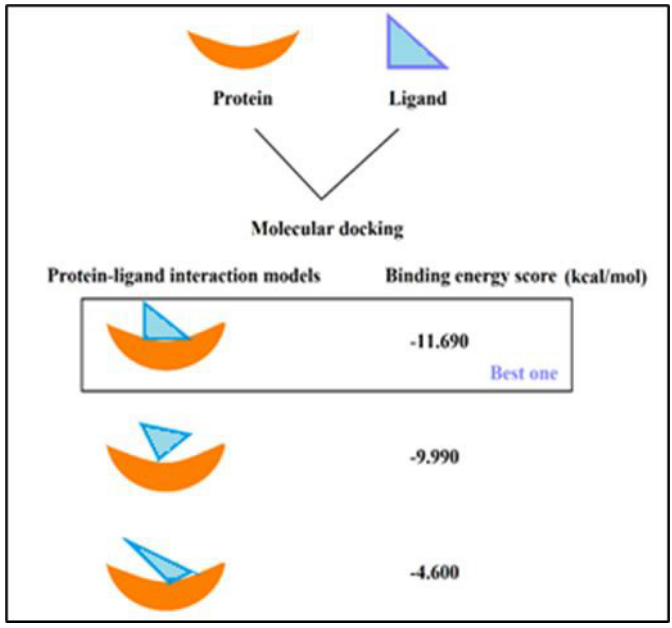

Figure 2.1. An example of protein-ligand poses and binding affinity. Protein-ligand interaction directly affects the binding free energy.

Another important term is the scoring function (SF). SF is a mathematical function that is needed to predict the binding affinity between two molecules after the docking. There are four scoring functions: Empirical, knowledge-based, machine-learning-based, and physics-based SFs. Physics-based SF includes force field (FF), solvation models, and quantum mechanics techniques (Li et al., 2019). FF SF is based on physical atomic interactions (Van der Waals, electrostatic, bond stretching, bending, and torsional forces) (Yuriev et al., 2015).

In a docking study, we should decide which strategy to use. Which data and information do we have? Here, we come across two different approaches: Template-based docking or free docking (also referred to as ab initio docking). There are no PDB files for all proteins in the databases, but we can utilize the sequence similarity of a protein (template) that has a PDB file for determining the structure of a particular protein we are interested in. Template-based docking is based on the homology of the sequences, so homology modeling is a very useful method for these kinds of servers/software/programs. On the contrary, template-free docking can be easily run if the users have their proper structures. Some tools do not need any preparation for protein or other structures. There is a common protocol in Figure 2.2 contained before and after docking steps.

2.2. Molecular Docking Software/Programs

Protein-protein and protein-ligand (implies smaller than a protein in this chapter) docking studies sometimes can be required different software and programs. Autodock is one of the oldest and most known docking programs that was presented 31 years ago by The Scripps Research Institute, and it can be used freely at no cost. The program builds on empirical free energy force fields and its scoring function is physics-based (Goodsell et al., 2021).

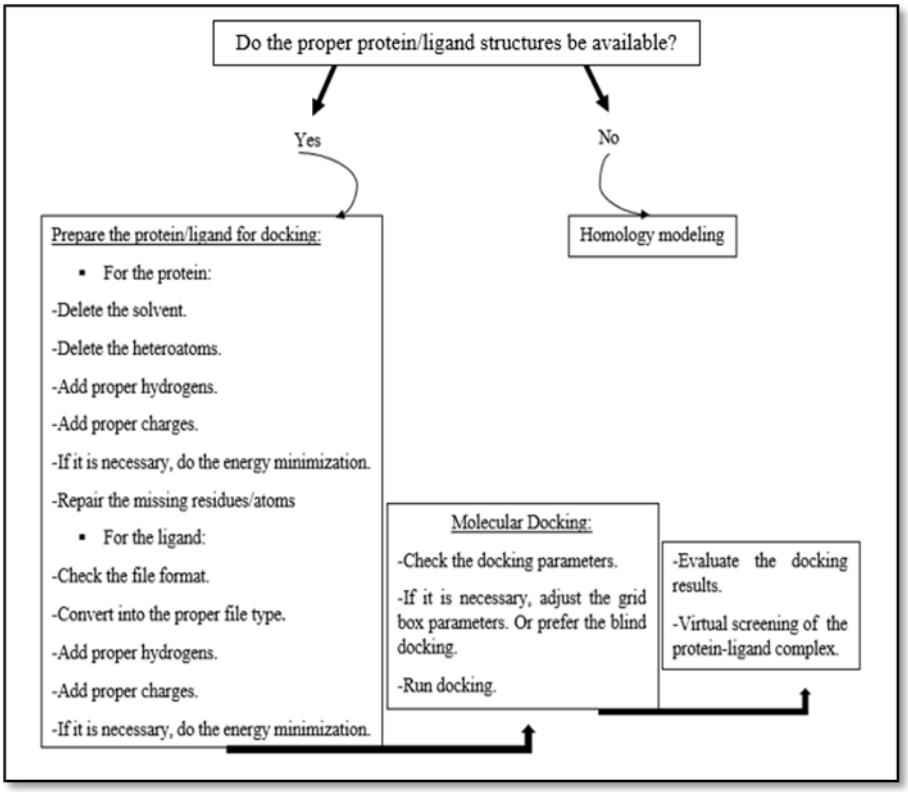

Figure 2.2. Pre-docking and after steps for studying protein-ligand interactions.

Valuation and visualization of interactions are easy to use and it has a user-friendly interface. There is no need to insert any command. A docking example from AutodockTools 1.5.6 (G. M. Morris et al., 2009; Sanner, 1999) was shown in Figure 2.4. Also, Autodock Vina (Trott & Olson, 2009) can be used as a plugin with UCSF Chimera (Pettersen et al., 2004).

Nowadays, personal computers can not be enough for big purposes such as investigating the interactions between SARS-CoV-2 and cellular components. Figure 2.3 showed the interface of AutodockTools 1.5.6 (Morris et al., 2009;

Sanner, 1999). The ClusPro (https://cluspro.bu.edu/), a supercomputer-based molecular docking server is often used for docking PDB files of protein structures (commonly X-ray and NMR structures) or homology models. The tool uses PIPER based on the Fast Fourier Transform (FFT) in the rigid body docking. The docking of PDB files entered into the server results in less than 4 hours (Kozakov et al., 2006, 2017).

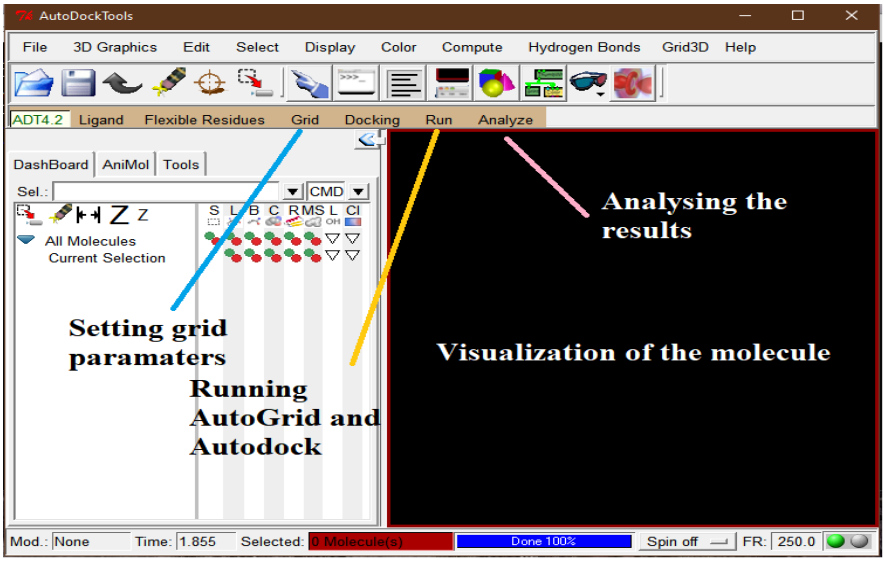

Figure 2.3. The interface of the AutodockTools 1.5.6 (Morris et al., 2009; Sanner, 1999).

ZDOCK (http://zdock.umassmed.edu) is also an FFT-based docking server with high predictive accuracy. Docking jobs run on a computer at the University of Massachusetts Medical School. Runs can be done quickly and the average time is 11.5 minutes (Pierce et al., 2014). HDOCK (http://hdock.phys.hust.edu.cn/) is similar to other docking servers, besides protein-DNA/RNA interactions are workable too. Also, HDOCK allows a hybrid strategy that contains both template-based and free docking. Runs are fast (they take about 10-20 minutes) and the algorithm is based on an iterative knowledge-based scoring function (Yan et al., 2017).

After the docking process, protein-protein/ligand complexes should be visualized via the desired program, and UCSF Chimera could be a good choice for that. But some programs like UCSF Chimera can not visualize complexes in a single file, so protein and other protein/ligands can be saved as separate files and opened separately. This approach sometimes could be hard to apply. Another

approach is to use PyMOL (Schrödinger, LLC, 2015) which is free for only educational purposes. PyMOL can visualize the docking models in high quality and does not require separating the protein and protein/ligand.

2.3. An Overview of Molecular Docking Studies

There are two main docking approaches in COVID-19 studies: 1) blockade of Angiotensin-converting enzyme 2 (ACE2), Transmembrane Serine Protease 2 (TMPRSS2), or Paired Basic Amino Acid Cleaving Enzyme (FURIN) and 2) inhibition of SARS-CoV-2 structural or non-structural components such as spike glycoprotein, the nucleocapsid phosphoprotein, 3-chymotrypsin-like protease ($3CL^{pro}$ or M^{pro}, main protease), RNA dependent RNA polymerase (RdRp), papain-like protease (PL^{pro}).

Ton et.al developed a deep learning platform (Deep Docking) that is useful for the rapid prediction of docking scores of any docking program. They applied 1.3 billion compounds from the ZINC15 library to the program and determined a thousand potential inhibitors for SARS-CoV-2 M^{pro} (Ton et al., 2020). Hall Jr. and Ji investigated some anti-viral drugs and they found that Zanamivir, Indinavir, Saquinavir, and Remdesivir have promising hits on the main protease of SARS-CoV-2. They observed the highest negative docking scores for spike glycoprotein and $3CL^{pro}$ belongs to Coenzyme A (−11.555 kcal/mol) and Dpnh (NADH) (−11.016 kcal/mol) respectively (Hall & Ji, 2020). Garg and his coworkers investigated the effects of some phytochemicals on the inhibition of the M^{pro}.

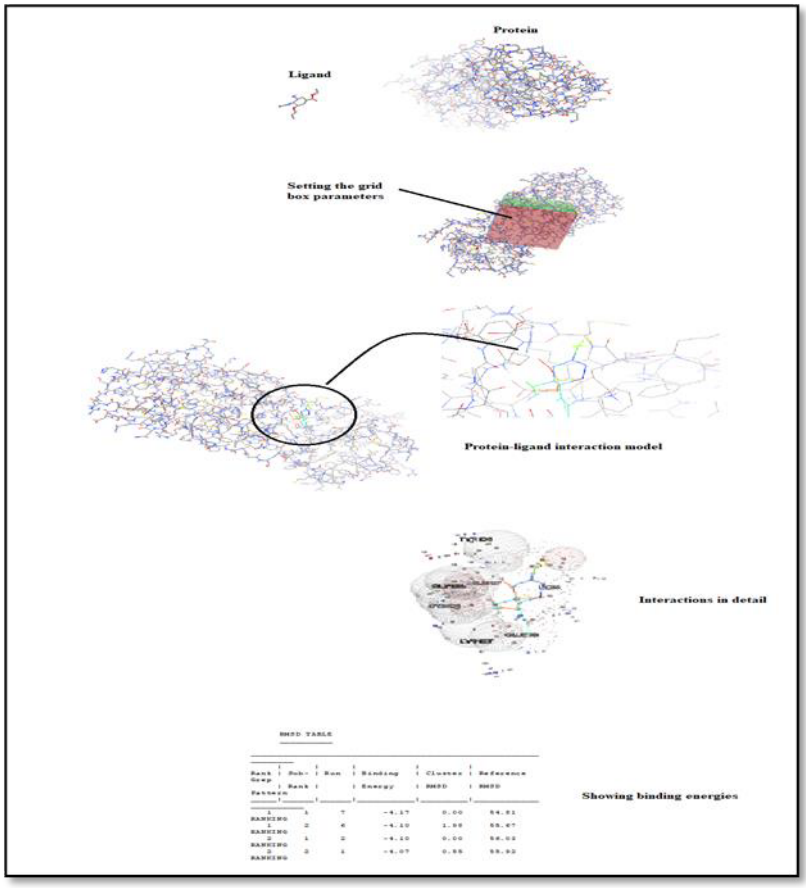

Figure 2.4. A molecular docking example in AutodockTools 1.5.6 (Morris et al., 2009; Sanner, 1999).

The results of the study showed that ginsenosides (docking score: − 9.63 kcal/mol), gedunin (docking score: − 9.51 kcal/mol), nimbin (docking score: − 8.66 kcal/mol), epoxyazadiradione (docking score: − 8.47 kcal/mol) have potential by their binding energies. According to bioavailability radar studies and molecular dynamic simulations, the study indicated that gedunin is a promising phytochemical for COVID-19 (Garg et al., 2020).

The docking approach for COVID-19 does not just cover determining the inhibitor agents for SARS-CoV-2 components also contains the studies of receptor-component interactions. It could be said that our knowledge of COVID-19 has begun at the ACE2 receptor-Spike protein interaction studies that are expanding day by day to investigate single nucleotide polymorphisms of human receptors and SARS-CoV-2 mutations. Calcagnile et al. studied ACE2 missense variants-SARS-CoV-2 spike protein interactions. They used HDOCK (Yan et al.,

2017) and FireDock (Andrusier et al., 2007; Mashiach et al., 2008) as molecular docking tools and specify the missense variants that have higher and lower binding affinities to SARS-CoV-2 spike protein (Calcagnile et al., 2021). Also, other human protein interactions can be studied for unraveling the COVID-19 mechanism. Hussain et al. investigated conformational properties of the human TMPRSS2 and SARS-CoV-2 complex and detected the points of the interactions (Hussain et al., 2020).

CONCLUSION

The models obtained by homology modeling studies can be used in structure-based drug design, protein function, interaction, antigenic properties, and protein engineering studies. Relationships between changes in protein structure due to mutations and drug resistance can also be revealed by these studies. Since the 1980s, molecular docking tools have been improved and *in silico* interaction, model generations have become very important issues for brightening the mechanisms of the diseases. Drug repurposing and development is a very long process, but in a pandemic situation; scientist has to be quick in their research. Computer-based studies may shorten the time. Also; until now, we have known that only ACE2, TMPRSS2, and FURIN are directly related to SARS-CoV-2. But *in silico* studies can open new windows for revealing other interactions.

REFERENCES

1. *About MODELLER*. (n.d.). Retrieved April 2, 2021, from https://www.salilab.org/modeller/
2. Andrusier, N., Nussinov, R., & Wolfson, H. J. (2007). FireDock: Fast interaction refinement in molecular docking. *Proteins: Structure, Function and Genetics*, *69*(1), 139–159. https://doi.org/10.1002/prot.21495
3. Arnold, K., Bordoli, L., Kopp, J., & Schwede, T. (2006). The SWISS-MODEL workspace: A web-based environment for protein structure homology modelling. *Bioinformatics*, *22*(2), 195–201. https://doi.org/10.1093/bioinformatics/bti770
4. Benkert, P., Biasini, M., & Schwede, T. (2011). Toward the estimation of the absolute quality of individual protein structure models. *Bioinformatics*, *27*(3), 343–350. https://doi.org/10.1093/bioinformatics/btq662
5. Berman, H. M., Westbrook, J., Feng, Z., Gilliland, G., Bhat, T. N., Weissig, H., Shindyalov, I. N., & Bourne, P. E. (2000). The Protein Data Bank. In *Nucleic Acids Research* (Vol. 28, Issue 1, pp. 235–242). Oxford University Press. https://doi.org/10.1093/nar/28.1.235
6. Burley, S. K., Bhikadiya, C., Bi, C., Bittrich, S., Chen, L., Crichlow, G. V., Christie, C. H., Dalenberg, K., Di Costanzo, L., Duarte, J. M., Dutta, S., Feng, Z., Ganesan, S., Goodsell, D. S., Ghosh, S., Green, R. K., Guranovic, V., Guzenko, D., Hudson, B. P., … Zhuravleva, M. (2021). RCSB Protein Data Bank: Powerful new tools for exploring 3D structures of biological macromolecules for basic and applied research and education in fundamental biology, biomedicine, biotechnology, bioengineering and energy sciences. *Nucleic Acids Research*, *49*(1), D437–D451. https://doi.org/10.1093/nar/gkaa1038
7. Calcagnile, M., Forgez, P., Iannelli, A., Bucci, C., Alifano, M., & Alifano, P. (2021). Molecular docking simulation reveals ACE2 polymorphisms that may increase the affinity of ACE2 with the SARS-CoV-2 Spike protein. *Biochimie*, *180*, 143–148. https://doi.org/10.1016/j.biochi.2020.11.004
8. Chen, Y. C. (2015). Beware of docking! In *Trends in Pharmacological Sciences* (Vol. 36, Issue 2, pp. 78–95). Elsevier Ltd. https://doi.org/10.1016/j.tips.2014.12.001
9. Coutsias, E. A., Seok, C., & Dill, K. A. (2004). Using quaternions to calculate RMSD. *Journal of Computational Chemistry*, *25*(15), 1849–1857. https://doi.org/10.1002/jcc.20110
10. *COVID-19 statistics - Google*. (n.d.).
11. *Docking (molecular)*. (n.d.). Retrieved March 29, 2021, from http://snst-hu.lzu.edu.cn/zhangyi/ndata/Docking_%28molecular%29.html

12. *Documentation | SWISS-MODEL*. (n.d.). Retrieved April 2, 2021, from https://swissmodel.expasy.org/docs/help
13. Eswar, N., Webb, B., Marti-Renom, M. A., Madhusudhan, M. S., Eramian, D., Shen, M., Pieper, U., & Sali, A. (2006). Comparative Protein Structure Modeling Using Modeller. *Current Protocols in Bioinformatics*, *15*(1). https://doi.org/10.1002/0471250953.bi0506s15
14. Fiser, A., Do, R. K. G., & Šali, A. (2000). Modeling of loops in protein structures. *Protein Science*, *9*(9), 1753–1773. https://doi.org/10.1110/ps.9.9.1753
15. Garg, S., Anand, A., Lamba, Y., & Roy, A. (2020). Molecular docking analysis of selected phytochemicals against SARS-CoV-2 Mpro receptor. *Vegetos*, *33*(4), 766–781. https://doi.org/10.1007/s42535-020-00162-1
16. Goodsell, D. S., Sanner, M. F., Olson, A. J., & Forli, S. (2021). The <scp>AutoDock</scp> suite at 30. *Protein Science*, *30*(1), 31–43. https://doi.org/10.1002/pro.3934
17. Gupta, M., Sharma, R., & Kumar, A. (2018). Docking techniques in pharmacology: How much promising? In *Computational Biology and Chemistry* (Vol. 76, pp. 210–217). Elsevier Ltd. https://doi.org/10.1016/j.compbiolchem.2018.06.005
18. Hall, D. C., & Ji, H. F. (2020). A search for medications to treat COVID-19 via in silico molecular docking models of the SARS-CoV-2 spike glycoprotein and 3CL protease. *Travel Medicine and Infectious Disease*, *35*, 101646. https://doi.org/10.1016/j.tmaid.2020.101646
19. Hussain, M., Jabeen, N., Amanullah, A., Baig, A. A., Aziz, B., Shabbir, S., Raza, F., & Uddin, N. (2020). Molecular docking between human tmprss2 and sars-cov-2 spike protein: Conformation and intermolecular interactions. *AIMS Microbiology*, *6*(3), 350–360. https://doi.org/10.3934/microbiol.2020021
20. Issa, N. T., Badiavas, E. V., & Schürer, S. (2019). Research Techniques Made Simple: Molecular Docking in Dermatology - A Foray into In Silico Drug Discovery. In *Journal of Investigative Dermatology* (Vol. 139, Issue 12, pp. 2400-2408.e1). Elsevier B.V. https://doi.org/10.1016/j.jid.2019.06.129
21. Kufareva, I., & Abagyan, R. (2012). Methods of protein structure comparison. Methods in Molecular Biology, 857, 231–257. https://doi.org/10.1007/978-1-61779-588-6_10
22. Kovac, J., & Dickerson, R. E. (2006). Present at the Flood: How Structural Molecular Biology Came About (Richard E. Dickerson). In *Chemical Education Today www.JCE.DivCHED.org* • (Vol. 83, Issue 9). www.JCE.DivCHED.org
23. Kozakov, D., Brenke, R., Comeau, S. R., & Vajda, S. (2006). PIPER: An FFT-

based protein docking program with pairwise potentials. *Proteins: Structure, Function, and Bioinformatics*, *65*(2), 392–406. https://doi.org/10.1002/prot.21117

24. Kozakov, D., Hall, D. R., Xia, B., Porter, K. A., Padhorny, D., Yueh, C., Beglov, D., & Vajda, S. (2017). The ClusPro web server for protein-protein docking. *Nature Protocols*, *12*(2), 255–278. https://doi.org/10.1038/nprot.2016.169
25. Li, J., Fu, A., & Zhang, L. (2019). An Overview of Scoring Functions Used for Protein–Ligand Interactions in Molecular Docking. In *Interdisciplinary Sciences: Computational Life Sciences* (Vol. 11, Issue 2, pp. 320–328). Springer Berlin Heidelberg. https://doi.org/10.1007/s12539-019-00327-w
26. Mashiach, E., Schneidman-Duhovny, D., Andrusier, N., Nussinov, R., & Wolfson, H. J. (2008). FireDock: a web server for fast interaction refinement in molecular docking. *Nucleic Acids Research*, *36*(Web Server issue). https://doi.org/10.1093/nar/gkn186
27. Morris, G. M., Ruth, H., Lindstrom, W., Sanner, M. F., Belew, R. K., Goodsell, D. S., & Olson, A. J. (2009). Software news and updates AutoDock4 and AutoDockTools4: Automated docking with selective receptor flexibility. *Journal of Computational Chemistry*, *30*(16), 2785–2791. https://doi.org/10.1002/jcc.21256
28. Morris, J. H., Huang, C. C., Babbitt, P. C., & Ferrin, T. E. (2007). structureViz: linking Cytoscape and UCSF Chimera. *Bioinformatics*, *23*(17), 2345–2347. https://doi.org/10.1093/bioinformatics/btm329
29. Muhammed, M. T., & Aki-Yalcin, E. (2019). Homology modeling in drug discovery: Overview, current applications, and future perspectives. *Chemical Biology & Drug Design*, *93*(1), 12–20. https://doi.org/10.1111/cbdd.13388
30. Pettersen, E. F., Goddard, T. D., Huang, C. C., Couch, G. S., Greenblatt, D. M., Meng, E. C., & Ferrin, T. E. (2004). UCSF Chimera - A visualization system for exploratory research and analysis. *Journal of Computational Chemistry*, *25*(13), 1605–1612. https://doi.org/10.1002/jcc.20084
31. Pierce, B. G., Wiehe, K., Hwang, H., Kim, B. H., Vreven, T., & Weng, Z. (2014). ZDOCK server: Interactive docking prediction of protein-protein complexes and symmetric multimers. *Bioinformatics*, *30*(12), 1771–1773. https://doi.org/10.1093/bioinformatics/btu097
32. *PubMed*. (n.d.).
33. Sanner, M. (1999). Python: a programming language for software integration and development. *Undefined*.
34. *Sars n-CoV spike | Models*. (n.d.). Retrieved April 2, 2021, from https://swissmodel.expasy.org/interactive/16B5UU/models/
35. Sayle, R. A., & Milner-White, E. J. (1995). RASMOL: biomolecular graphics

for all. *Trends in Biochemical Sciences*, *20*(9), 374–376. https://doi.org/10.1016/S0968-0004(00)89080-5

36. Schneider, M., Fu, X., & Keating, A. E. (2009). X-ray vs. NMR structures as templates for computational protein design. *Proteins: Structure, Function and Bioinformatics*, *77*(1), 97–110. https://doi.org/10.1002/prot.22421
37. Schrödinger, LLC. (2015). *The {PyMOL} Molecular Graphics System, Version~1.8*.
38. Ton, A. T., Gentile, F., Hsing, M., Ban, F., & Cherkasov, A. (2020). Rapid Identification of Potential Inhibitors of SARS-CoV-2 Main Protease by Deep Docking of 1.3 Billion Compounds. *Molecular Informatics*, *39*(8). https://doi.org/10.1002/minf.202000028
39. Trott, O., & Olson, A. J. (2009). AutoDock Vina: Improving the speed and accuracy of docking with a new scoring function, efficient optimization, and multithreading. *Journal of Computational Chemistry*, *31*(2), NA-NA. https://doi.org/10.1002/jcc.21334
40. *UCSF Chimera Home Page*. (n.d.). Retrieved April 2, 2021, from https://www.cgl.ucsf.edu/chimera/index.html
41. Vyas, V. K., Ukawala, R. D., Ghate, M., & Chintha, C. (2012). Homology modeling a fast tool for drug discovery: Current perspectives. In *Indian Journal of Pharmaceutical Sciences* (Vol. 74, Issue 1, pp. 1–17). Indian J Pharm Sci. https://doi.org/10.4103/0250-474X.102537
42. Wang, G., & Zhu, W. (2016). Molecular docking for drug discovery and development: A widely used approach but far from perfect. In *Future Medicinal Chemistry* (Vol. 8, Issue 14). Future Science. https://doi.org/10.4155/fmc-2016-0143
43. Waterhouse, A., Bertoni, M., Bienert, S., Studer, G., Tauriello, G., Gumienny, R., Heer, F. T., De Beer, T. A. P., Rempfer, C., Bordoli, L., Lepore, R., & Schwede, T. (2018). SWISS-MODEL: Homology modelling of protein structures and complexes. *Nucleic Acids Research*, *46*(W1), W296–W303. https://doi.org/10.1093/nar/gky427
44. Yan, Y., Zhang, D., Zhou, P., Li, B., & Huang, S. Y. (2017). HDOCK: A web server for protein-protein and protein-DNA/RNA docking based on a hybrid strategy. *Nucleic Acids Research*, *45*(W1), W365–W373. https://doi.org/10.1093/nar/gkx407
45. Yuriev, E., Holien, J., & Ramsland, P. A. (2015). Improvements, trends, and new ideas in molecular docking: 2012-2013 in review. *Journal of Molecular Recognition*, *28*(10), 581–604. https://doi.org/10.1002/jmr.2471

Chapter 14

A Research on the Histo-Anatomical Characteristics of Some Species of *Anagallis* (Primulacaeae) Distributed in Turkey

Sibel ULCAY[1]

1

Introduction

Primulacaeae consists of 58 genera and 2500 species (APG, 2016). *Anagallis* is a genus belonging to the subfamily Myrsinoideae of Primulaceae (Ka¨llersjo¨ et al., 2000). 24 taxon of the genus are distributing naturally (Pax and Knuth, 1903). With the species identified from the mountains of East Africa, this number has increased to 39 (Fries, 1923). In Turkey, 6 taxa belonging to the genus *Anagallis* are distributed. (Coşkunçelebi, 2012). Family members are medically important. Various studies have shown the medicinal value of the plants, such as an expectorant, anti-bacterial, anti-diuretic, antioxidant, antimicrobial, antiviral, antifungal, mutagenic, antimutagenic, cytotoxic, anticancer. Also species treats liver, lung problems, gallstones, kidney stones, urinary infection, and dermatological diseases (Bajaj et al., 1999). Bronchium, Sinupret, Pectosol, and Tussipect are its herbal compounds derived from roots and flowers of plants of family Primulaceae (Ibrahim et al. 2018).

Anagallis species are also used in traditional therapy. *Anagallis arvensis* L. species is used in the treatment of skin diseases and conjunctivitis in various countries of the world, as an anti-inflammatory, antiasthmatic, and antiflatulent antitussive and expectorant (Viegi et al., 2003; Akerreta, et al., 2007; Gairola et al., 2010; Bhatia et al., 2014) *Anagallis arvensis* is a summer annual herb which blossoms at the end of spring (Osbornová-Kosinová, 1984) It has ability to modify according to climate (Mir and John, 2014) It is found across the Europe and dispersed worldwide because of ruderal habitat. It is abundant in Egypt, Palestine, non-tropical region of South America, and Taiwan (Salam et al. 2011; Sharifi et al. 2016). The literature witnesses 1000 species of the plant grouped in 22 genera which are further divided in 5 different tribes: *Primuleae*, *Cyclamineae*, *Lysimachieae*, *Samoleae*, and *Corideae*. *Anagallis* belongs to the *Lysimachieae* tribe comprising of 28 species. (Sayanova et al., 1999) This genus is characterized by some distinguishing characters, such as flowering pattern is pentamerous, nectarless, polypetalous, and have a compound ovary. Petals of this genus have nyctinastic behavior, (i.e., open up in daylight but close at dusk), which leads to self-pollination.

The number of study on *Anagallis* species is limited. These articles are mostly related to morphological biochemical and seed germination (Manns and Anderberg, 2007; Salam, 2011; Quintana et al., 2008). With this study, it was aimed to determine the anatomical features of 3 taxa belonging to *Anagallis* genus, which have not been studied before. The results we will obtain will benefit future studies with *Anagallis* species.

Materials and Methods

Specimens of the species were collected between April and July (Table 1) from Kırşehir and Niksar- Tokat (Turkey) (Table 1). Some of the specimens were fixed in 70% alcohol, others were turned into herbarium samples. In the identification of the species, the work named Flora of Turkey was used (Davis, 1978). Sections were taken by hand and used glycerin as analysis medium The preparates were made permanent by the glycerin-gelatin method (Vardar, 1998). The cell types obtained from the root, stem and leaf sections of the species were determined by using Upright Microscope Eclipse Ni-U imaging system and photographed. Cell measurements were made from transverse and superficial sections of taxa. 20 measurements were taken from tissues such as epidermis, periderm, parenchyma and vascular bundle elements (Table 2).

Table 1. Information collected from the taxa researched.

Taxa	**Locality of collection**	**Altitude (m)**	**Voucher and date collection**	**Alcohol stock number**	**Herbarium number**
A. arvensis var. *arvensis*	Gürçeşme kasabası (Niksar-Tokat)	356 m	SULCAY60, 2019.07.28	A87	360
A. arvensis var. *careulea*	Gürçeşme kasabası (Niksar-Tokat)	350 m	SULCAY60 2019.06.07	A142	363,
A. foemina	Kırşehir (Güneydoğusu)	1027 m	SULCAY60, 2019.09.03	A52	357

Results and Discussion

Root

It has been determined that they have a secondary structure in the root cross sections of the species. Periderm cells are shattered from time to time and are 2-3 layered. The central cylinder is filled with secondary xylem elements. Xylem is oval, rectangular, and circular shaped. Phloem is 4-5 layered. The cortex is rather constricted. The cortex is consisting of 3-4 rows of parenchyma cells. Cambium is occurred crushed cells and is indistinguishable (Figure 1).

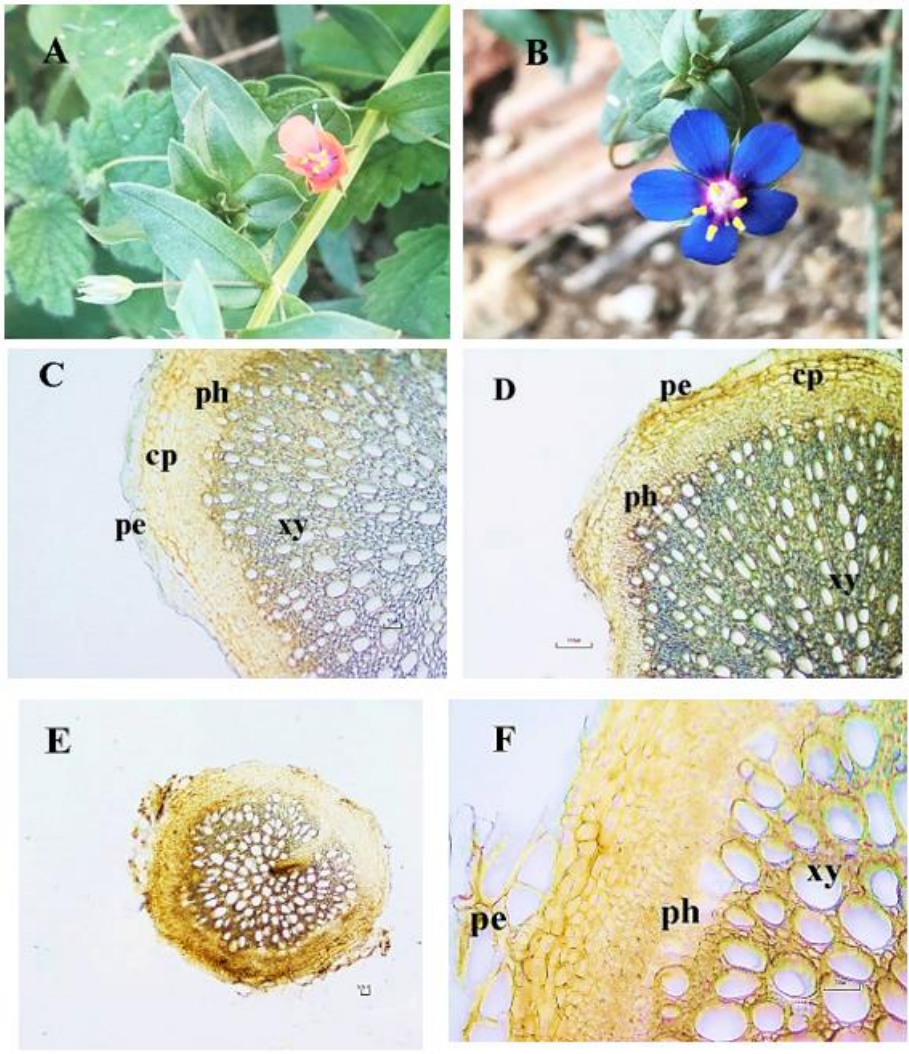

Figure 1 Roots cross-sections of species. A *A. arvenseis* var. *arvensis genel görünüşü, B A. foemina genel görünüşü, C A. arvenseis* var. *arvensis* cross-sections D *A. arvenseis* var. *caerulea E. A. foemina*. pe peridermis, cp cortex parenchyma, ph phloem, xy xylem (Scala 50 mμ).

Stem

Stem cross-sections of the species are angular. Each corner has formed a long protrusion towards the outside. Epidermis cells are circular, rectangular or square shaped. Stomata have been identified on the epidermis. Glandular or non-glandular hair is not found on the stem. The cortex is quite narrow and 4-5 layered. Vascular bundles are 4 and placed in the corners. The pith is quite large

and the parenchymal cells in this region are large in diameter and have intercellular spaces (Figure 2).

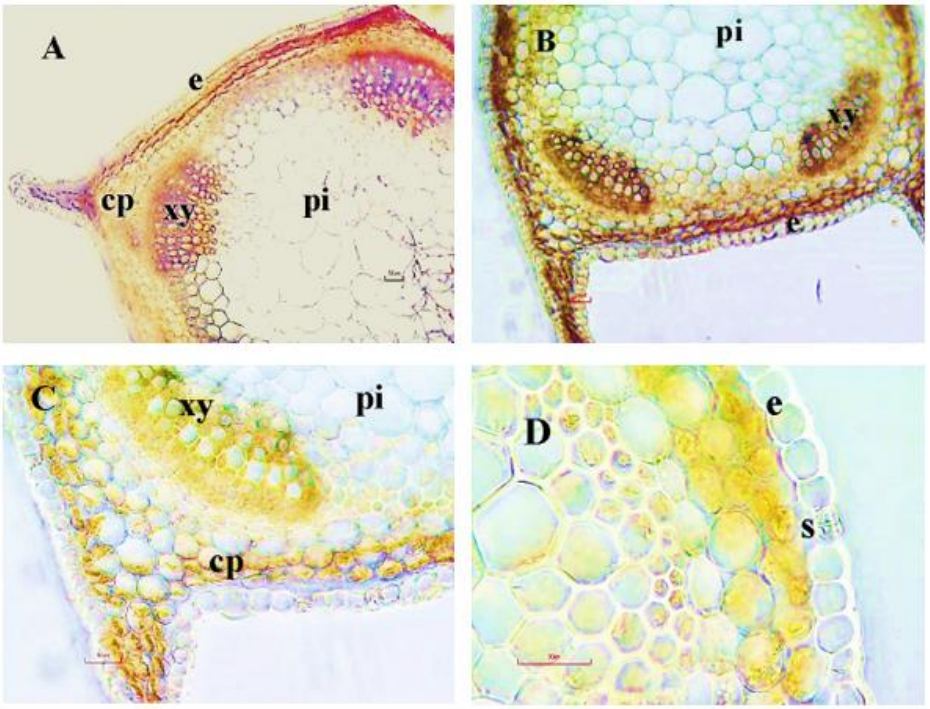

Figure 2 Stems cross-sections of species. A *A. arvenseis* var. *arvensis,* B *A. arvenseis* var. *caerulea*, C *A. arvenseis* var. *caerulea* -D *A. foemina* e epidermis, cp cortex parenchyma, pi pith, s stomata, xy xylem (Scala 50 mμ).

Leaf

According to the leaf cross-sections of the species, the epidermis cells are circular in shaped. A thin cuticle layer is cover the epidermis. The mid-vein areas are prominent and contain a vascular bundle. Anisocytic stomata were formed on the lower and upper surfaces of the isolateral leaves. The sizes of stomas are given in Table 1 (Figure 3).

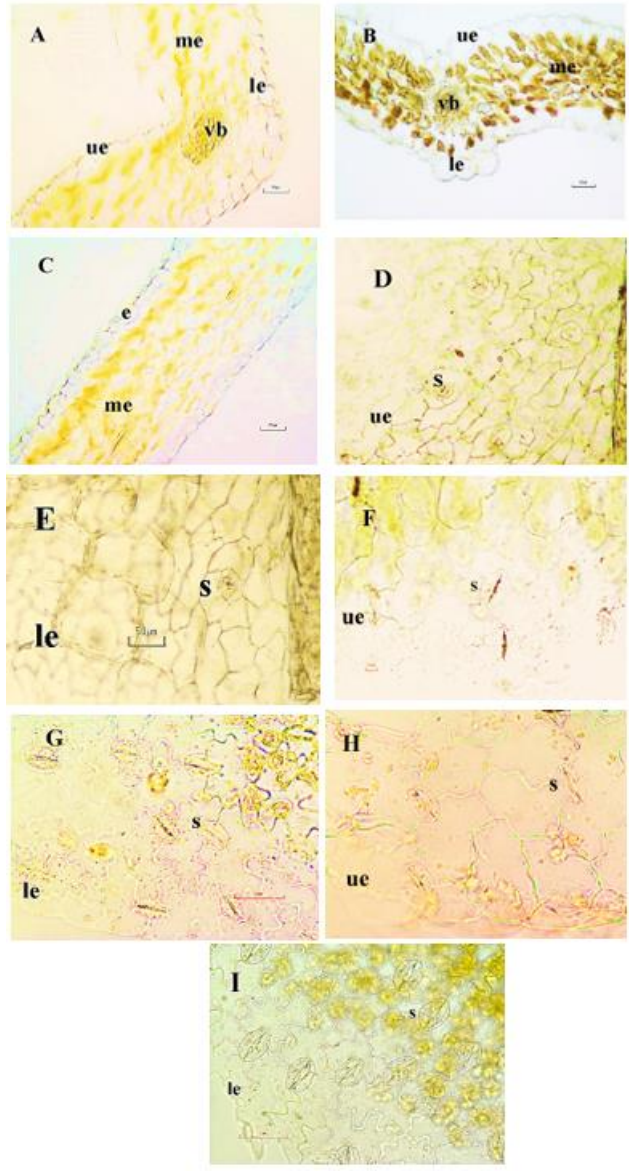

Figure 3. Transverse and superficial sections of leaf. A-D-E *A. arvensis* var. *arvensis*, B-F-G *A. arvensis* var. *caereula* C-I-H *A. foemina*. ue upper epidermis, le: lower epidermis, parenchyma, s: stoma, vb vascular bundle (scale bar 50 µm).

Table 2 Anatomical measurement results of taxa.

Characters	*A. arvensis var.arvensis*		*A. arvensis* var. *caereula*		*A. foemina*	
	Width (µm) ±Se	Length (µm) ± Se	Width (µm) ± Se	Length (µm) ± Se	Width (µm) ± Se	Length (µm) ± Se
Root periderm	20.43±0.84	32.69±2.56	44.13±3.37	41.92±7.13	47.29±2.91	88.51±10.36
Diameter of root cortex cells	16.56±0.87		19.66±1.29	38.25±3.30	18.34±1,91	
Root diameter of trachea	24.98±1.50		26.71±1.57	53.93±2.26	52.45±1.48	
Stem epidermis	18.65±0.54	30.29±1.50		22.47±2.31		25.21±2.14
Stem collenchyma	20.13±2.13		11.75±0.98		21.55±2.13	
Stem cuticle	9.25±0.56		8.12±0.65		6.45±0.40	
Stem diameter of cortex parenchyma	40.88±2.44		19.50±1.69		30.55±2.08	
Stem diameter of pith cells	98.40±6.42		75.39±8.74		69.41±11.09	
Stem diameter of trachea	16.21±0.99		14.81±2.11		17.77±1.06	
Leaf epidermis	51.21±3.30		20.61±1.20		36.25±3.36	
Lower stomata	26.21±0.03	39.36±0.13	27.38±0.43	37.31±1.27	21.04±1.28	30.37±0.55
Upper stomata	24.53±0.13	34.60±0.05	28.25±1.01	38.56±1.19	18.56±2.75	36.79±0.73
Leaf parenchyma	37.40±0.40		41.22±13.05		41.88±0.77	32.32±0.90

Discussion

In this study, three taxa belonging to the genus *Anagallis* were examined anatomically and its findings were presented by us for the first time. The roots of taxa are in the secondary structure. Bejenaru et al. (2013) reported that the root of *Lysimachia punctata* L., which is a member of Primulaceae, has a primary structure. In another study, *Primula acaulis* subsp. *acaulis* (L.) L. it is reported that the root of the species also has a primary structure (Akçin et al., 2019). The central cylinder is quite large in all three taxa. Secondary transmission elements fill the pith area. The stem cross-sections of the species are all four-cornered, with outward extensions at the corners and vascular bundles are at the corners. The stem structure of all three plants is very similar to each other. No hairs were found on either the root or the stem surface. The leaf type of the plants we examined is isolateral. However, Primulaceae family generally has dorsiventral type mesophyll structure (Metcalfe and Chalk, 1979). *P. macrocalyx* Bunge, *P. pallasi* Lehm. and *P. denticulata* Sm. species, the leaves are dorsiventral type (Belaeva

and Butenkova, 2019). In the leaves of the studied species, anomocytic type stomata are present on both surfaces. Davis (1978) states that stoma sizes should be considered together with morphological findings in distinguishing *Anagallis* species distributed in Turkey. In our study, the stomata sizes of the species were also different. Especially *A. foemina* stoma width and length are smaller than the other species (Table1). Stomata sizes can be used as criteria to distinguish *Anagallis* species. No hairs were found on the leaf surface.

With this study, the anatomical features of 3 taxon belonging to the genus *Anagallis* were determined, and their similarities and differences with other taxa and with each other were revealed.

The roots of taxa are in the secondary structure. Bejenaru et al. (2013) reported that the root of *Lysimachia punctata* L., which is a member of Primulaceae, has a primary structure. In another study, it is reported that the root of *Primula acaulis* subsp. *acaulis* also has a primary structure (Akçin et al. 2019). The central cylinder is quite large in all three taxa we studied. Secondary vascular elements fill the pith region. The stem cross-sections of the species are all four-cornered, with outward extensions at the corners. Conduction bundles were formed at the corners of these extensions. The number of vascular bundles is 4 in all taxon. The stem structure of these three plants is very similar to each other. No hairs were found on both the root and stem surface. The leaf type of the plants we examined is isolateral. Generally, the mesophyll type of the Primulaceae family is dorsiventral (Metcalfe and Chalk, 1979). *P. macrocalyx*, *P. pallasi* and *P. denticulata* species, the leaves are dorsiventral (Belaeva and Butenkova, 2019). The leaves of *P. veris*, are isolateral. (Marchyshyn and Shostak, 2014). In the leaves of the studied species, anomocytic stomata are present on both surfaces. Davis (1978) states that stomata sizes should be considered together with morphological findings in distinguishing *Anagallis* species distributed in Turkey. In particular, stomatal width and length of *A. foemina* are smaller than the other two taxon (Table1). Stomata sizes can be used as criteria to distinguish *Anagallis* species.

As a result, with this study, the anatomical features of 3 taxon belonging to the genus *Anagallis* were determined, and the similarities and differences with other taxa and with each other were tried to be revealed.

References

1. Akçin, O. E., Yapar, D., Özbucak, T., & Akçin, Y. (2019). An anatomical study on *Primula acaulis* subsp. *rubra* (Primulaceae) distributed in the Central Black Sea region. *Academic Journal of Agriculture, 10*(1), 195-200.
2. Akerreta, S., Cavero, R. Y., López, V., & Calvo, M. I. (2007). Analyzing factors that influence the folk use and phytonomy of 18 medicinal plants in Navarra. *Journal of Ethnobiology and Ethnomedicine*, *3*(1), 1-18.
3. APG (2016). An update of the Angiosperm Phylogeny Group classification for the orders and families of flowering plants: APG IV. *Botanical Journal of the Linnean Society 181*(1): 1 -20.
4. Bajaj, Y. P. S. (1999). *Anagallis arvensis* L. (Common Pimpernel): In vitro culture, regeneration of plants, and the formation of anagalline and other saponins. In *Medicinal and Aromatic Plants XI* (pp. 1-10). Springer, Berlin, Heidelberg.
5. Belaeva, T. N., & Butenkova, A. N. (2019). Leaf anatomy of valuable species of genus Primula. *Ukrainian Journal of Ecology*, *9*(3), 150-155.
6. Bejenaru, L. E., Bejenaru, C., Mogosanu, G. D., & Oancea, C. N. (2014). Histo-anatomical investigation on Lysimachia punctata l.(primulaceae) species. *Annals of the University of Craiova-Agriculture, Montanology, Cadastre Series*, *43*(1), 31-39.
7. Bhatia, H., Sharma, Y. P., Manhas, R. K., & Kumar, K. (2014). Ethnomedicinal plants used by the villagers of district Udhampur, J&K, India. *Journal of Ethnopharmacology*, *151*(2), 1005-1018.
8. Davis, P. H. (1978). Flora of Turkey and the East Aegean Islands, Vol. 6, 139-141.
9. Fries, T.C. (1923). The *Anagallis* species of the African high mountains. Note sheet of the royal botanical garden and museum in Berlin, (75), 329-339.
10. Gairola, S., Gupta, V., Bansal, P., Singh, R., & Maithani, M. (2010). Herbal antitussives and expectorants-a review. *International Journal of Pharmaceutical Sciences Review and Research*, *5*(2), 5-9.
11. Ibrahim, A. M., & Ghoname, S. I. (2018). Molluscicidal impacts of *Anagallis arvensis* aqueous extract on biological, hormonal, histological and molecular aspects of Biomphalaria alexandrina snails. *Experimental parasitology*, *192*, 36-41.
12. Källersjö, M., Bergqvist, G., & Anderberg, A. A. (2000). Generic realignment in primuloid families of the Ericales sl: a phylogenetic

analysis based on DNA sequences from three chloroplast genes and morphology. *American Journal of Botany*, *87*(9), 1325-1341.
13. Marchyshyn, S. M., & Shostak, L. H. (2014). Anatomical structure of the leaves and flowers of primrose (Primula veris L.). *Farmatsevtychnyi zhurnal*, (6), 69-76.
14. Metcalfe, C.R. and L. Chalk. (1979). Anatomy of the dicotyledons. Second ed. Oxford: Clarendon Press.
15. Mir, G. M., & John, S. A. (2014). Ethno-medicinal study of Pulwama tehsil (Jammu and Kashmir). *Journal of Medicinal Plant Studies*, *2*(4), 5-8.
16. Osbornová-Kosinová, J. (1984). Notes on the synanthropic plants of Egypt. *Folia Geobotanica et Phytotaxonomica*, *19*(3), 279-285.
17. Pax, F., & R. Knuth. (1903). Primulaceae. Pp. 1–386 in *The Plant Kingdom* 22 (IV, 237). ed. A. Engler. Leipzig: Engelmann
18. Quintana, A., Freyre, R., Davis, T. M., & Griesbach, R. J. (2008). Genetic studies of flower color in *Anagallis monelli* L. *HortScience*, *43*(6), 1680-1685.
19. Salam, I. U., Moinuddin, A., & Syed, T. A. (2011). Allelopathic effect of Scarlet pimpernel (Anagallis arvensis) on seed germination and radical elongation of mung bean and pearl millet. *Pakistan Journal of Botany*, *43*(1), 351-355.
20. Sayanova, O., Napier, J. A., & Shewry, P. R. (1999). Δ6-Unsaturated fatty acids in species and tissues of the Primulaceae. *Phytochemistry*, *52*(3), 419-422.
21. Sharifi-Rad, J., Hoseini-Alfatemi, S. M., Miri, A., Sharifi-Rad, M., Sharifi-Rad, M., Hoseini, M., & Sharifi-Rad, M. (2016). Exploration of phytochemical and antibacterial potentiality of Anagallis arvensis L. extract against methicillin-resistant Staphylococcus aureus (MRSA). *British Biotechnology Journal*, *10*(2), 1-8.
22. Vardar, Y. (1998). Preparation Techniques in Botany. Ege University Faculty of Science Printing Works, İzmir, 112 p.
23. Viegi, L., Pieroni, A., Guarrera, P. M., & Vangelisti, R. (2003). A review of plants used in folk veterinary medicine in Italy as basis for a databank. *Journal of Ethnopharmacology*, *89*(2-3), 221-244.